AFOSR TN-59-218
ASTIA AD 211 780

THE UNIVERSITY OF MICHIGAN

COLLEGE OF ENGINEERING
Department of Electrical Engineering
Solid-State Devices Laboratory

Technical Report No. 7

AN INVESTIGATION OF REACTIONS INVOLVED IN THE PREPARATION OF FERRITES

Clinton F. Jefferson

UMRI Project 2495

under contract with:

SOLID STATE SCIENCES DIRECTORATE
AIR FORCE OFFICE OF SCIENTIFIC RESEARCH
CONTRACT NO. AF 18(603)-8, DIVISION FILE NO. 40-24
WASHINGTON, D. C.

administered by:

THE UNIVERSITY OF MICHIGAN RESEARCH INSTITUTE ANN ARBOR

January 1959

PREFACE

The development of ferrites as useful components in electrical circuits is a result of cooperative research efforts of scientists of varied disciplines. Physicists, chemists, mineralogists, ceramicists, and engineers have all contributed to the theory of the origin of magnetism, materials development, and circuit application of ferrites. As a result, research on ferrites has been a common meeting ground for the exchange of ideas between the various physical sciences.

There is a need for a better understanding of the processes involved in the preparation of ferrites. One of the problems with which the engineer is confronted in the utilization of ferrites is the variability of magnetic properties between materials which are supposedly identical. An attempt to reproduce ferrites with the same magnetic properties in successive preparations, even when, apparently, the most minute detail is followed in the procedure, often results in failure. This can mean only that the magnetic properties of the final product are sensitive to the slightest variation in the manufacturing procedure. This study was conducted to obtain information about some of the reactions involved in the preparation of ferrites which might be responsible for this behavior. In some instances, a correlation between physical and chemical properties and the magnetic properties has been made. The emphasis has, however, been placed on the investigation of physical and chemical changes resulting from the solid-state reactions.

The author wishes to express his appreciation to the many people who aided him during the course of this work. In particular, he wishes to thank

Professor D. M. Grimes and Professor L. Thomassen for their many helpful discussions of all phases of the work. He is indebted to Professor R. M. Denning for helpful suggestions in the work with differential thermal analysis, Professor E. F. Westrum for his discussions of the phase studies, and Professor L. S. Ramsdell for criticisms of the manuscript.

Finally, he is indebted to the Air Force Office of Scientific Research, Air Research and Development Command, Solid State Science Division, for supporting this study.

TABLE OF CONTENTS

LIST OF TABLES

LIST OF FIGURES

LIST OF FIGURES (Continued)

LIST OF FIGURES (Concluded)

ABSTRACT

The purpose of this study was to investigate some solid-state reactions involved in the preparation of ferrites. By means of microscopic examination of polished sections, chemical analysis, X-ray analysis, density measurements, and magnetic measurements such as the Curie temperature and saturation moment per gram, the phase relationships, kinetics of the spinel reaction in several different atmospheres, and the densification process have been studied in the systems $(Ni,Zn)O\text{-}Fe_2O_3$ and $Li_2O\text{-}Fe_2O_3$. Some magnetic properties of ferrites contained in the system $Ni_xZn_{1-x}Fe_2O_4\text{-}Fe_2O_3$ are correlated with the method of preparation.

By differential thermal analysis, chemical analysis, and saturation moment measurements, the progression of the oxidation of the systems $Ni_{.474}Zn_{.526}Fe_2O_4\text{-}Fe_3O_4$ and $LiFe_5O_8\text{-}Fe_3O_4$ has been followed. The temperature at which γFe_2O_3, which forms during the oxidation of the above systems, transforms to αFe_2O_3 has been determined as a function of the composition.

1. INTRODUCTION

A group of oxides with the general formula of XY_2O_4 is known as the spinels. This class of compounds has the same crystal structure as the mineral spinel, $MgAl_2O_4$, from which its name has been taken. Included in this classification are the aluminates $MeAl_2O_4$, the chromites $MeCr_2O_4$, the titanates Me_2TiO_4, the germanates Me_2GeO_4, and the ferrites $MeFe_2O_4$. These compounds are all cubic and belong to the space group $Fd\bar{3}m$.

The unit cell of the spinels consists of $X_8Y_{16}O_{32}$. The oxygen atoms are arranged in a close-packed structure with two types of interstices between neighboring oxygen atoms. The tetrahedral interstices have been called the A sites and the octahedral interstices have been called the B sites. In the unit cell there are 64 A sites, of which 8 are occupied, and 32 B sites, of which 16 are occupied. The distribution of the cations among the available sites has received a considerable amount of study. Barth and Posnjak[1] found that there are two ways in which the cations can be distributed over the A and B sites: The 8 X can be on the A sites and the 16 Y on other B sites, or the 8 Y can be on the A sites with 8 Y and 8 X distributed randomly on B sites. The first arrangement is known as the normal structure and the second as the inverted structure. It is conventional to designate the sites by writing the A sites first, followed by the B sites in brackets as follows:

$$X_8[Y_{16}]O_{32} \qquad Y_8[X_8Y_8]O_{32}$$

The spinels are classified as 2-3 spinels when X is a divalent cation and Y is a trivalent cation and as 2-4 spinels when X is a divalent cation and Y is a tetravalent cation. It has been found that the 2-4 spinels occur only in the inverted structure. Barth and Posnjak,[1] and Verwey and

Heilmann[2] found that all the ferrites studied except Zn and Cd ferrites have the inverse structure; the latter two have the normal structure.

The nomenclature of the ferrites has grown rather confusing. The term ferrite has been widely accepted for the oxides with the formula $MeFe_2O_4$. The term was first used in naming the mineral magnesioferrite, $MgFe_2O_4$, by Rammelsberg[3] in 1859. Before the structure of the spinels was known, the oxides were thought to be salts of the acid $H_2(FeO_2)_2$. The structure, however, has shown that they are really double oxides and might best be expressed by the formula $MeOFe_2O_3$. Unfortunately, the term ferrite is also used for the α iron phase in metallurgy. This name, first suggested by Howe, was adopted from the mineralogical term.[4] It has, however, met with wide acceptance and is in common usage among the metallurgists. The term ferrite is also applied to the oxides $LiFeO_2$, $NaFeO_2$, and $KFeO_2$, while the name ferrate is used for the higher oxides, i.e., Na_2FeO_4 and K_2FeO_4.[5] From the above consideration, it seems that naming $NiOFe_2O_3$ as the double oxide, i.e., nickelous ferric oxide, might be less confusing.

According to Dana's System of Mineralogy,[6] the origin of the name spinel is unknown. It appears to have been given originally to the mineral spinel, $MgOAl_2O_3$. It has since been adopted as a class name for all oxides having the same structure. The term ferrospinel has been in use for the ferromagnetic members of the oxides with the composition $MeFe_2O_4$. It appears that the term ferrispinel would be more appropriate, since the spinels are correctly ferrimagnetic and the term "ferri" also denotes iron in the trivalent state. Thus nickelous ferrispinel would be the spinel containing divalent nickel and trivalent iron. Because of its wide acceptance, the term ferrite is used throughout this paper for the oxides with the formula $MeFe_2O_4$ where Me designates a divalent cation.

Paramagnetism arises from the fact that atoms which have an unpaired

electron have a resultant magnetic moment. Ferrimagnetism arises from the interaction of atoms with unpaired electrons on one site with those on another. Ferrimagnetism, then, is a cooperative phenomenon requiring crystallographic consideration as well as consideration of the atomic structure of the atoms involved, while paramagnetism is an atomic phenomenon only.

Néel[7] successfully explained the magnetic properties of ferrimagnetic materials by assuming three types of superexchange forces. There are A-A interaction, A-B interaction, and B-B interaction. These superexchange forces have a negative spin interaction. The magnetic moment of magnetite is then explained as follows. Magnetite has the inverse spinel structure $Fe_8^{+3}[Fe_8^{+2}Fe_8^{+3}]O_{32}$. There are five unpaired electrons in Fe^{+3} and four unpaired electrons in Fe^{++}, contributing to the magnetic moment of magnetite. The moment of the 8 Fe^{+3} on the A sites is aligned antiparallel with the moment of the 8 Fe^{+3} and 8 Fe^{+2} on the B sites. Since the 8 Fe^{+3} cations on the A sites cancel the moment of the 8 Fe^{+3} on the B sites, the net moment is due to the moment of the 8 Fe^{+2} which are aligned parallel with each other. This gives rise to a magnetic moment of 8 x 4 = 32 Bohr magnetons per unit cell, or 4 Bohr magnetons per Fe_3O_4 group. The experimental saturation moment has been found to be 4.2 Bohr magnetons.

As stated above, the ferrites of zinc and cadmium have the normal spinel structure. The Zn and Cd ions are diamagnetic so that the A sublattice has no moment. At room temperature the 16 iron ions with 5 unpaired electrons each are paramagnetic, since there is no A-B interaction to give rise to ferrimagnetism.

The fact that magnetite or lodestone has magnetic properties has been known for centuries. However, ferrites have become of commercial importance as magnetic devices in electrical circuits only relatively recently. This development was mainly due to the work of Snoek[8] at the Philip Re-

search Laboratories, where he found that the magnetic properties of the spinels could be altered by mixing various ferrites in different proportions. Snoek found that when $NiFe_2O_4$, an inverted spinel, was combined with $ZnFe_2O_4$, a normal spinel, the permeability was greatly increased. This is accompanied by the lowering of the Curie temperature, the temperature at which the ferrite ceases to be ferrimagnetic. This discovery led to research in other mixed ferrites such as those of Co, Ni, Zn, Mg, Mn, Li, and Fe, and even to the study of mixed spinels such as the ferrites and the aluminates.

A number of papers have appeared in the literature in recent years pertaining to the investigation of the above systems. In general, the investigations can be classified into two categories: (1) those dealing with the magnetic properties, and (2) those dealing with the physical, crystallographic, and chemical properties. The way in which the problem is attacked depends upon the interests of the researcher.

Ferrites are usually prepared by mixing the constituent oxides in the desired proportions, pressing the mixed oxides into varying shapes, and heating to form the ferrite by reaction in the solid state. The properties of the material formed in this way are sensitive to the method of preparation. Different magnetic properties can be obtained, for example, by changing the heating time and temperature at which the reaction is carried out. The purpose of this study was to obtain information about the reactions involved in ferrite formation, so that information could be obtained about the factors involved in the preparation procedure which might affect the magnetic properties of the cores. For this reason, some of the magnetic properties as well as chemical properties have been investigated. The emphasis, however, was placed on studying the solid-state reactions rather than on investigating the magnetic properties resulting from the solid-state reactions.

The magnetic properties to which reference is made in this report are the initial permeability, μ; the loss factor, Q; the saturation moment per unit mass, σ_s; and the Curie temperature. The magnetic induction in gauss, B, is given by $B = H + 4\pi I$, where H in oersteds is the applied field and I is the magnetic moment per unit volume in emu. The initial permeability is defined as $B/H = 1 + 4\pi\chi$, where χ is the volume susceptibility. The magnetic moment per unit mass, σ, is obtained by dividing the moment per unit volume, I, by the density of the material. The Curie temperature is the temperature at which the sample ceases to be ferromagnetic.

The initial permeability is a measure of the energy supplied to the material. The loss factor, Q, is a measure of the energy returned by the material. The product of the initial permeability and the loss factor, μQ, often called the quality factor, is a measure of the worth of the material, since a large μ and Q are desirable.

The permeability and loss factors are highly dependent on the method of preparation of the sample and are not constants of the material. The Curie temperature is a physical constant characteristic of a given material, much as the melting point is characteristic of a crystalline solid. The saturation moment is also characteristic of the material. For this reason these properties can be used in the analysis of magnetic materials.

2. PHASE RELATIONSHIPS AND MAGNETIC PROPERTIES OF SEVERAL FERRITES

2.1 THE SYSTEM $Ni_{.474}Zn_{.526}Fe_2O_4$-FeO-$Fe_2O_3$

Since the magnetic properties of ferrites are sensitive to the impurities in the specimen, both in solid solution and as a second phase, it is important to know the phase relationships that exist between the component oxides from which the ferrites are made. The ferrites utilized as ferromagnetic elements in electric circuits have the advantages of high permeability combined with high resistivity. One detrimental factor which contributes to the lowering of the resistivity is ferrous iron in the structure.[9] Ferrous iron also affects the anisotropy and magnetostriction which in turn affect the permeability. It is therefore necessary to understand the conditions under which it forms in order to control the magnetic properties of the ferrites.

In general, it may be said that ferrites such as $MeFe_2O_4$ and $Me'Fe_2O_4$, where Me and Me' designate a divalent cation, form continuous solid solutions over their entire composition range. This fact has been used repeatedly to make ferrites with varying magnetic properties, depending on the particular choice for Me and Me' and the relative amounts of each.

The possibility exists, when starting with the oxides MeO and Fe_2O_3, of forming the compound $Me_x^{+2}Fe_{1-x}^{+2}Fe_2O_4$, if the conditions are right for reduction of Fe_2O_3 to occur. The reaction $3Fe_2O_3 \rightarrow 2Fe_3O_4 + 1/2\ O_2$ occurs in air at one atmosphere at 1392°C. The addition of a second oxide, however, can lower the temperature at which Fe_2O_3 is reduced to Fe_3O_4. This will be discussed in detail later. It is sufficient to note at this time that in a mixture of Fe_2O_3 and MeO reduction of the Fe_2O_3 occurs at relatively moderate temperatures. It can be seen that the system is a ternary

system with the components MeO, FeO, and Fe_2O_3. When Me also has two common valences as in the system MnO-Fe_2O_3, the system is further complicated. Such systems are not considered here.

When (Ni, Zn)O and Fe_2O_3 are mixed in a 1:1 mole ratio, the equilibrium composition should be the stoichiometric ferrite containing no ferrous iron. There are two conditions under which ferrous iron can form in the ferrite. The formation of ferrous iron below a temperature of about 1300°C is caused by the inhomogeneity of the material. The extent to which ferrous iron is found in the sample is dependent upon the heating time and the extent to which the oxides are mixed prior to heating. Figure 1 shows the ferrous iron content of a 1:1 mole mixture of (Ni, Zn)O and Fe_2O_3 as a function of the reaction time for two different mixing procedures. The amount of ferrous iron in the well-mixed sample decreases with heating time. The amount of ferrous iron in the poorly mixed sample also decreases with heating time, but much more slowly.

The requirement for the formation of ferrous iron in air at 1210°C is that (Ni,Zn)O and Fe_2O_3 be present in local areas in a mole ratio other than 1:1. In the initial heating period, the spinel structure is formed and since the oxides are distributed in a nonstoichiometric ratio, ferrous iron is formed in the regions where Fe_2O_3 is in excess. After prolonged heating, diffusion of (Ni,Zn)O into the ferrite results in the oxidation of the ferrous iron with the formation of more $(Ni,Zn)Fe_2O_4$.

Above 1300°C the formation of ferrous iron in stoichiometric material is due to the decomposition of the ferrite. If (Ni,Zn)O is not lost to the system, a second phase will appear. Van Uitert[10] and Brownlow[11] have shown that volatilization of zinc occurs in material containing ZnO which leaves the material with an excess of Fe_2O_3. The amount of ferrous iron formed by this mechanism increases rather than decreases with reaction time

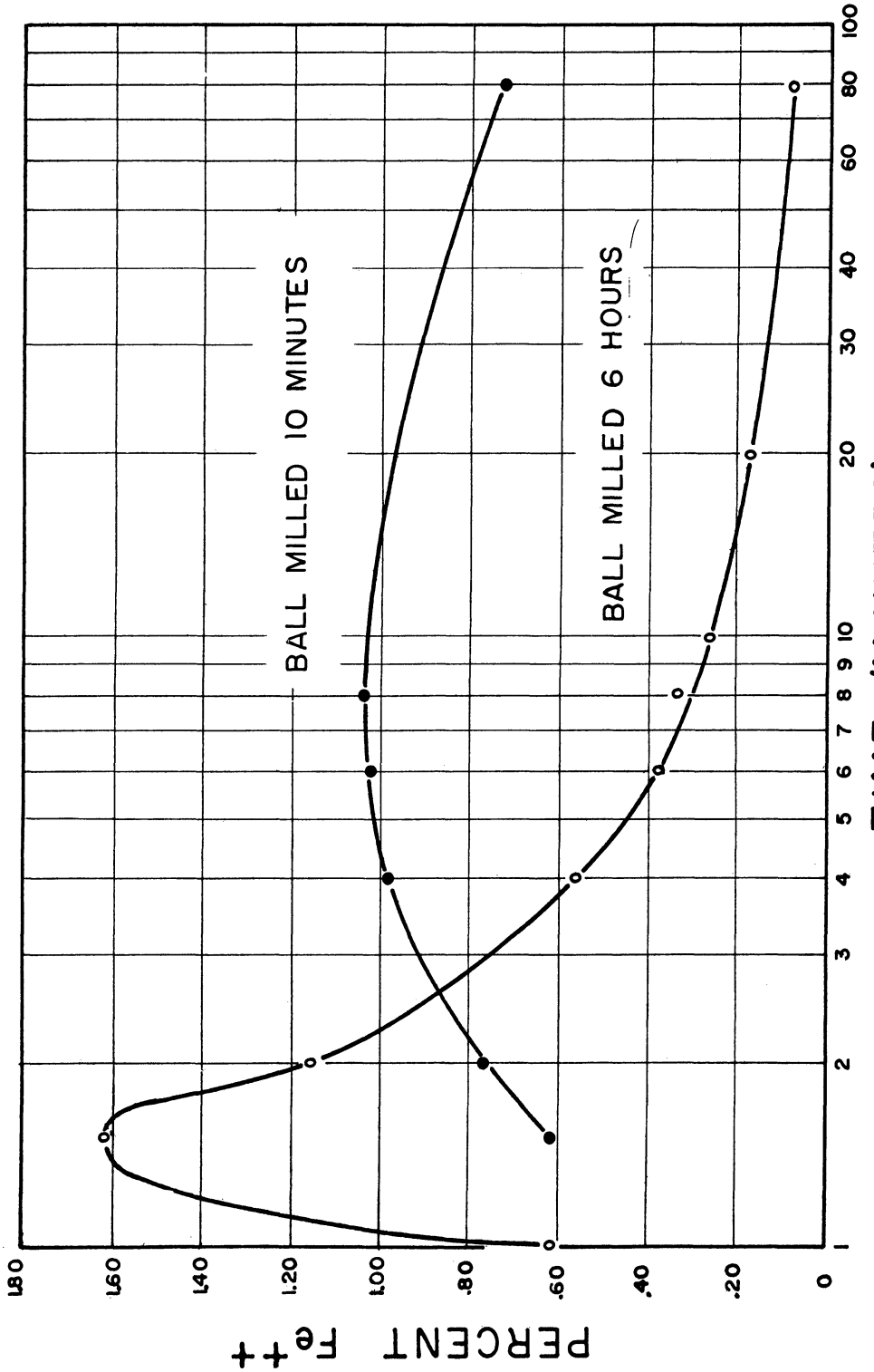

Fig. 1. Percent ferrous iron vs. reaction time for $Ni_{.4}Zn_{.6}Fe_2O_4$; 1210°C.

as occurs in the first case.

Kato and Takei[12] attribute the magnetic properties of sintered ZnO and Fe_2O_3 containing a large amount of Fe_2O_3 either to the formation of Fe_3O_4 in solid solution with the $ZnFe_2O_4$, or to the formation of Fe_2O_3 as a magnetic second phase, depending upon the method of preparation. Kushima and Amanuma[13] investigated the same system and concluded that while some Fe_2O_3 is converted to Fe_3O_4, the magnetic properties of the Fe_2O_3-rich material are due to Fe_2O_3 in solid solution with $ZnFe_2O_4$.

Roberts and Merwin[14] investigated the system MgO-FeO-Fe_2O_3 in air at one atmosphere. In the system FeO-Fe_2O_3, above 1386 ± 5°C, the stable phase was found to be a magnetite solid solution containing excess oxygen, while below this temperature the stable phase is a hematite solid solution containing less oxygen than Fe_2O_3. The solubility of MgO in $MgFe_2O_4$ was found to be about 1% from 1750°C to 1000°C.

Berger[15] investigated the ZnO-Fe_2O_3 system and determined the solubility of Fe_2O_3 in zinc ferrite by measurement of the lattice constant. He found the composition of the stable phase to be 76 mole % Fe_2O_3 at 1400°C, 64 mole % Fe_2O_3 at 1200°C, and about 61 mole % Fe_2O_3 at 1000°C. From density considerations he concluded that the solid solution contained lattice holes, which could be accounted for by assuming the presence of γFe_2O_3.

Smolenski[16] investigated the solid solutions of $Ni_{.3}Zn_{.7}Fe_2O_4$-Fe_2O_3 and attempted to explain the magnetic properties on the basis of Néel's theory. He found that, with increasing Fe_2O_3 content, the saturation magnetization increased for a time and then decreased. The Curie temperature increased and the magnetic permeability decreased. The Fe_2O_3 in solid solution with $Ni_{.3}Zn_{.7}Fe_2O_4$ is stated to be γFe_2O_3. The basis for this conclusion is not given.

Toropov, Rabkin, Freingenfeld, and Epstein[17] investigated the system $NiO-ZnO-Fe_2O_3$ and attempted to correlate the phase composition with the magnetic properties. They plotted a ternary diagram of the system $NiO-ZnO-Fe_2O_3$, showing the area of solid solutions. The firing temperature is given as 1350-1400°C. They make the statement that the effect of changing the temperature is to change the amount of Fe_3O_4 and to change the extent of solid solution.

The purpose of this investigation is to extend these studies and to determine the equilibrium phase compositions of the system $Ni_xZn_{1-x}Fe_2O_4-Fe_2O_3$ in air at one atmosphere. The value of x was arbitrarily held constant at .474, while the amount of Fe_2O_3 in the initial composition was varied. Methods used to identify the composition and phase of the sintered oxides were (1) direct chemical analysis, (2) visual microscopic examination, (3) Curie temperature determinations, and (4) X-ray diffractional analysis.

2.1.1 Preparation and Measurement of Samples.—The compositions investigated are given in Table I. All samples were prepared by ball-milling the C.P. oxides in acetone for 6 hours, decanting the acetone and air-drying the oxides at 100°. The dried oxides were then pressed into toroids and fired in air in an electric globar furnace, the temperature of which was stabilized to ± 5°. Firing temperatures were determined with a calibrated platinum versus platinum + 10% rhodium thermocouple. The samples used for the study were fired with time on temperature varying from 3 hours at 1400° to 5 days at 1000°. Samples prepared for chemical analysis at equilibrium temperatures less than 1000° were prefired for 4 hours at 1150° and then crushed in a "Diamond Mortar" and refired as a powder at the desired temperature for 24 hours. All samples were quenched to room temperature by rapid immersion in water.

TABLE I

INITIAL COMPOSITIONS

Composition	Moles ZnO	Moles NiO	Moles Fe_2O_3
1	.526	.474	1.000
2	.526	.474	1.135
3	.526	.474	1.294
4	.526	.474	1.570
5	.526	.474	1.938
6	.526	.474	3.000
7	.526	.474	4.00
8	.526	.474	5.00
9	.526	.474	6.00
10	.000	.000	1.00

To insure the reliability of these data as representing equilibrium values, it was essential to insure that factors such as mixing, time of firing, and possible oxidation during cooling to room temperature were properly controlled. Quantitative experiments indicated that a rapid quench was necessary. This was obtained by immersing the samples in water. As might be expected, samples allowed to cool in air from 1200° indicated upon analysis only 5 to 50% of the ferrous iron content of water-quenched samples. The ferrous iron content was clearly dependent upon the porosity of the pressed cores. Table II shows the effect of the cooling method on ferrous iron content. Experiments on the effect of reaction time on the ferrous iron content revealed that at a temperature of 1200°, 80% of the ferrous iron present after 15 hours was formed within 3 minutes, and 99% within 20 minutes. These data are given in Table III.

TABLE II

FACTORS INFLUENCING THE EXTENT OF OXIDATION DURING THE COOLING PROCESS

$Ni_{.474}Zn_{.526}Fe_2O_4 + .938\ Fe_2O_3$ T = 1210°C

		Cooling Method	Wt. % Fe^{++}
Material pressed into core			
Core thickness	.703 cm	Air-cooled	3.39
Core thickness	.107 cm	Air-cooled	.72
Core thickness	1.66 cm	Water-quenched	6.32
Material fired as loose		Air-cooled	.35
powder		Water-quenched	6.85

TABLE III

FERROUS IRON CONTENT OF MATERIAL AS A FUNCTION OF REACTION TIME,

WATER-QUENCHED FROM 1210°C

$Ni_{.474}Zn_{.526}Fe_2O_4 + .938\ Fe_2O_3$

Firing Time (min)	Wt. % Fe^{++}
3	5.29
5	6.34
10	6.31
20	6.44
900	6.55

Ferrous iron determinations were made by dissolving the ferrite in a olution of .05 N $SnCl_2$ in concentrated HCl under an atmosphere of oxygen-free CO_2. The amount of ferrous iron was then determined by titration with $K_2Cr_2O_7$. The procedure is described in detail in Appendix I. The samples were prepared for microscopic examination by mounting in bakelite and polishing according to standard metallographic techniques.

The Curie temperatures were obtained by measuring the fall-off of $K\sqrt{\mu_1^2+\mu_2^2}$ with temperature, where μ_1 is the real part and μ_2 is the imaginary part of the initial permeability. The Curie temperature is identified here as the temperature at which the permeability reaches its peak and begins to fall off toward unity. A typical curve of $K\sqrt{\mu_1^2+\mu_2^2}$ vs. temperature is given in Fig. 2.

2.1.2. Results and Conclusions.—Table IV gives the mole ratio Fe_3O_4:$Ni_{.474}Zn_{.526}Fe_2O_4$ based on chemical analysis for the ferrous iron content of samples sintered at various temperatures and water-quenched. This ratio for any given material increases with temperature, and approaches the value indicated as the stoichiometric limit, which is the value that the sample would have if the excess Fe_2O_3 were completely converted to Fe_3O_4. The method used in calculating this ratio is given in Appendix II.

The Curie temperatures of the samples are given in Table V. These data are plotted against the initial compositions in Fig. 3. From this plot the limiting composition of the homogeneous solid solution at the boundary lines between the one-phase and two-phase area at 1000, 1100, 1200, and 1300° can be obtained. From these data the phase diagram in Fig. 4 was obtained. The additional information obtained by microscopic examination of the material provides excellent confirmation of the position of this boundary. The Curie points for the $Ni_{.474}Zn_{.526}Fe_2O_4$-$Fe_3O_4$ solid solutions will be seen to lie linearly between those of the extreme compositions, i.e., $Ni_{.474}Zn_{.526}Fe_2O_4$ and Fe_3O_4. Because of this, it is reasonable to express the composition of this phase in terms of these substances.

The data in Table IV indicate that the composition of the spinel phase in the one-phase area consists of a solid solution of $Ni_xZn_{1-x}Fe_2O_4$, Fe_3O_4, and Fe_2O_3. This is in agreement with the findings of Roberts and Merwin[14]

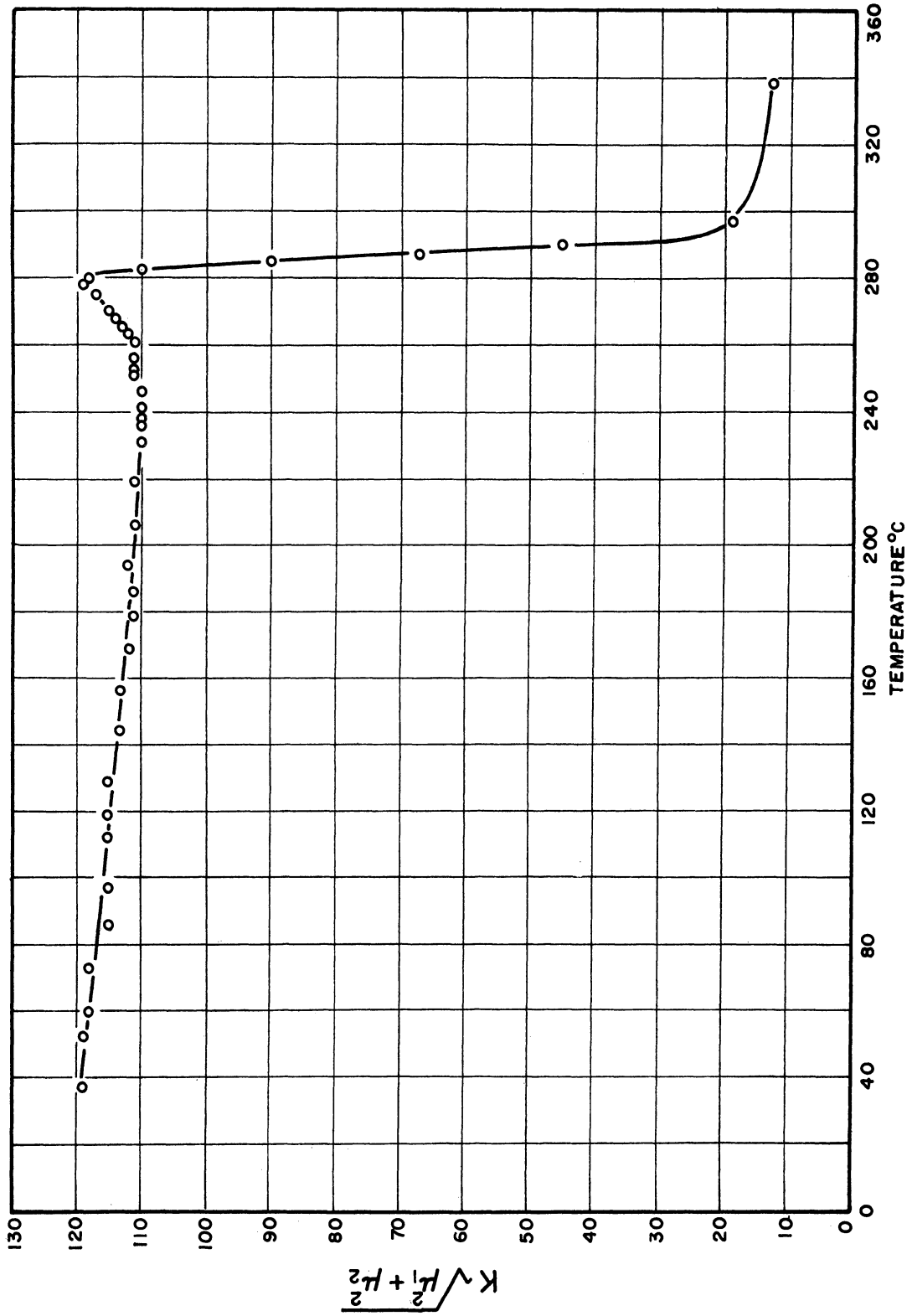

Fig. 2. $K\sqrt{\mu_1^2 + \mu_2^2}$ vs. temperature for $Ni_{.474}Zn_{.526}Fe_2O_4$ + $.294Fe_2O_3$ fired at 1000°C.

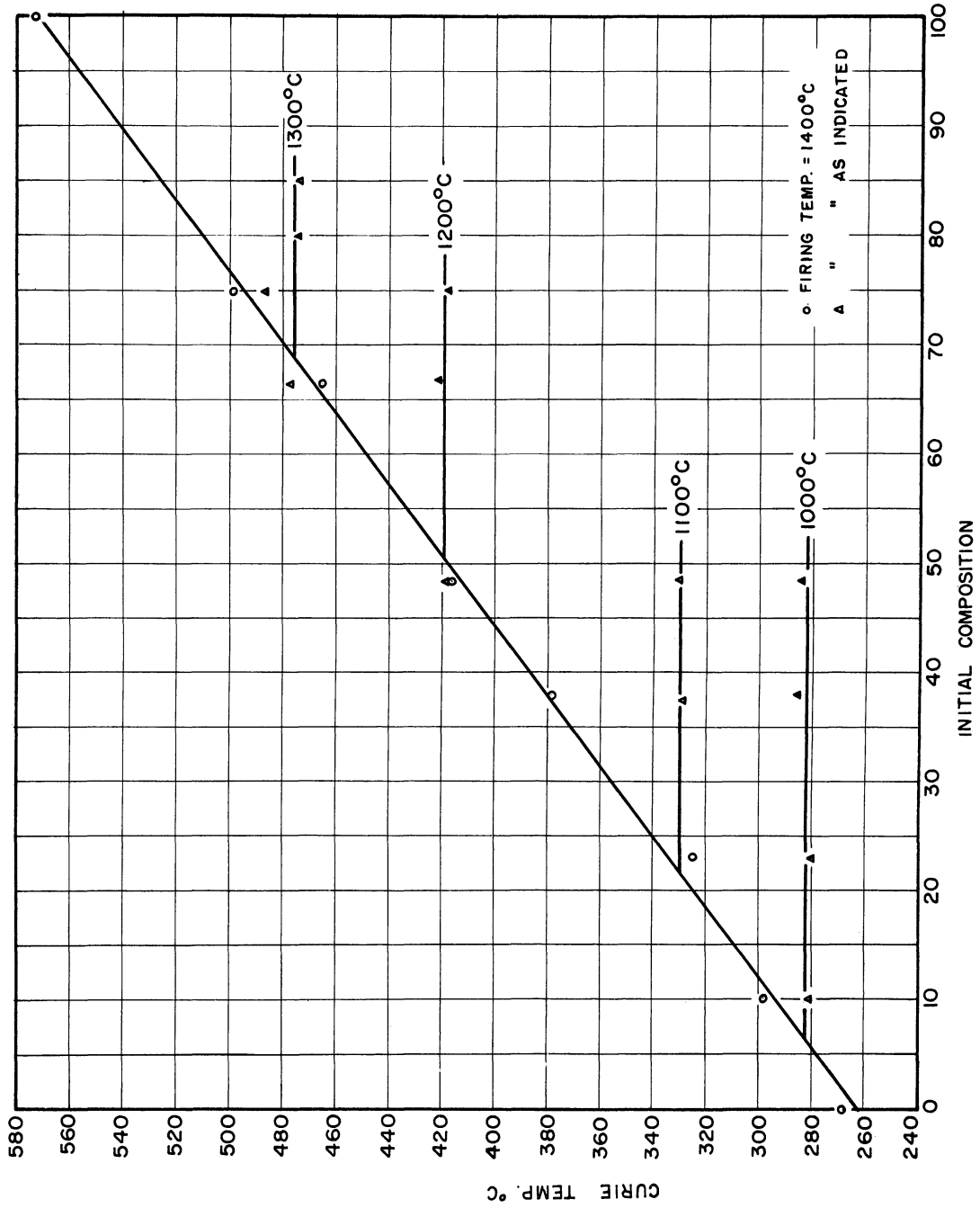

Fig. 3. Curie temperature vs. initial composition.

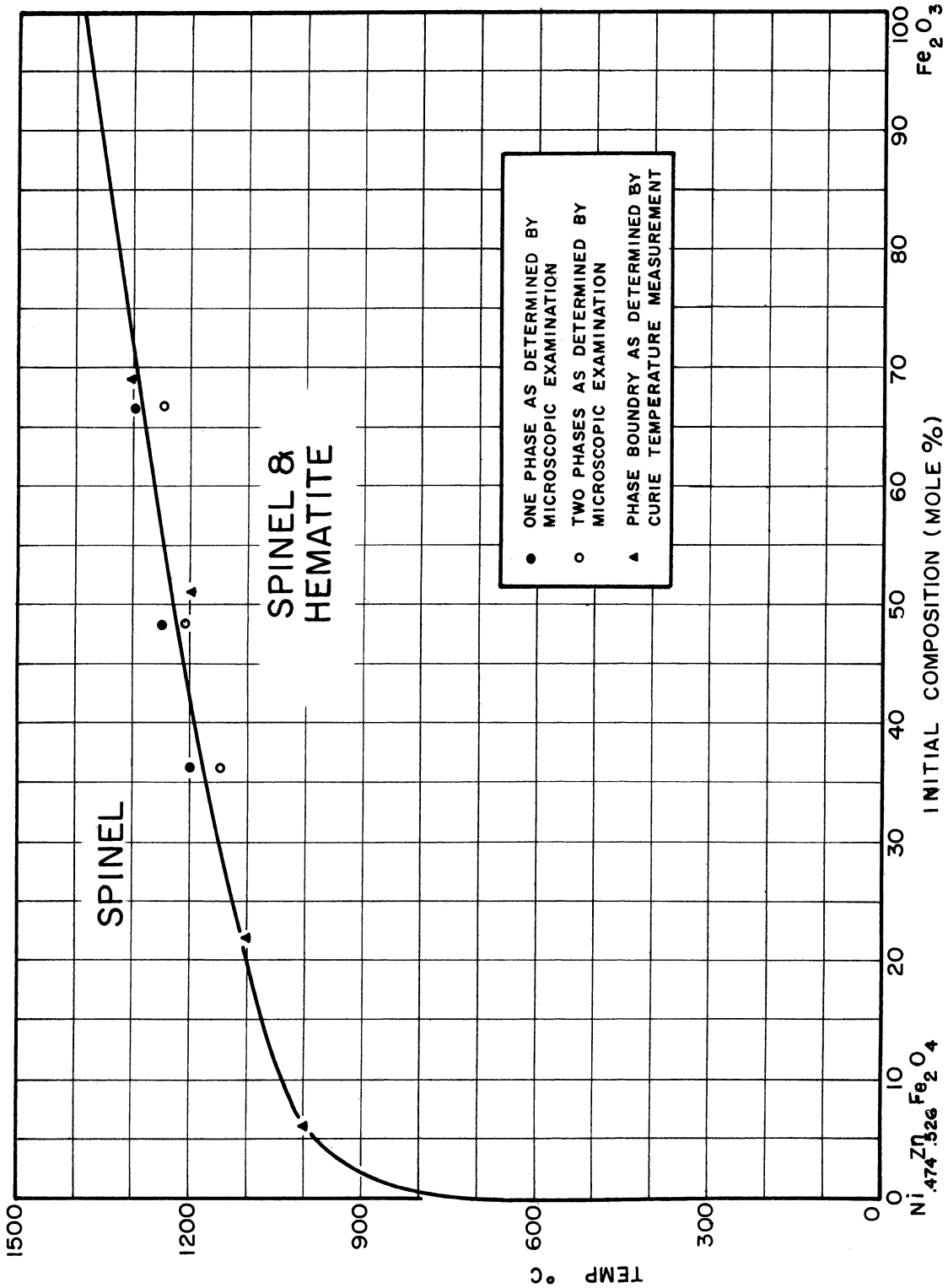

Fig. 4. The phase diagram for $Ni_{.474}Zn_{.526}Fe_2O_4$-$Fe_2O_3$.

TABLE IV

THE MOLE RATIO Fe_3O_4:$Ni_{.474}Zn_{.526}Fe_2O_4$ AS A FUNCTION OF INITIAL COMPOSITION $Ni_{.474}Zn_{.526}Fe_2O_4 + BFe_2O_3$

Temperature	B = .135	B = .294	B = .938	B = 2.00
700	.004	.004		
800	.015	.012		
900	.035	.028		
1000	.06	.050	.054	.051
1050		.083	.079	.090
1100	.085	.143	.142	.149
1150		.159	.237	.247
1200		.175	.412	.431
1250		.180	.509	.688
1300		.187	.542	1.07
1350		.190	.570	1.15
1400		.194	.585	1.20
Theoretical Limit	.09	.196	.625	1.33

TABLE V

CURIE TEMPERATURE OF SAMPLES WITH AN INITIAL COMPOSITION OF $Ni_{.474}Zn_{.526}Fe_2O_4 + BFe_2O_3$

B	900°C	1000°C	1100°C	1200°C	1300°C	1400°C
0		230	259	256	261	268
.135	276	280	293	280	280	298
.294	272	280	322	327	328	325
.570	267	286	328	380	368	374
.938	260	284	330	418	424	416
2.000				421	477	465
3.000				418	486	498
4.000					474	
5.667					474	
Pure Fe_2O_3						577*

*Prepared at 1425°C.

in the system MgO-FeO-Fe_2O_3. The composition of the spinel phase may be represented as (neglecting cation and anion vacancies):

$$aNi_xZn_{1-x}Fe_2O_4 \cdot bFe_3O_4 \cdot cFe_2O_3 \qquad (1)$$

The mole ratio b/a represents the solubility of Fe_3O_4 in the Ni-Zn ferrite solid solution. Beyond the solubility boundary a second phase, identified as αFe_2O_3 (hematite) by X-ray analysis, separates. This two-phase area is shown in Fig. 5. Throughout the two-phase region, this solubility (b/a) would be expected to remain constant at a given temperature. This is verified within experimental error from the data over the two-phase region presented in Table IV. The value b/(b+c) can be interpreted as a measure of the amount of excess oxygen in the spinel phase. The calculation of this ratio at the boundary line between the spinel field and the spinel-hematite field can be done as follows. In the two-phase area the overall composition of the system can be given as:

$$aNi_xZn_{1-x}Fe_2O_4 \cdot bFe_3O_4 \cdot cFe_2O_3 + dFe_2O_3 \quad . \qquad (2)$$

The ratio b/(b+c+d) can be calculated from a knowledge of the initial composition and the ferrous iron content. The procedure for this calculation is given in Appendix II. In the one-phase area d = o, and the ratio becomes b/(b+c). As the temperature is increased further, c approaches zero and the ratio approaches unity. The value of b/(b+c+d) has been plotted in Fig. 6 for 3 compositions. The temperature at which the second phase disappears has been marked. It can be seen that the value of b/(b+c) at this temperature is 0.7 for all compositions.

Darken and Gurry[18] found that magnetite prepared in air contained excess oxygen. At the boundary between the magnetite and hematite phase and the magnetite field, which occurs at 1392° in air, the composition of the magnetite phase in terms of the components Fe_3O_4 and Fe_2O_3 was found to be

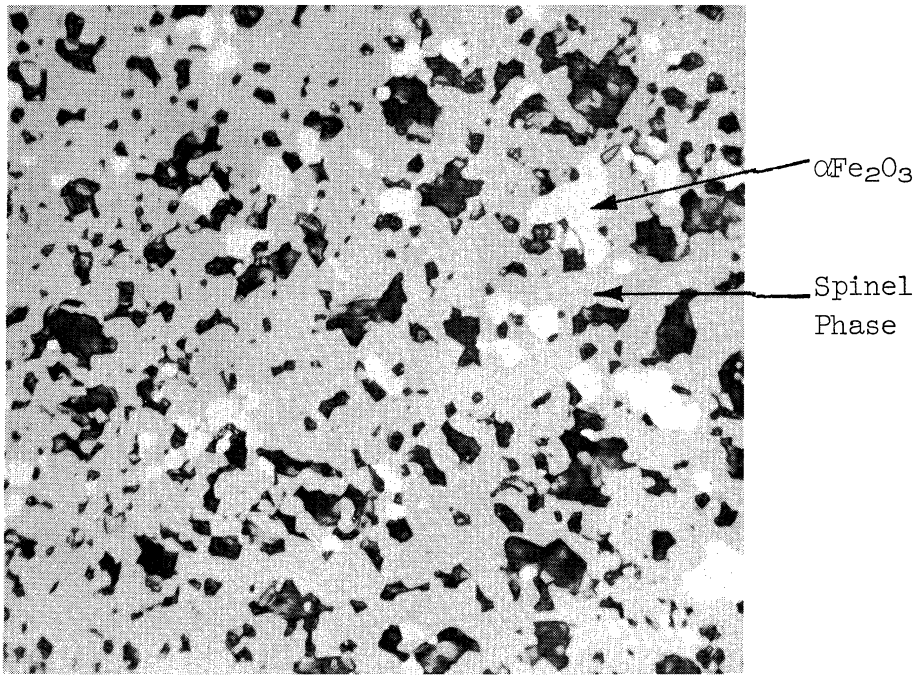

Polished, not etched (X1000)

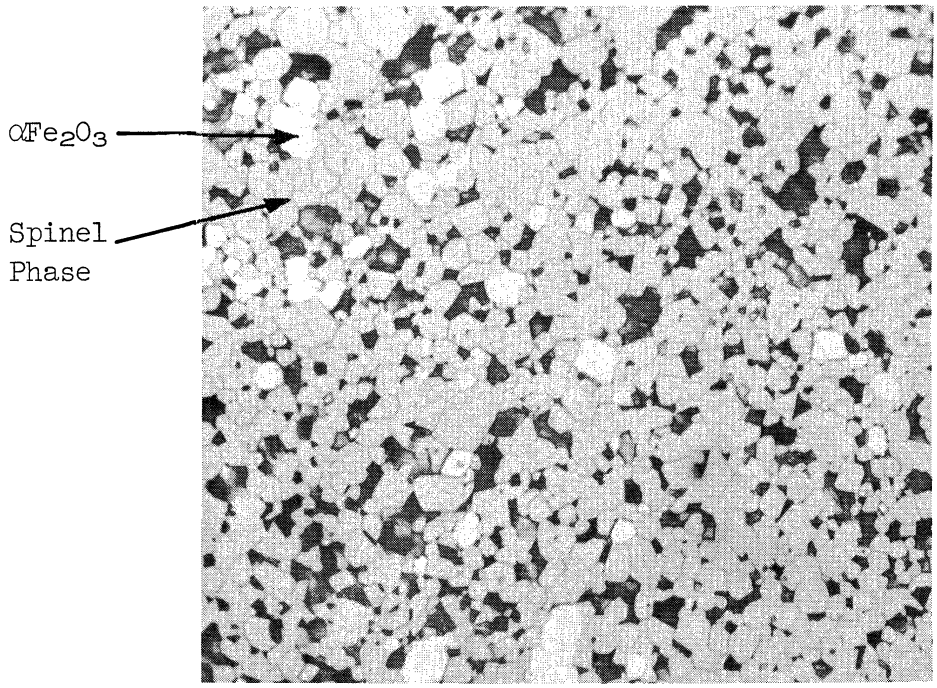

Polished and etched (X1000)

Fig. 5. Photomicrographs of the spinel-hematite field.

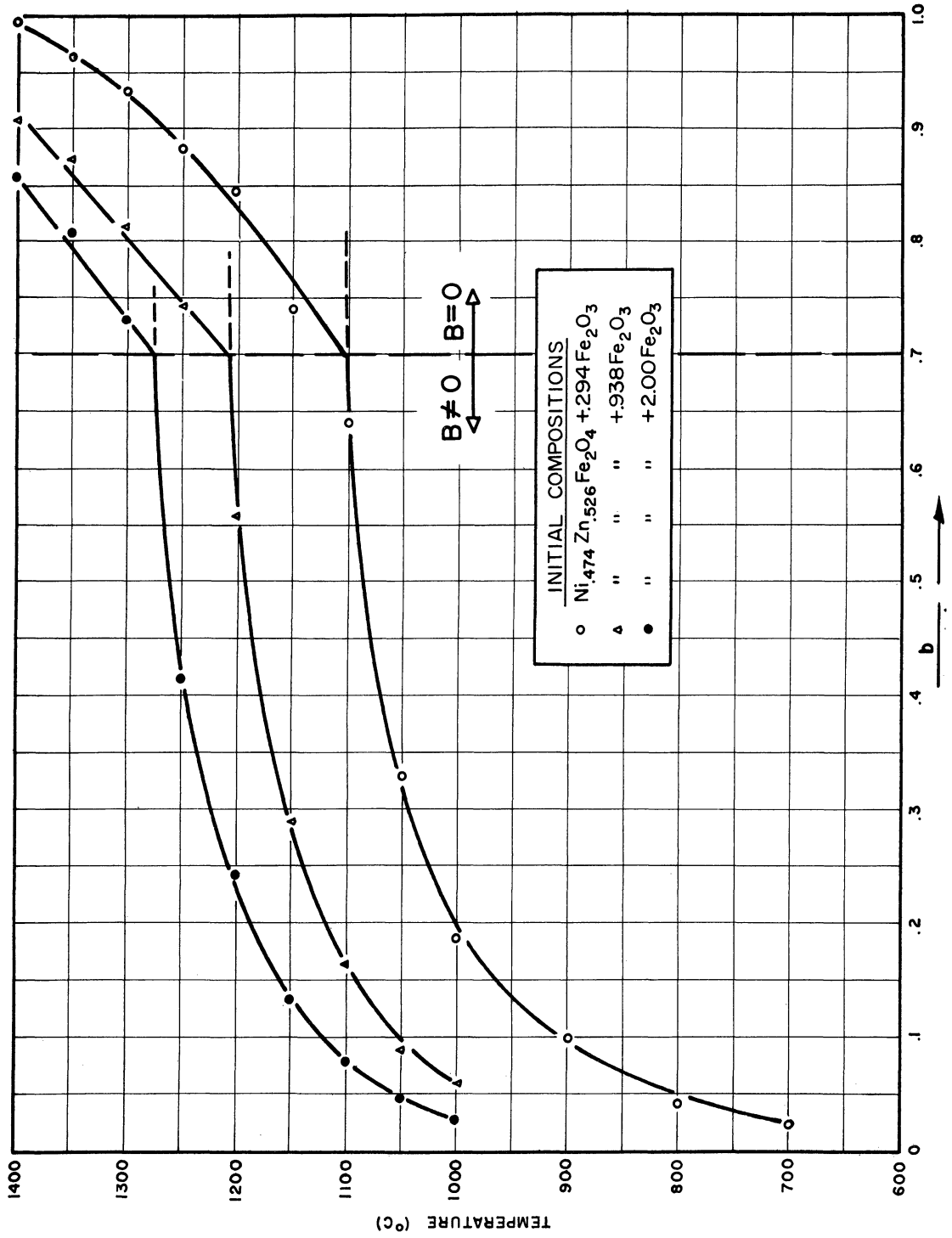

Fig. 6. b/(b+c+d) of Eq. (2) vs. temperature for 3 compositions.

0.7 mole fraction Fe_3O_4. In the notation of Eq. (1), this corresponds to:

$$bFe_3O_4 \cdot cFe_2O_3 \quad . \tag{3}$$

It is found here that the mole fraction of Fe_3O_4 = b/(b+c) = 0.7. Since Eq. (3) is identical to Eq. (1), where a = o, it appears that this ratio is independent of the value of a of Eq. (1) throughout the composition range.

2.2 THE SYSTEM $LiFeO_2$-FeO-Fe_2O_3

The ferrospinel $LiFe_5O_8$ was first reported by Hoffman,[19] who prepared the compound from Li_2O and Fe_2O_3 in a mole ratio of 1:5. The structure of the compound has aroused much interest. The unit cell is given as $Fe_8^{+3}[Fe_{12}^{+3}Li_4^{+1}]O_{32}$. Braun[20] has shown that the lithium ions are ordered on the B sublattice below 755°C. At this temperature they become disordered and become ordered again on cooling at 735°C. Braun, as well as David and Welch,[21] found that $LiFe_5O_8$ and γFe_2O_3 have practically the same X-ray pattern. The similarity between the two structures is apparent when we compare $Fe_8^{+3}[Fe_{12}^{+3}Li_4^{+1}]O_{32}$ and $Fe_8^{+3}[Fe_{12}^{+3}\square_4]O_{28}(OH)_4$. It has been proposed that the composition of γFe_2O_3 is somewhere between $Fe_8^{+3}[Fe_{13\frac{1}{3}}^{+3}\square_{2\frac{2}{3}}]O_{32}$ and $Fe_8^{+3}[Fe_{12}^{+3}\square_4]O_{28}(OH)_4$. The difference in the X-ray photographs of $LiFe_5O_8$ and γFe_2O_3 due to the scattering of the light lithium ion would be expected to be slight.

In addition to $LiFe_5O_8$, Li_2O and Fe_2O_3 form a second binary compound, when mixed in the mole ratio of 1:1. This compound, $LiFeO_2$, has the NaCl structure. Collongues and Chaudron[22] investigated these oxides and concluded that both $LiFe_5O_8$ and $LiFeO_2$ are the limiting members of the solid solutions formed by the replacement of $2Fe^{+2}$ by $Li^{+1}Fe^{+3}$ in Fe_3O_4 and FeO, respectively.

A partial phase diagram of the system $LiFeO_2$-FeO-Fe_2O_3 has been worked out for the system in air at one atmosphere of pressure.

2.2.1 Preparation and Measurement of Samples.—The samples used in this study were prepared in the same way as described for the system $Ni_{.474}Zn_{.526}Fe_2O_4$-$Fe_3O_4$. C.P. lithium carbonate and ferric oxide were weighed out in the mole ratios given in Table VI, and mixed by ball-milling in acetone for 6 hours. After drying, the oxides were pressed into compacts and heated at temperatures of from 1000 to 1500°C for times varying from 4 hours at 1000° to 3 minutes at 1500°. All samples were water-quenched.

The compositions of the samples after heating were calculated from the ferrous iron analysis. The samples were readily dissolved in concentrated HCl, so that the use of $SnCl_2$ was not necessary. With this exception, the procedure for the analysis of ferrous iron was as described in Appendix I for the Ni-Zn ferrite system. The procedure used to calculate the compositions in terms of the components $LiFeO_2$, FeO, and Fe_2O_3 is given in Appendix II. Phase identification was made by microscopic examination and X-ray analysis.

2.2.2 Results and Conclusions.—The ternary phase diagram for the system is shown in Fig. 7. Because of the nature of the diagram, it is not easily plotted as a pseudo-binary system, as is the Ni-Zn ferrite system. In the area designated as A, two phases co-exist at equilibrium. They are the ferrite phase, consisting of the $LiFe_5O_8$-Fe_3O_4 solid solution, and the hematite phase. The composition of the ferrite phase is $LiFe_5O_8 \cdot x(7Fe_3O_4 \cdot 3Fe_2O_3)$, where x is a function of the temperature. The ratio Fe_3O_4:Fe_2O_3 = 7:3 is identical to that obtained in the Ni-Zn ferrite system.

TABLE VI

INITIAL COMPOSITIONS

Composition No.	Mole % Li_2CO_3	Mole % Fe_2O_3
1	50.00	50.00
2	45.45	54.55
3	40.00	60.00
4	32.16	67.84
5	25.00	75.00
6	20.00	80.00
7	18.18	81.82
8	16.67	83.33
9	16.34	83.66
10	16.07	83.93
11	15.38	84.62
12	14.58	85.42
13	14.29	85.71
14	12.82	87.18
15	11.11	88.89
16	9.38	90.62
17	7.14	92.86
18	4.17	95.83
19	2.27	97.73
20	0	100.

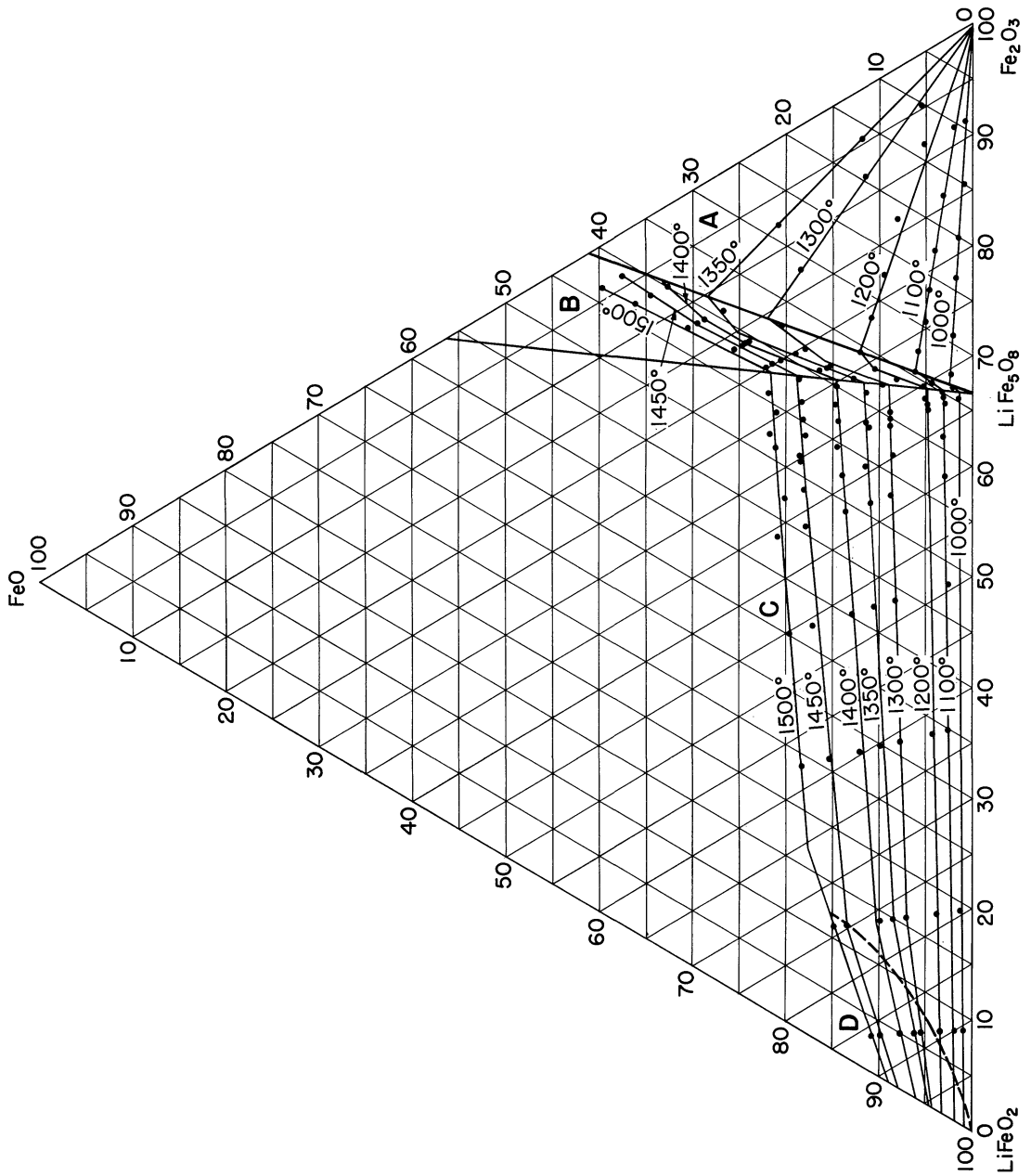

Fig. 7. Phase diagram for the system $LiFeO_2$-FeO-Fe_2O_3.

The area designated by B consists of a one-phase area of solid solution between lithium ferrite on the one hand and magnetite of varying composition on the other. This area is enclosed by lines connecting $LiFe_5O_8$ and the compositions $79FeFe_2O_4 \cdot 21FeO$ and $7FeFe_2O_4 \cdot 3Fe_2O_3$. It generally has been found that the solubility of MeO in the spinels, where Me is a divalent cation, is of the order of 1% or less. In the system $LiFe_5O_8$-Fe_3O_4, however, the solubility of FeO is considerably greater.

The area designated by C is a two-phase area consisting of the solid solution $LiFeO_2$-FeO and the solid solution $LiFe_5O_8$-$FeFe_2O_4$. The area D is a one-phase area of solid solution between $LiFeO_2$ and FeO. The exact location of this boundary has not been determined. The boundary was put in by dashed lines at a position it appears to have from the ferrous iron content. The compounds $LiFeO_2$ and FeO are paramagnetic. It is likely, but not certain, that their solid solutions are also paramagnetic. However, the samples located in this area were found to have a higher moment than can be explained by the paramagnetic properties of the oxides. Since this area is not of particular interest in the study of ferrite systems, the exact identification of the boundary was not attempted. Samples from different areas in the phase diagram are illustrated in Fig. 8.

This phase study points out the fact that the stoichiometric binary compound $LiFe_5O_8$ can be prepared only at temperatures below 1000°C. At this temperature and above, dissociation of $LiFe_5O_8$ occurs, with the formation of $LiFeO_2$ and Fe_2O_3 as follows:

$$LiFe_5O_8 \rightarrow LiFeO_2 + 2Fe_2O_3$$

The Fe_2O_3 goes into solid solution with the $LiFeO_2$ and $LiFe_5O_8$ as FeO and Fe_3O_4, respectively.

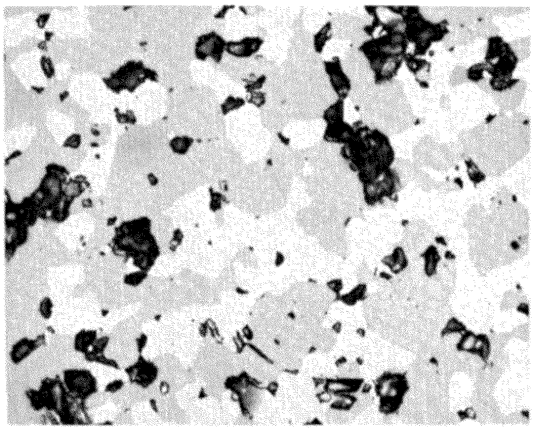

AREA (A)

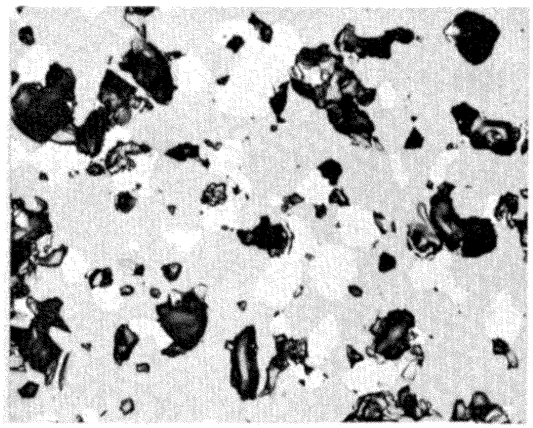

AREA (A)

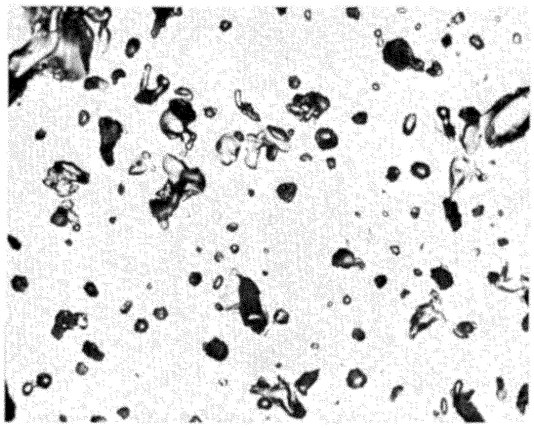

AREA (B)

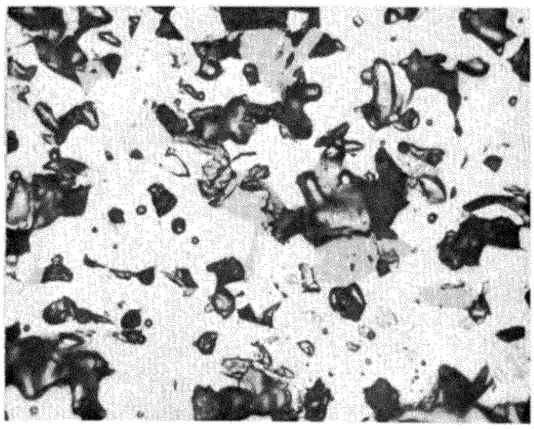

AREA (C)

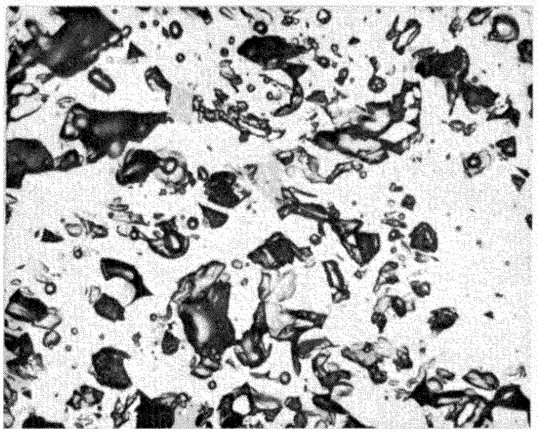

AREA (C)

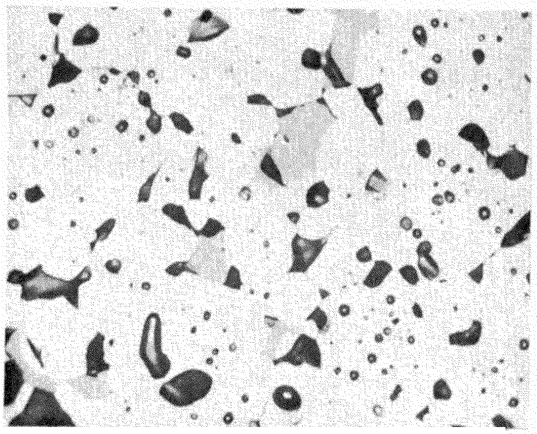

AREA (C)

Fig. 8. Photomicrographs of samples from different areas in the $LiFeO_2$-FeO-Fe_2O_3 system (X600).

2.3 SOME MAGNETIC PROPERTIES OF Ni-Zn FERRITES

2.3.1 Preparation and Measurement of Samples.—Some magnetic properties of ferrites have been measured and the results are reported below. The measurements were made on samples prepared by pressing the mixed oxides into toroids and heating in air for different lengths of time at different temperatures. Most of the samples were cooled to room temperature by quenching in air. Some samples, however, were quenched in water. The method of cooling has been specified in each case. The magnetic measurements were made on a Boonton Radio Corporation, Type 260-A, Q-meter with a frequency range of 50 kc to 50 mc.

2.3.2 The System $Ni_xZn_{1-x}Fe_2O_4$.—$NiFe_2O_4$ is ferrimagnetic, but has a relatively low permeability, while $ZnFe_2O_4$ is paramagnetic. When, however, the two ferrites are mixed to form the composition $Ni_xZn_{1-x}Fe_2O_4$, a magnetic ferrite can be obtained, with the proper choice of x, which has a relatively high initial permeability. This is presumably due to the decrease in the anistropy which accompanies the decrease in the Curie temperature. The permeability and Q of the Ni-Zn ferrites are plotted as a function of composition in Fig. 9. The Curie temperatures are plotted as a function of composition in Fig. 10. A considerable amount of information on the magnetic properties of Ni-Zn ferrites is given in the literature.

It is of interest to determine the effect of the addition of NiO and ZnO in excess of the stoichiometric amount of the composition of the spinel phase of a Ni-Zn ferrite. The oxides were mixed in the amounts given in Table VII, with the ratio of NiO:ZnO = 2:3. The composition of the ferrite prepared from sample 2 could vary between the limits $Ni_{.48}Zn_{.52}Fe_2O_4$ and $Ni_{.28}Zn_{.72}Fe_2O_4$, depending on whether or not the spinel phase preferentially selected Ni or Zn and rejected the other. With no preferential selection, the composition of the ferrite would be the same as sample 1,

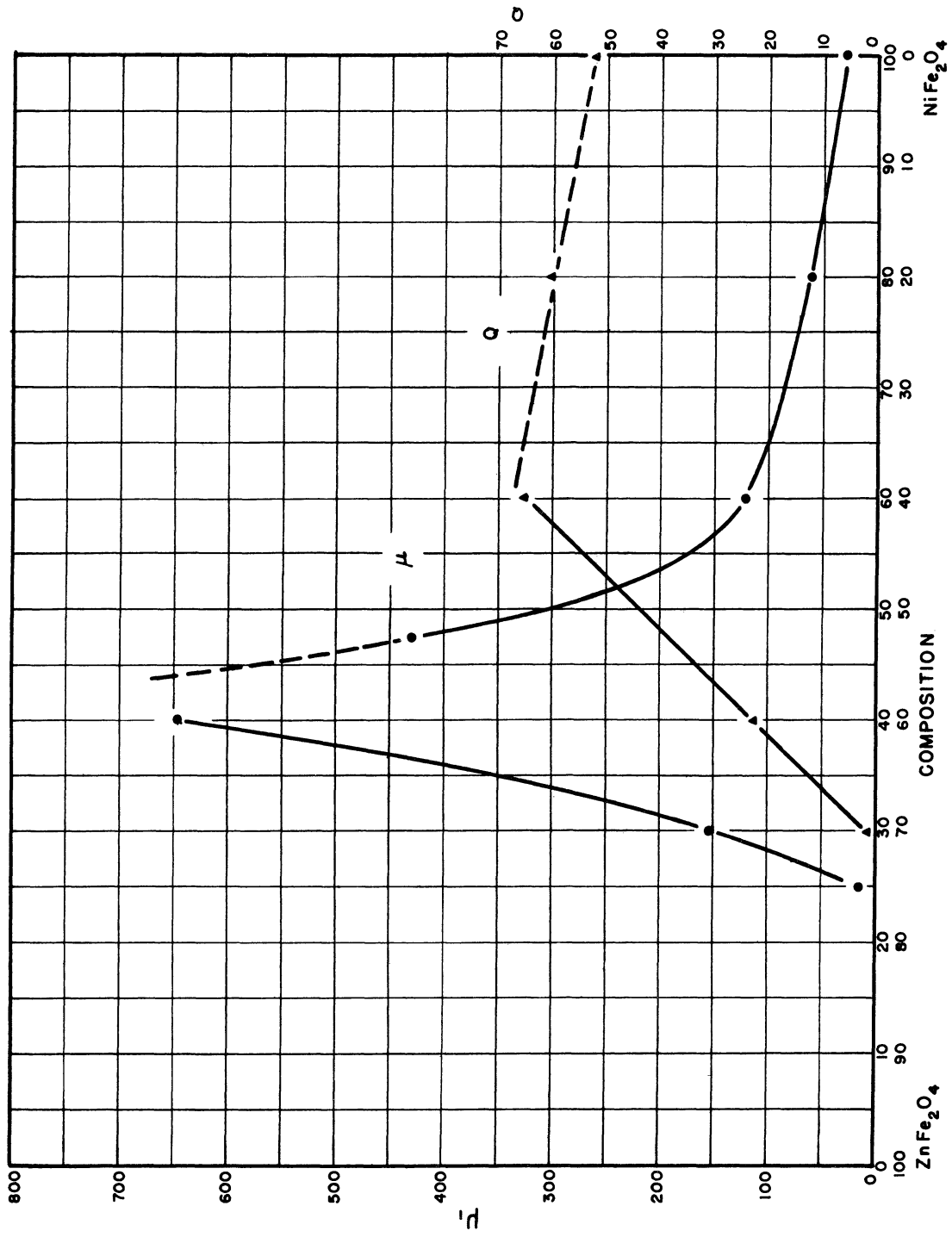

Fig. 9. μ_1 and Q vs. composition for Ni-Zn ferrites.

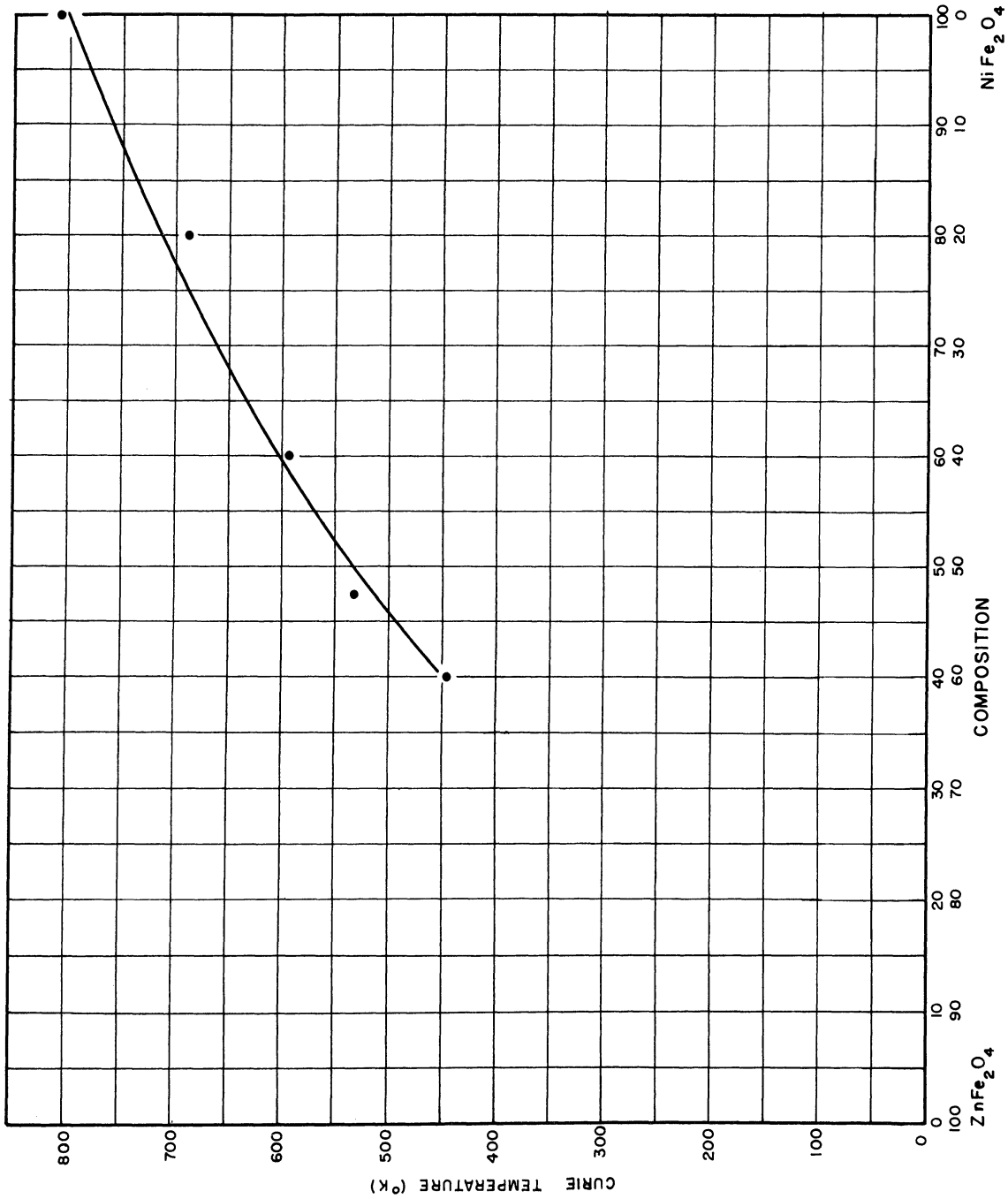

Fig. 10. Curie temperature vs. composition for Ni-Zn ferrites.

i.e., $Ni_{.4}Zn_{.6}Fe_2O_4$, with the second phase containing NiO and ZnO in the same proportion as the spinel phase.

Both samples were heated at 1200°C for 4 hours. The Curie temperatures, permeabilities and Q factors are given in Table VII. The Curie temperatures are identical within experimental error, indicating that the composition of the ferrite phase is the same in both samples. The permeabilities and Q's are considerably different for the two samples. The addition of the second phase decreases the permeability considerably. This is to be expected, at least for the portion of the permeability due to domain wall movement.

TABLE VII

THE EFFECT OF EXCESS (Ni,Zn)O ON THE MAGNETIC PROPERTIES OF A Ni-Zn FERRITE

Sample No.	Mole NiO	Mole ZnO	Mole Fe_2O_3	μ	Q	Curie Temp., °C
1	.20	.30	.50	647	22.5	272
2	.24	.36	.50	248	45.0	277

2.3.3 The System $Ni_{.474}Zn_{.526}Fe_2O_4$-$Fe_3O_4$.—The initial permeabilities and Q's of five compositions fired at 1210°C for varying lengths of time and air-quenched are shown in Figs. 11 and 12. It can be observed that μ_1 decreases and Q increases with increasing Fe_2O_3 content in the initial composition. This appears consistently throughout the investigation. Figures 13 and 14 are surfaces showing the dependence of Q on firing time and frequency for a stoichiometric and nonstoichiometric Ni-Zn ferrite. The samples were cooled by quenching in water.

The surfaces for the two materials are considerably different. This difference is due mainly to the fact that, with $Ni_{.474}Zn_{.526}Fe_2O_4$, the maximum Q occurs at about the same firing time at all frequencies, while

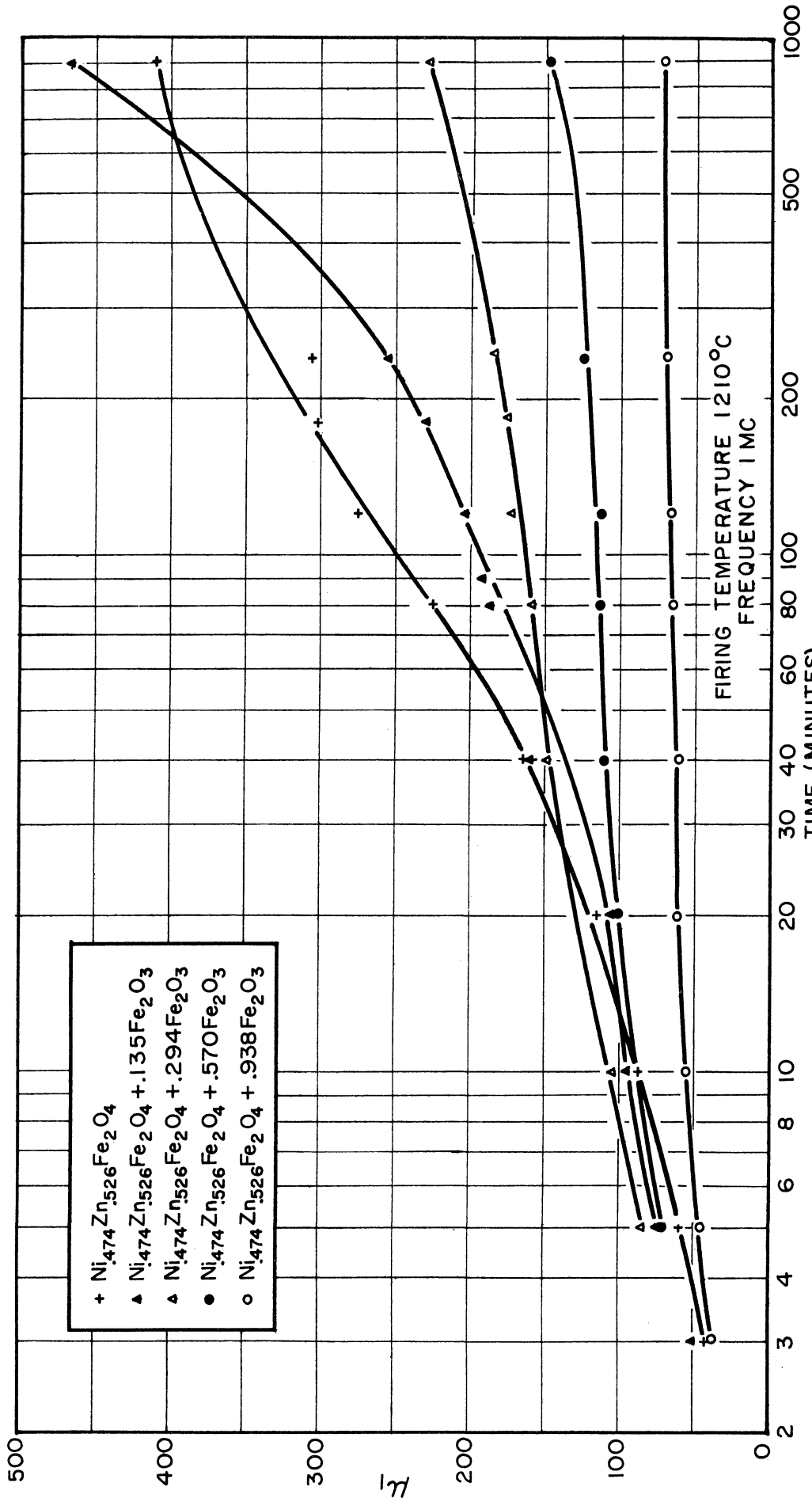

Fig. 11. μ_i vs. firing time for five compositions.

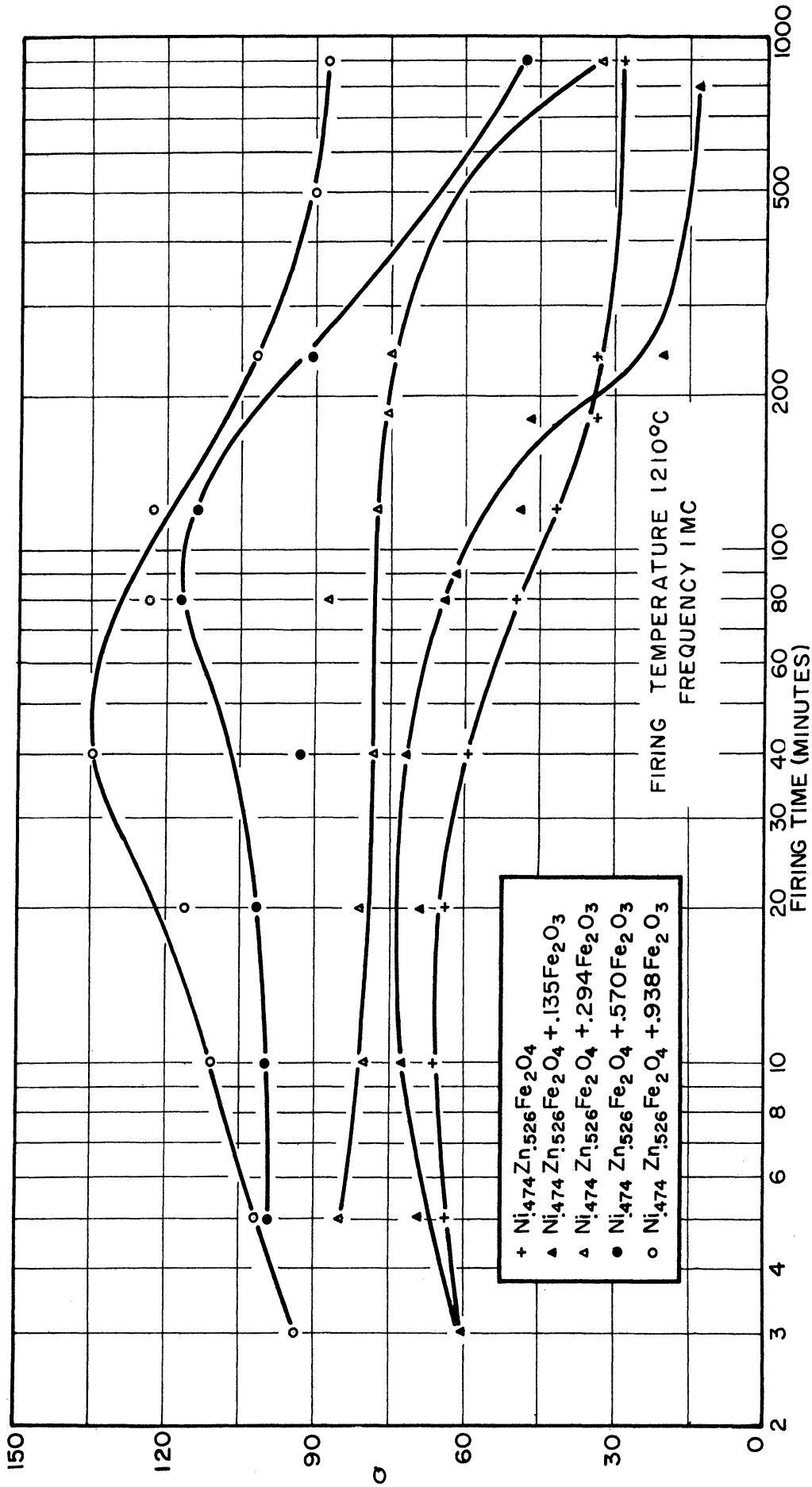

Fig. 12. Q vs. firing time for five compositions.

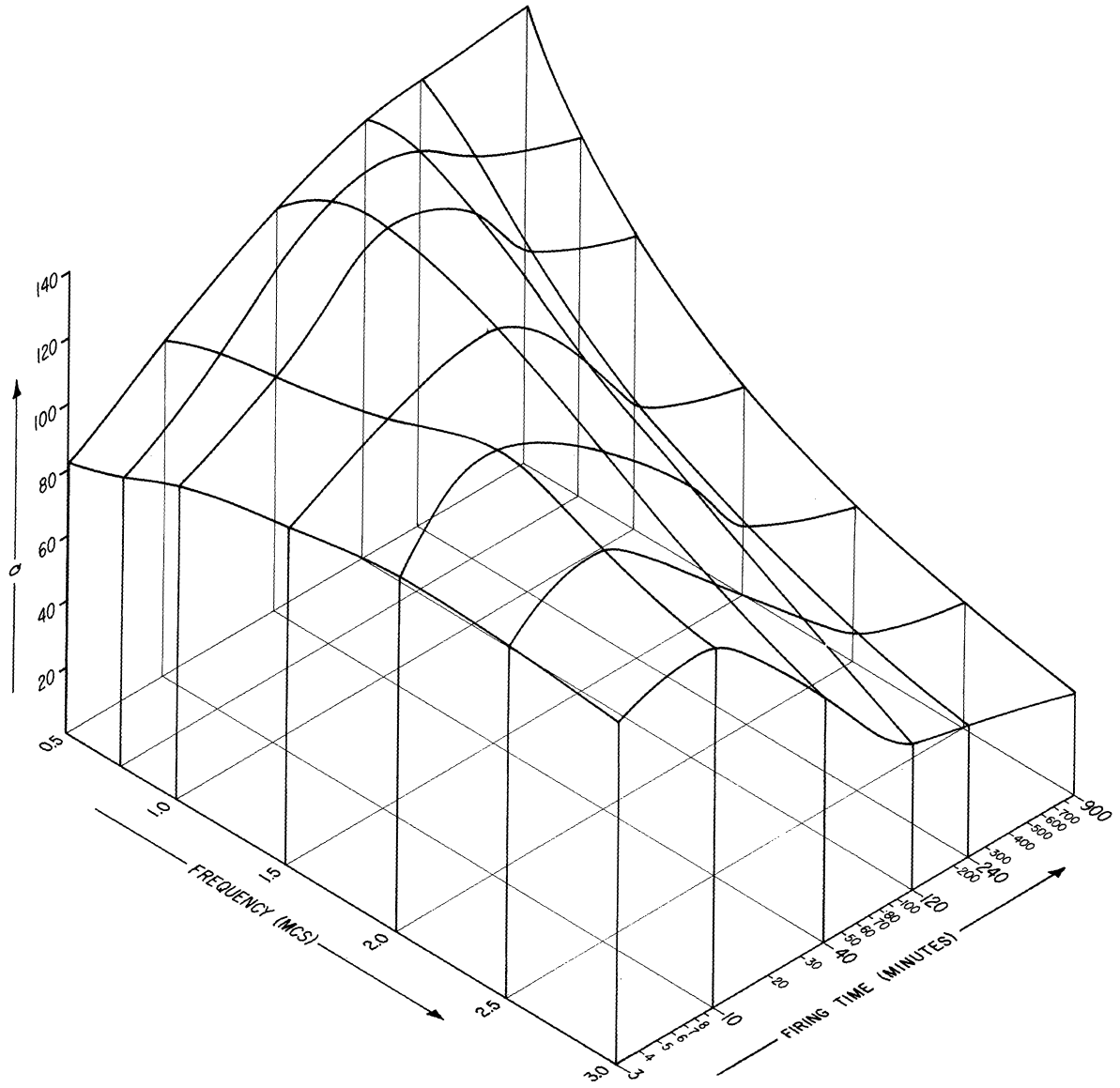

Fig. 13. Frequency-Q-firing time surface, $Ni_{.474}Zn_{.526}Fe_2O_4 + .938Fe_2O_3$.

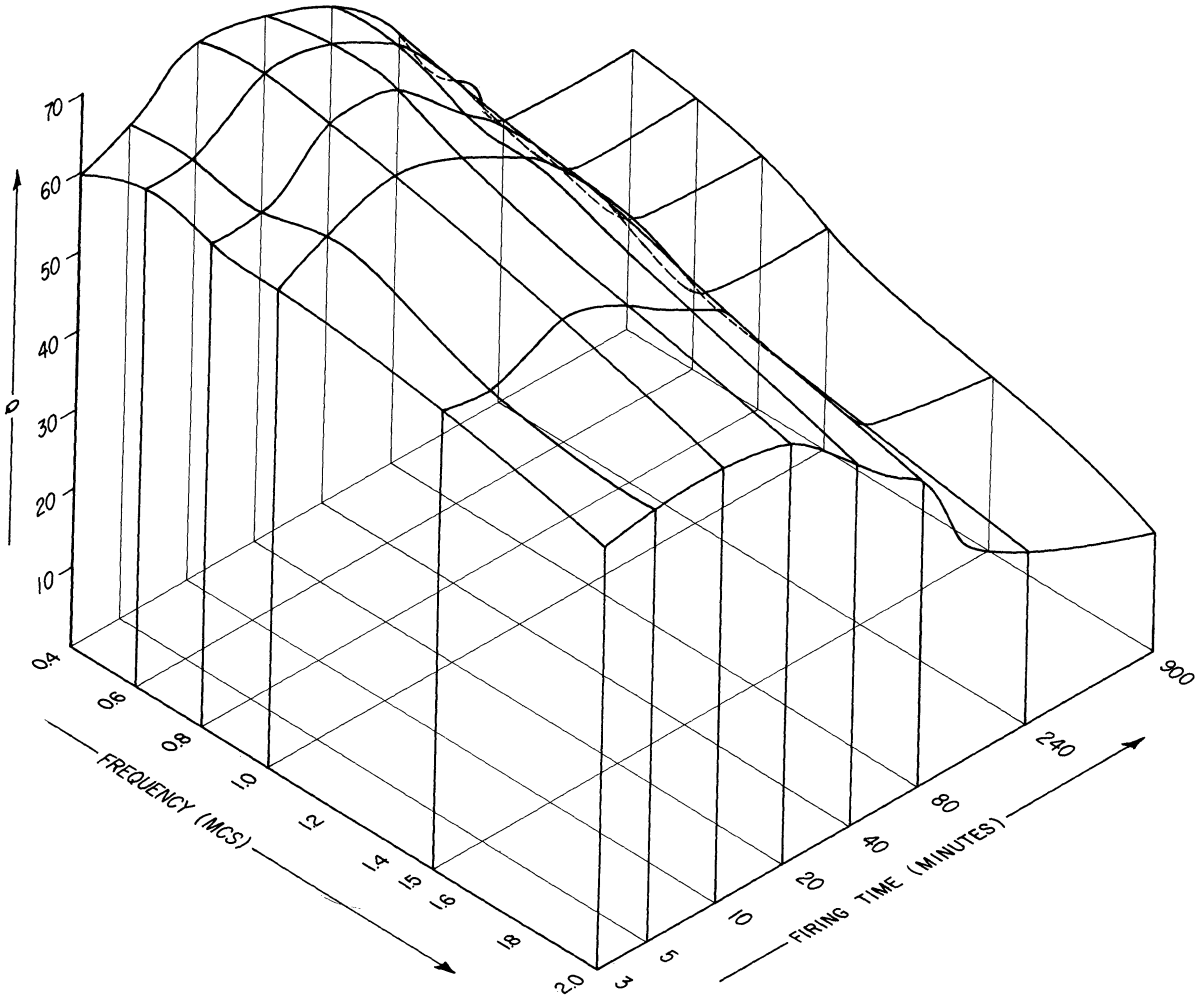

Fig. 14. Frequency-Q-firing time surface, $Ni_{.474}Zn_{.526}Fe_2O_4$.

for the material containing excess Fe_2O_3, the maximum Q moves to longer firing times as the frequency is lowered.

Figure 15 is a plot of Q at 2 mc vs. percent ferrous iron obtained from cores fired at several temperatures and air-cooled. It can be observed that the value of Q increases to a maximum at about 3.5% ferrous iron and then decreases. It appears that the maximum Q is determined by the concentration of ferrous iron.

Figure 16 is a plot of the ferrous iron content and Q at 2 mc as a function of reaction temperature for water-quenched cores. If the Q depends only upon the ferrous iron content, it would be expected that the drop in Q would be at the same ferrous iron content for the different heat treatments. This is not entirely true, although the Q starts to decrease for the water-quenched cores at a lower reaction temperature than it does for the air-quenched cores. It would be expected that the composition of the air-quenched cores would not be uniform, since oxidation would be greatest at the surface. This might account for the observed result.

The magnetic properties of the cores can be changed considerably by annealing. Data for two cores fired at 1210°C for 40 minutes and annealed at 800°C for 1 hour are given in Table VIII. The stoichiometric core did not change, while there was a considerable change in the nonstoichiometric core. The nonstoichiometric core contained 3.1% ferrous iron before annealing and .18% after annealing.

It was found that cores fired at higher temperatures were oxidized very little on annealing. If the core is dense, only a small amount of surface oxidation takes place. A frequency spectra of some cores before and after annealing is given in Fig. 17. It can be seen that μ_1 is changed very little on annealing, but Q is increased, and the maximum is shifted to a higher frequency. Again the permeability decreases as the amount of

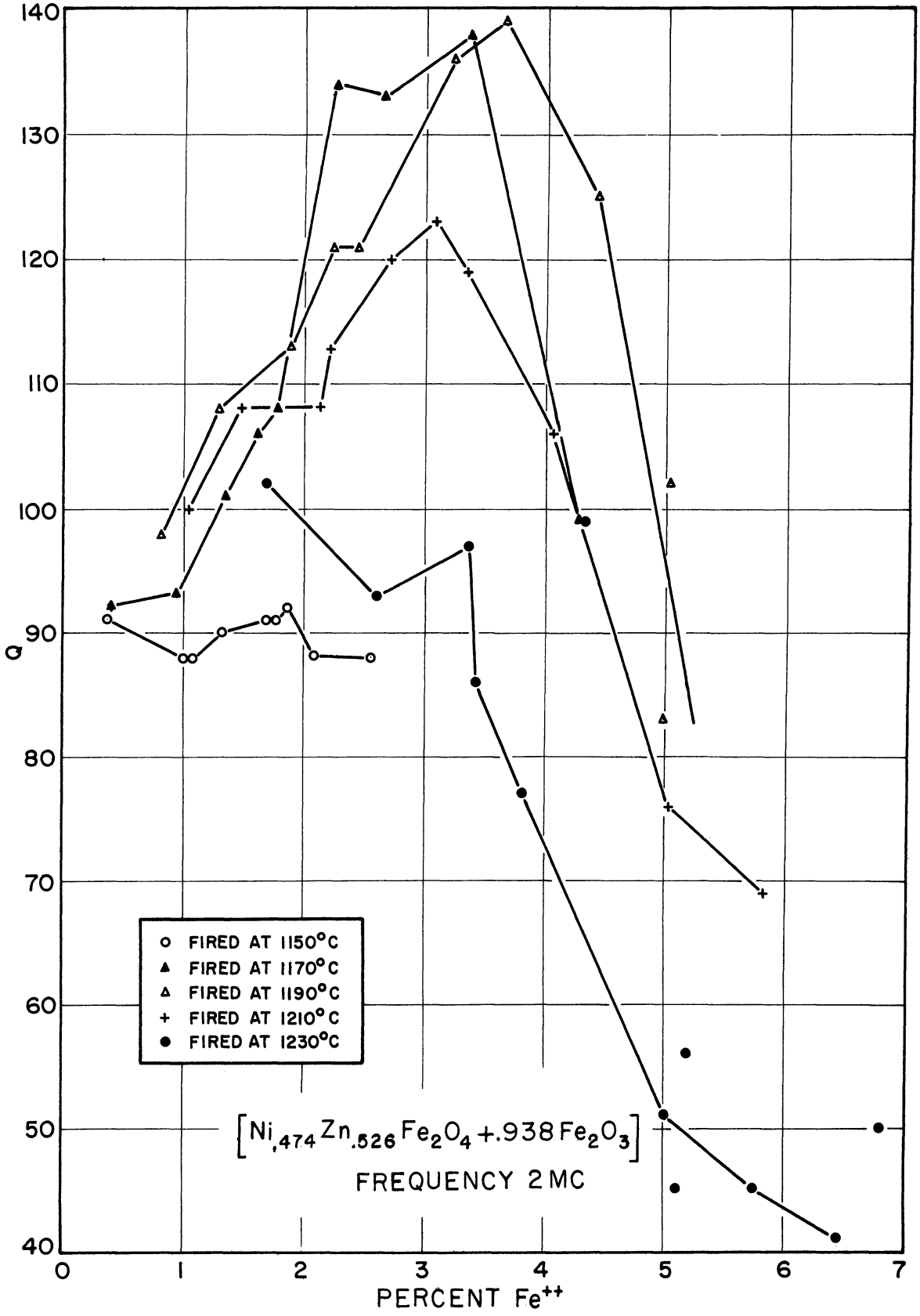

Fig. 15. Q vs. percent ferrous iron, air-quenched.

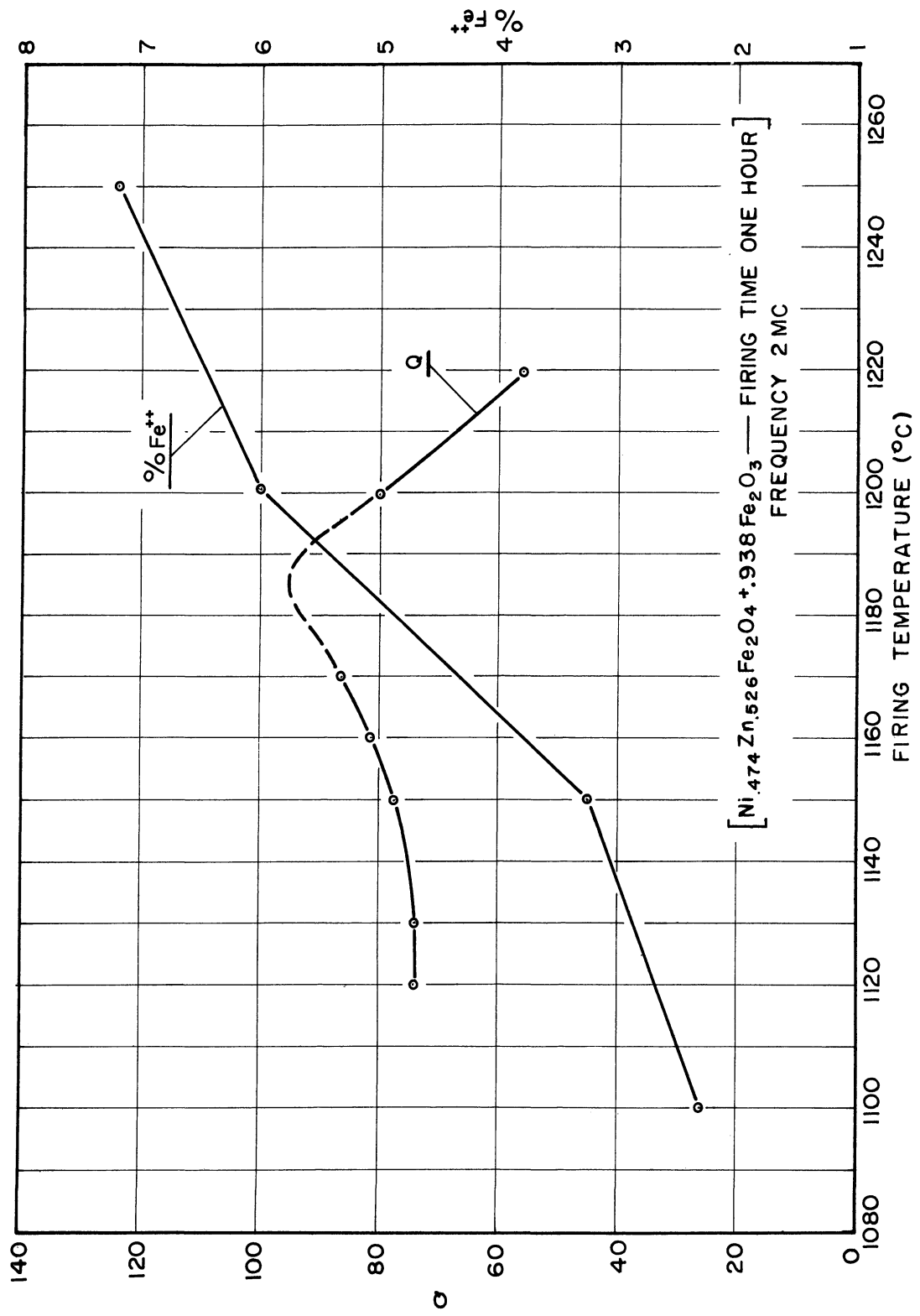

Fig. 16. Q and percent of ferrous iron vs. firing temperature for water-quenched cores.

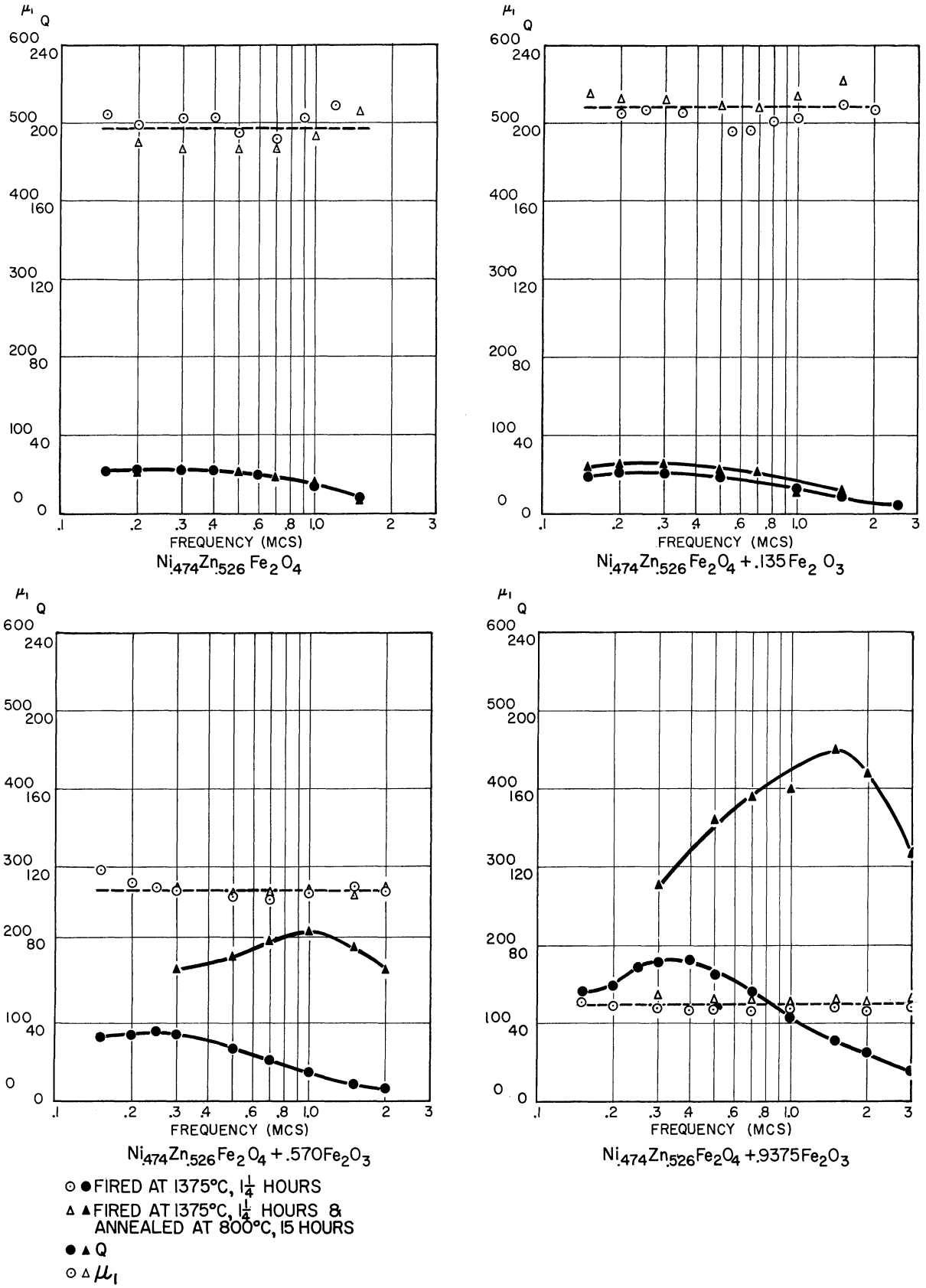

Fig. 17. Frequency spectra of μ_1 and Q as a function of total iron content.

TABLE VIII

EFFECT ON μ_1 AND Q OF ANNEALING UNDER OXIDIZING CONDITIONS

	Before Annealing		After Annealing	
	μ_1	Q	μ_1	Q
$Ni_{.474}Zn_{.526}Fe_2O_4$	145	47	150	45
$Ni_{.474}Zn_{.526}Fe_2O_4$ + .938 Fe_2O_3	60	135	8.7	47

Fe_2O_3 is increased. At the same time, the Q increases and the frequency at which the Q is at a maximum shifts to higher frequencies.

The exact cause for the above results is not known. If it were simply a matter of annealing out stresses, it would be expected to occur in the stoichiometric ferrite as well, which it does not. Possibly an orientation of the cations on different lattice sites is involved. The annealed material did not show a second phase in the polished sample.

The ferrous iron content of water-quenched samples rapidly attains a maximum value, as seen in Table III. The ferrous iron content of air-quenched samples increases with reaction time up to 900 minutes. This is because in the initial stages of the reaction the sample is relatively porous and is readily oxidized while cooling in air. In Table IX, the permeabilities and ferrous iron content of air-cooled samples are given. The permeability is plotted as a function of reaction time in Fig. 18.

The permeability of the samples appears to be independent of the ferrous iron content. It can be seen in Fig. 18 that the permeability reaches a constant value fairly rapidly, while the ferrous iron content continues to increase. (See Table IX.) Again, while the ferrous iron content depends a great deal on the method of quenching, the permeabilities of air-quenched and water-quenched samples are not greatly different. This is seen from

TABLE IX

DATA ON $Ni_{.474}Zn_{.526}Fe_2O_4$ + .938 Fe_2O_3; AIR-COOLED

Temperature 1150°C

Core No.	Time (min)	μ_1 at 2 mc	Q at 2 mc	Wt.% Fe^{++}
A 439-1	5	15	91	.36
A 440-1	10	24	88	1.00
A 441-1	15	25	88	1.10
A 442-1	20	26	90	1.32
A 443-1	40	28	91	1.69
A 444-1	80	32	92	1.86
A 445-1	120	32	91	1.75
A 446-1	240	33	89	2.09
A 447-1	480	36	88	2.55
A 448-1	900	38	87	----

Temperature 1170°C

Core No.	Time (min)	μ_1 at 2 mc	Q at 2 mc	Wt.% Fe^{++}
A 392-1	3	23	92	.4
A 393-1	5	31	93	.94
A 394-1	10	36	101	1.35
A 396-1	20	40	106	1.62
A 397-1	40	41	108	1.78
A 398-1	80	45	134	2.27
A 399-1	120	47	133	2.67
A 400-1	240	47	138	3.38
A 402-1	900	48	99	4.28

Temperature 1190°C

Core No.	Time (min)	μ_1 at 2 mc	Q at 2 mc	Wt.% Fe^{++}
A 375-1	3	38	98	.82
A 376-1	5	37	108	1.30
A 377-2	10	43	113	1.88
A 378-1	15	45	121	2.24
A 379-1	20	48	121	2.43
A 380-1	40	--	---	2.60
A 381-1	80	51	136	3.23
A 382-1	120	52	139	3.65
A 385-1	240	52	125	4.43
A 390-1	630	53	102	5.04
A 389-1	900	53	83	4.97

Temperature 1210°C

Core No.	Time (min)	μ_1 at 2 mc	Q at 2 mc	Wt.% Fe^{++}
A 404-1	3	31	100	1.05
A 405-1	5	42	108	1.48
A 406-1	7	44	108	2.15
A 407-2	10	47	113	2.21
A 408-2	15	50	120	2.72
A 410-1	30	53	119	3.36
A 411-1	40	54	123	3.10
A 412-1	80	55	106	4.06
A 413-1	120	54	120	----
A 415-1	240	56	76	5.02
A 417-1	900	59	69	5.84

Temperature 1230°C

Core No.	Time (min)	μ_1 at 2 mc	Q at 2 mc	Wt.% Fe^{++}
A 418-2	3	40	102	1.68
A 419-1	4	47	98	----
A 420-2	5	56	93	2.6
A 421-1	7	63	97	3.36
A 422-2	10	71	86	3.44
A 433-1	12	71	77	3.83
A 423-1	15	74	99	4.33
A 424-1	20	83	45	5.10
A 426-1	30	83	51	5.01
A 427-1	40	85	56	5.20
A 428-1	60	86	45	5.76
A 429-1	80	93	32	6.06
A 430	120	93	41	6.44
A 432	900	75	50	6.79

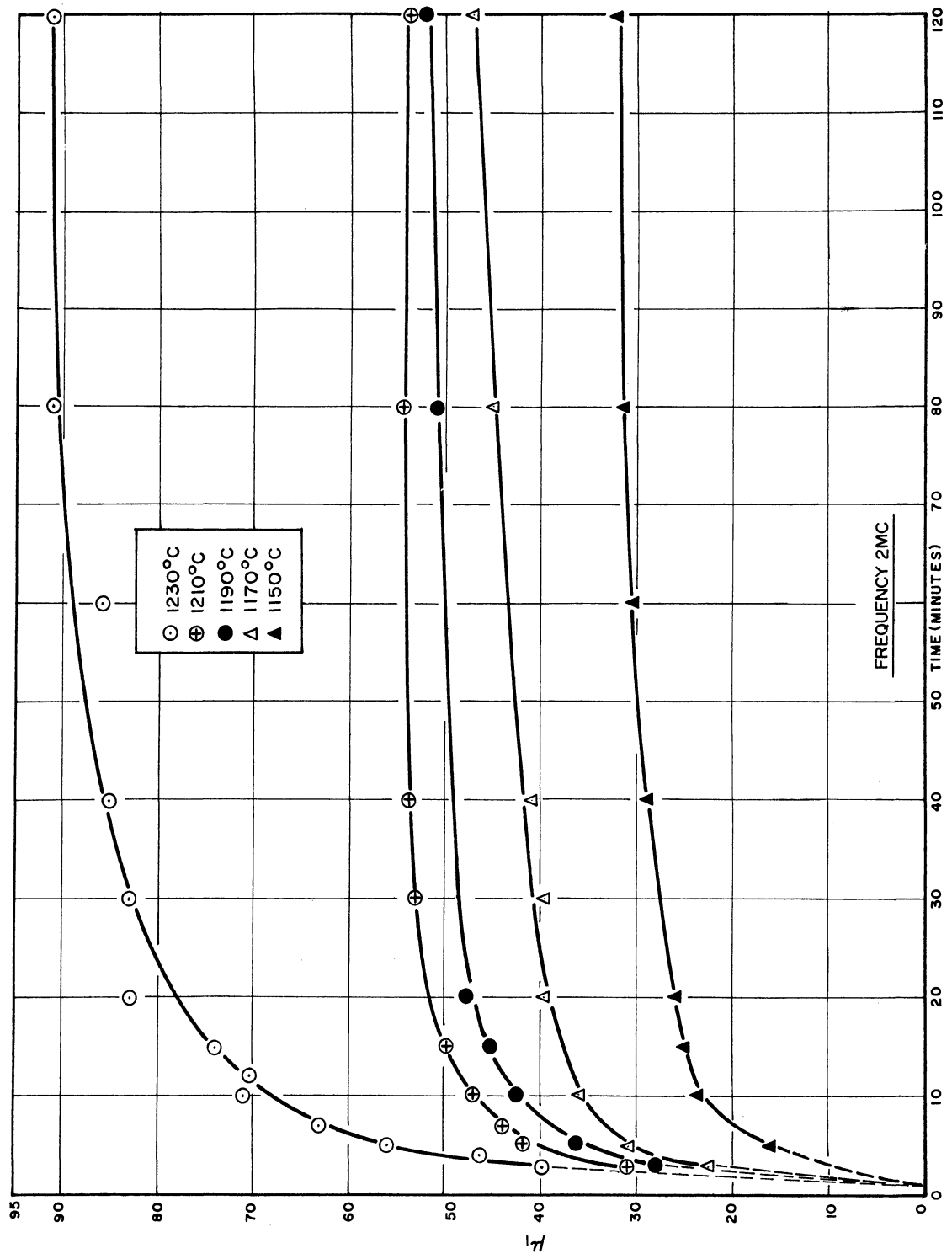

Fig. 18. μ1 vs. firing time for $Ni_{.474}Zn_{.526}Fe_2O_4$ + $.938Fe_2O_3$.

Table X, where the permeabilities of air-quenched and water-quenched cores are given at a number of frequencies. While the permeabilities of the air-quenched cores are somewhat greater for the longer reaction times, for the shorter reaction times there is not much difference.

TABLE X

PERMEABILITY DATA FOR WATER-QUENCHED AND AIR-QUENCHED CORES

(Firing Temperature 1210°C)

Freq. (mc)	Firing Time (min) (Water Quench) Comp. 5								
	3	5	7	10	40	80	120	240	900
.9	32.2	39.9	44.0	49.5	55.9	56.5	57.4	57.5	58.5
2.0	33.8	42.0	46.4	52.3	59.0	59.9	60.3	60.7	62.35
4.0	34.2	42.5	46.8	54.7	59.8	60.8	61.2	62.2	63.44
7.0	35.1	43.4	47.6	53.9	61.7	62.8	62.8	63.4	65.7
12.0	33.8	41.8	46.7	53.4	60.5	62.8	61.8	63.0	64.8
18.0	36.9	46.4	51.7	58.9	67.3	69.9	70.3	72.4	74.4

Freq. (mc)	Firing Time (min) (Air Quench) Comp. 5								
	3	5	7	10	40	80	120	240	900
.9	32.97	32.5		51.9	62.1	63.1	63.6	67.7	67.0
2.0	34.6	45.8		53.6	65.9	67.0	67.6	71.6	71.0
4.0	34.7	45.8		53.9	66.6	67.6	68.6	72.4	72.5
7.0	35.0	46.2		54.7	67.8	69.0	69.9	74.0	75.6
12.0	34.4	45.5		53.9	67.8	70.4	71.0	75.5	80.0
18.0	36.4	48.3		58.3	74.	77.9	81.5	87.3	93.6

It has been observed throughout that, as the Fe_2O_3 content is increased, the permeability is decreased. It was thought that the introduction of divalent iron into the lattice would effectively decrease the concentration of zinc and raise the Curie temperature. This could account for the lower permeability. Three compositions with varying zinc content were prepared and the magnetic properties and Curie temperature measured. Figure 19 shows the results of this experiment. While the Curie temperature increases with decreasing zinc content, the permeabilities are almost equal.

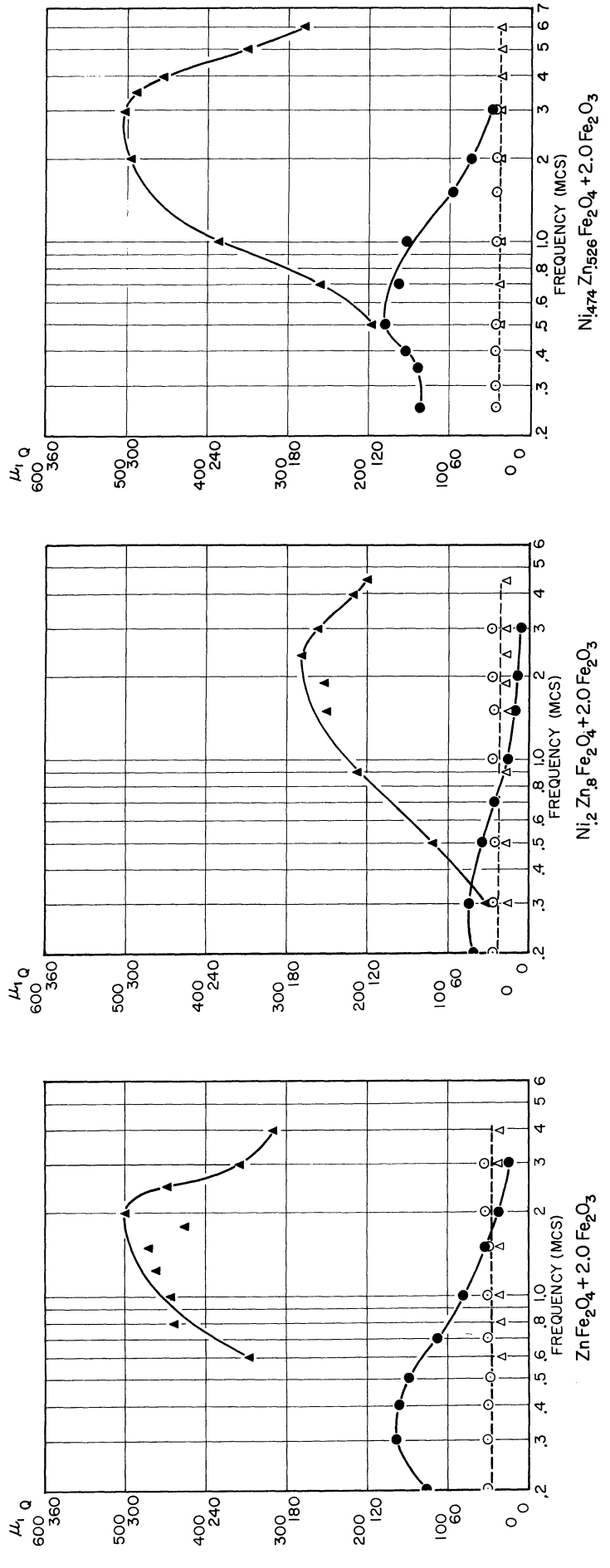

Fig. 19. Effect of Varying the Ni-Zn ratio on magnetic properties of a nonstoichiometric ferrite.

3. SOLID-STATE REACTIONS OCCURRING IN THE PREPARATIONS OF FERRITES

3.1 INTRODUCTORY REMARKS

The solid-state reactions which are involved in the formation of ferrites might be classified as the reaction leading to the ferrite formation and the reaction resulting in the densification of the ferrite product. In general, it might be said that the ferrite formation is complete before the densification becomes pronounced, although there is probably some overlap. Ferrite formation through reaction between two solid components is a true solid-state chemical reaction. The densification process, usually termed sintering, is also classed as a solid-state reaction, since, as in the above case, material transport through the process of diffusion is necessary for the reaction to progress. The driving force for the ferrite reaction is the chemical potential arising from the concentration gradient at the boundary surfaces. The driving force for the sintering process is the reduction of the surface free energy brought about by decreased surface area of the denser material.

The treatment of the kinetics of solid-solid reactions is complicated by the fact that most reactions of this type are subject to variations, depending upon the previous treatment to which the oxides have been subjected. It is known that lattice imperfections and dislocations aid in the diffusion process. In general, it has been found that oxides which have been prepared at the lowest temperatures are the most reactive, since heating destroys the lattice imperfections. Impurities which increase the number of lattice imperfections also accelerate solid-solid reactions.

The kinetics of the reaction between two solid particles is governed

by the reaction rate at the solid-solid interface and by the rate at which the reacting components are supplied at the interface by diffusion. In general, the boundary reaction is sufficiently rapid so that it can be neglected, and the rate determining process becomes the diffusion of the reacting components to the interface.

The reaction occurs at the points of contact of the two reacting particles, and as the reaction proceeds a layer of the product forms between the two particles. In order for the reaction to continue, one or both of the reacting components must diffuse through this product layer to react with the oxide on the other side. The effect of the product layer can be either to retard, to accelerate or not to alter the rate of reaction, depending on whether or not the rate-determining step for the reaction is the diffusion of reacting components through the product layer. Since this process is usually slower than the boundary reaction, it is often the rate-determining step. The rate of arrival of the diffusing component at the reacting interface is then inversely proportional to the thickness of the product layer through which it must diffuse. This fact is expressed in the following rate equation:

$$\frac{dy}{dt} = \frac{k}{y} ; \qquad y^2 = k't \tag{4}$$

where y is the thickness of the product layer, k is a constant and t is time. This equation, first proposed by Tammann,[23] has been verified for numerous solid-state reactions. In case the boundary reaction cannot be neglected, it has been shown that the rate equation is, to a first approximation[24]

$$\frac{dy}{dt} = \frac{k}{y+b} ; \qquad yb + y^2 = k't \ . \tag{5}$$

In the initial stages when y is small, the equation reduces to $y = (k'/b)t$.

When y becomes large the equation becomes $y^2 = k't$.

Equations (4) and (5) express the growth rate of the product layer as a function of time. In actual practice it is more convenient to measure the percent of the oxides which have reacted to form the product. Jander[25] obtained such an expression for the case where spherical particles of one component are surrounded by spherical particles of the other. The unreacted particle is assumed to have a radius R. The radius at any time t is then R-y, where y is still the thickness of the product layer. The volume of the unreacted sphere is $4/3\pi(R-y)^3$. The fraction of the sphere that has reacted is given by

$$\frac{4/3\pi R^3 - 4/3\,\pi\,(R-y)^3}{4/3\ \pi R^3} = \frac{x}{100} \quad , \tag{6}$$

where x is the percent of the sphere which has reacted. Solving for y, we obtain

$$y = (1 - \sqrt[3]{1 - x/100})R \quad . \tag{7}$$

This value of y can be substituted into Eq. (4) to obtain

$$(1 - \sqrt[3]{1 - x/100})^2 = k''t \quad . \tag{8}$$

We can obtain k" from a plot of $(1 - \sqrt[3]{1 - x/100})^2$ vs. t. The activation energy can then be obtained from a plot of log k" vs. 1/T.

Very little is known about the actual mechanism whereby the spinel structure is formed. Wagner[26] proposed that the spinel reaction can be considered to consist of the diffusion of Me^{+2} and Fe^{+3} in opposite directions through the product layer and the following boundary reactions:

At the MeO-$MeFe_2O_4$ boundary: $4\ MeO + 2\ Fe^{+3} = MeFe_2O_4 + 3\ Me^{+2}$

At the Fe_2O_3-$MeFe_2O_4$ boundary: $4\ Fe_2O_3 + 3\ Me^{+2} = 3\ MeFe_2O_4 + 2\ Fe^{+3}$

Probably the most complete investigation of a spinel reaction was that by

Huttig[27] on the reaction between ZnO and Fe_2O_3. By means of chemical and physical properties, the changes in a mixture of ZnO and Fe_2O_3 were followed from the time of mixing to the formation of the spinel. Finch and Sinha[28,29] found that outgrowths on αFe_2O_3 particles undergo a transformation to γFe_2O_3 at 700°C which persists as high as 900°C. Their conclusion was that this step is necessary for the formation of ferrites by a solid-state reaction. This mechanism would suppose that the spinel structure forms first, followed by diffusion of the divalent cation into the structure.

Using X-ray methods, Kedesdy and Katz[30] found that the spinel structure starts to form at 600°C for $ZnFe_2O_4$ and 700°C for $NiFe_2O_4$, with temperatures for ferrite formation of mixed NiO and ZnO ferrites intermediate between these two temperatures. Guillissen and Rysselberghe[31] found by chemical analyses of unreacted Zn in a mixture of ZnO and Fe_2O_3 that reaction to form the ferrite starts slightly below 600°C. In this case the extent of reaction reached a constant value after several hours, so that to further this reaction the temperature had to be increased. Hopkins[32] found that the reaction rate was influenced by the temperature of preparation of the Fe_2O_3. He found that Fe_2O_3 was transformed into a less reactive form at 675°C. Activation energies for the formation of $ZnFe_2O_4$ from the two forms of Fe_2O_3 were found to be 110 Kcal/mole for the high-temperature form of Fe_2O_3, and 57 Kcal/mole for the low-temperature form.

Okamura and Simoizaka[33] investigated the rate of formation of $NiFe_2O_4$ with respect to the method of mixing. They concluded that, with mechanical mixing, diffusion through the product layer was the rate-controlling step, while with co-precipitated material this was not so. The activation energy of mechanically mixed oxides was found to be 44 Kcal/mole. For the co-precipitated oxides it was found to be 25 Kcal/mole. They found no cor-

relation between the appearance of the spinel structure in the X-ray diagrams and the magnetic intensity of the sample, from which they concluded that there were both a nonmagnetic and a magnetic spinel structure. Yost[34] stated that the Wagner mechanism can be used to explain the formation of spinels and silicates. Linder,[35] using radio tracers, found that the Wagner theory explained the reaction rate of zinc ferrite formation. This type of mechanism also explained the rate of formation of $NiFe_2O_4$ in the mechanically mixed material prepared by Okamura and Simoizaka.[33]

Nagaura, Kato, and Niboshi[36] investigated the reaction between ZnO and Cr_2O_3 and found that the reaction kinetics conformed to Jander's equation. The temperature where reaction starts was found by differential thermal analysis and X-ray analysis to be 590°C, while the activation energy was 21 Kcal/mole. Kushima and Amanuma[37] studied the formation reaction of the ferrites of Cu, Ni, Zn, and Co. The temperature of formation was 700° for $CoFe_2O_4$, 650° for $NiFe_2O_4$, and 720° for $CuFe_2O_4$.

Relatively little work has been done to evaluate the influence of the atmosphere on the reaction mechanism. The role played by the atmosphere in a solid-gas reaction is far better understood than is the role played by the atmosphere in a solid-solid reaction. The mechanisms through which the surrounding gas can alter the reaction are probably changes in the defect concentrations of the reacting oxides and product layer and changes in binding forces of the atoms at the solid-gas interface. The first mechanism would increase the rate of diffusion to the reacting boundary, while the second would increase the rate of reaction at the boundary.

Hedvall[38] has shown that when Fe_2O_3 is sintered in N_2 and O_2, both A and Q are altered in the equation $k = A \exp - Q/RT$.

Okamura and Simoizaka[33] investigated the reaction of NiO and Fe_2O_3 as

a function of the gas pressure between 800°C and 1050°C. It was found that there was little difference at 800°C. At 900°C and above, the limit of the value of σ_s as a function of heating time increased with decreasing pressure.

Forestier[39] investigated the influence of various gases on the reaction between NiO and Fe_2O_3 at temperatures of 700°C and below, and concluded that at constant temperature and pressure the speed of the reaction is an increasing function of the temperature of liquefaction of the gas. Forestier also found that the speed of the reaction is approximately a linear function of the logarithm of the pressure, and that the reaction goes toward zero as the pressure goes toward zero.

In this section, results of some studies of reactions involved in the preparation of ferrites have been discussed. The mechanism of the reactions between NiO and Fe_2O_3 and between ZnO and Fe_2O_3 has been investigated by microscopic examination of the reacting particles. The influence of the atmosphere on the rate of reaction between NiO and Fe_2O_3 and between Li_2CO_3 and Fe_2O_3; the influence of the green density on the final density of sintered ferrites; and the stages in the oxidation of several magnetite-ferrite solid solutions have all been investigated.

3.2 MICROSCOPIC STUDY OF THE REACTION BETWEEN NiO AND Fe_2O_3

Normally, ferrites are prepared from oxide particles which are approximately .5 micron or less in size. When particles of this size are used, it is impossible to observe the course of the reaction between the oxides with a light microscope. To obtain large particles for this study, samples of NiO, ZnO, and Fe_2O_3 were sintered separately and crushed to the desired size. Compositions corresponding to 50 mole % NiO - 50 mole % Fe_2O_3 and 50 mole % ZnO - 50 mole % Fe_2O_3 were mixed without further grinding and

caused to react at several temperatures for various lengths of time. The samples were then impregnated with a solution of bakelite thinned with acetone. Once the bakelite was set, it was possible to polish the samples without pulling out the particles in the process.

The results of the study of the composition 50 mole % NiO - 50 mole % Fe_2O_3 are summarized as shown in Figs. 20, 21, and 22. These photomicrographs are not of the same particles in each case, but are typical of the particles in the different stages of reaction. The NiO particles consist of aggregates of small crystals. These crystals grow as the reaction progresses. The Fe_2O_3 diffuses into the NiO particles and appears to form a NiO-Fe_2O_3 solid solution. In the last photomicrograph of NiO, a precipitate is present. It is concluded that the precipitate is $NiFe_2O_4$, which has formed when the solubility of Fe_2O_3 in NiO is exceeded. A layer of $NiFe_2O_4$ forms around the outside of the Fe_2O_3 particles, as the NiO diffuses into them. As the reaction progresses, this layer increases in size until it includes the entire particle.

The photomicrographs in Figs. 21 and 22 were taken in polarized light with crossed nicols. The progress of diffusion of the Fe_2O_3 into the NiO can be followed by the red coloration it imparts to the NiO. The extent of diffusion of the NiO into the Fe_2O_3 particles can also be distinguished by the change in shading of the Fe_2O_3 particles at the surface in contact with the NiO. This can be observed especially in photomicrographs 2 and 3 of Figs. 21 and 22. While it is not possible to comment on the concentration of the diffusing component in these diffusion layers, it appears that the distances which the oxides have interpenetrated one another are about equal.

An identical study of the ZnO-Fe_2O_3 composition showed that the spinel reaction occurs entirely on the Fe_2O_3 particles. No evidence of diffusion

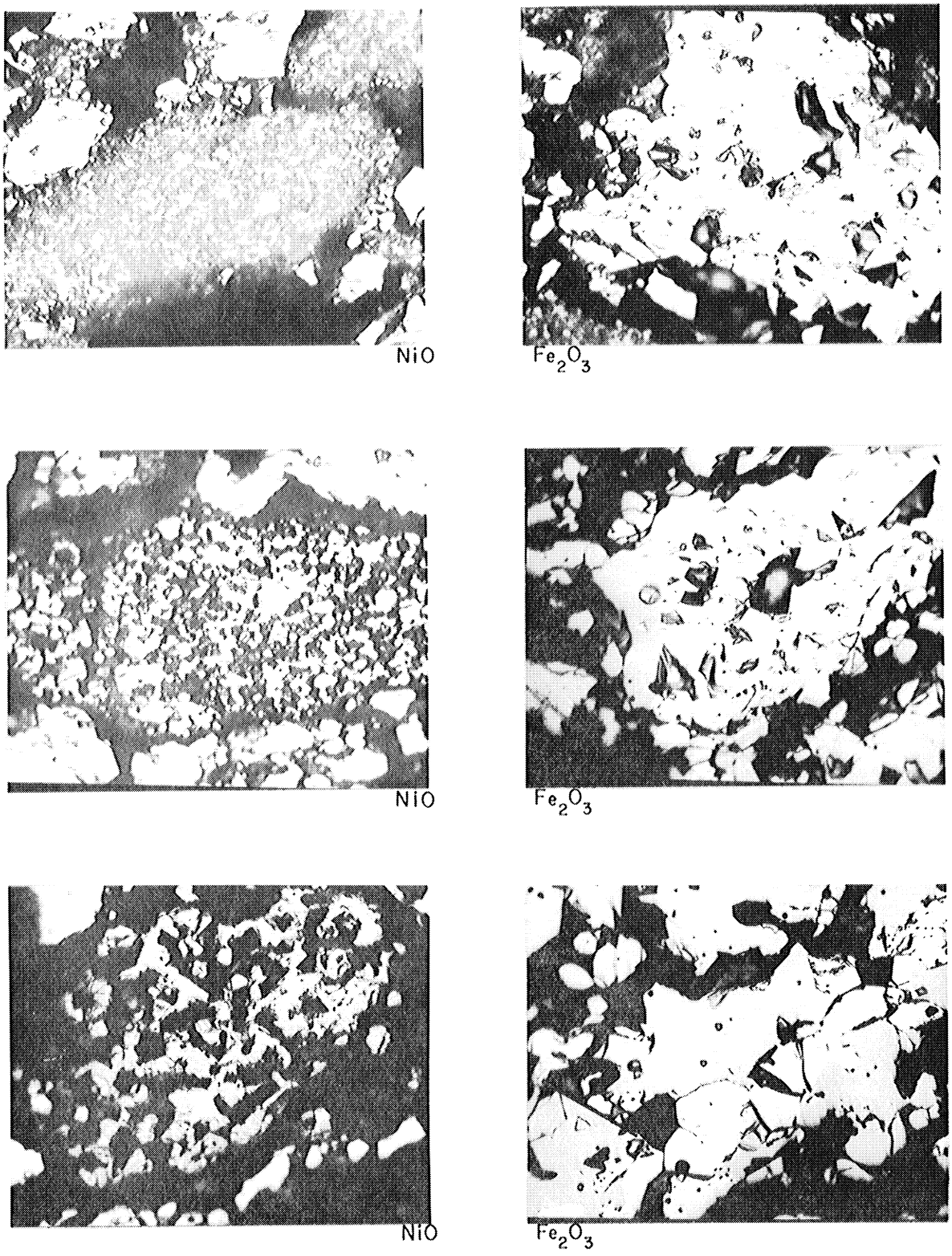

Fig. 20. NiO and Fe_2O_3 particles during different stages of reaction (X600).

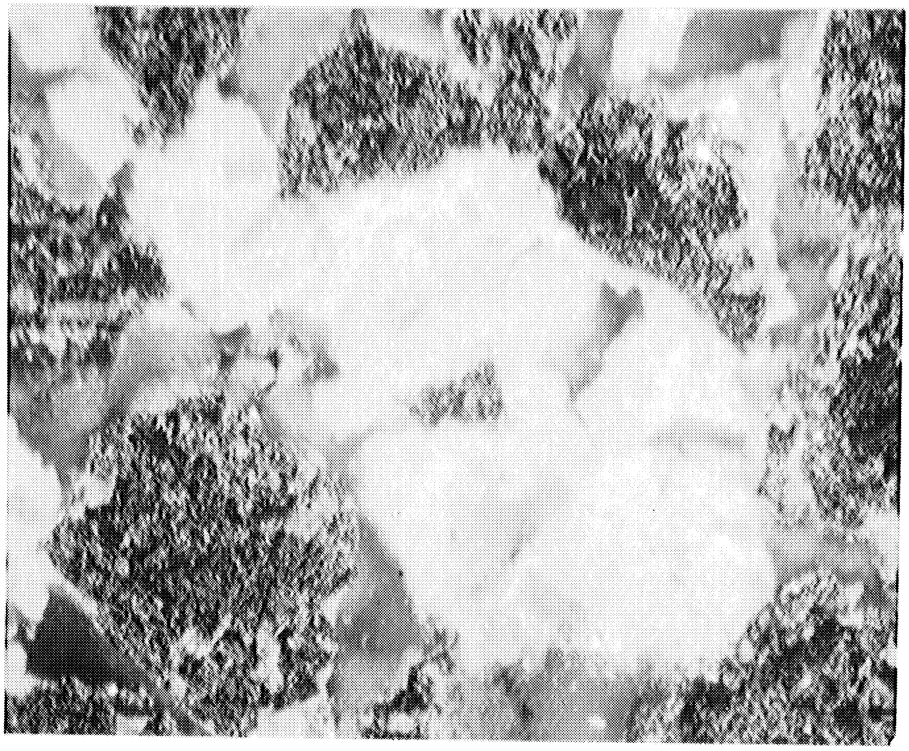

Stage 1

Stage 2

Fig. 21. NiO and Fe_2O_3 particles during different stages of reaction; polarized light with crossed nicols (X500).

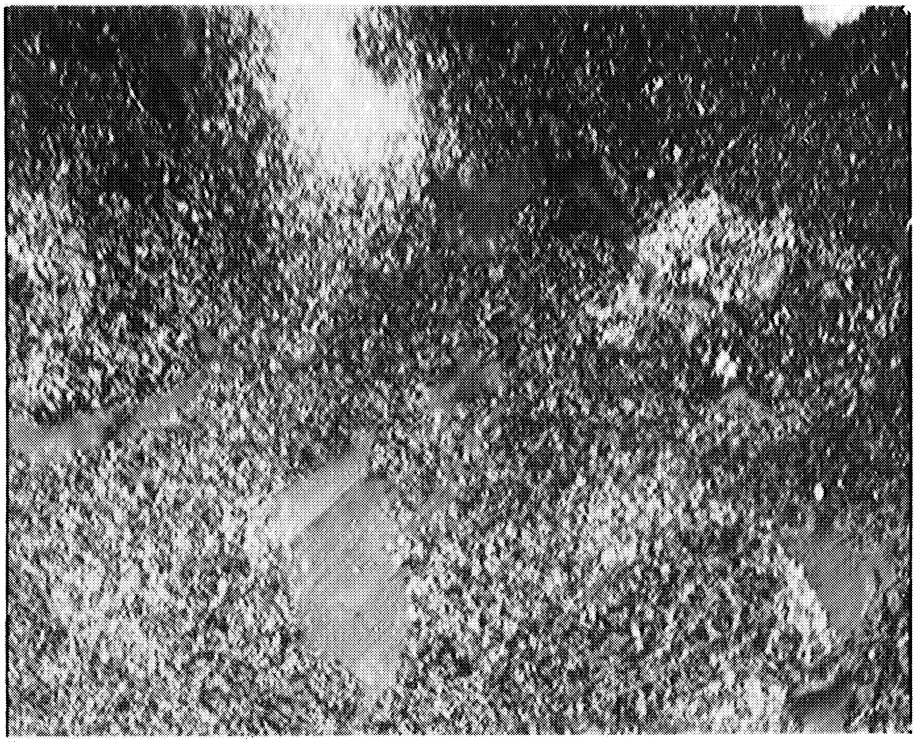

Stage 3

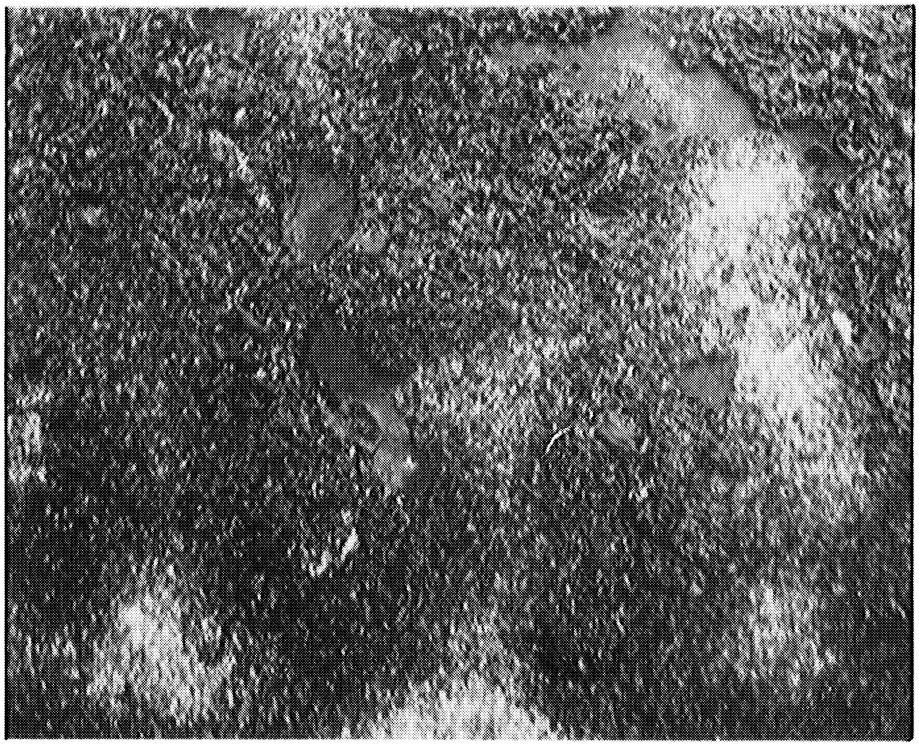

Stage 4

Fig. 22. NiO and Fe_2O_3 particles during different stages of reaction; polarized light with cross nicols (X500).

of Fe_2O_3 into the ZnO, or of ferrite formation on the surface of the ZnO particles, was detected.

3.3 INFLUENCE OF THE ATMOSPHERE ON THE FORMATION OF $NiFe_2O_4$ AND $LiFe_5O_8$

3.3.1 Preparation and Measurement of Samples.—The kinetics of the reaction between NiO and Fe_2O_3 and between Li_2CO_3 and Fe_2O_3, to form $NiFe_2O_4$ and $LiFe_5O_8$, respectively, have been investigated in air, oxygen, and nitrogen atmospheres. The extent of reaction at any time was determined by measuring the saturation moment. Since the saturation moment per gram is proportional to the amount of ferrimagnetic product formed during the reaction, the percent completion of the reaction can be obtained by dividing the moment per gram of the sample by the moment per gram of a completely reacted sample.

The total magnetic moment that a ferrimagnetic sample develops in a magnetic field, H, is given by $\sigma_s \cdot M$, where σ_s is the magnetic moment per unit mass and M is the mass of the sample. If the field is uniform over the sample, and if the orienting effect due to the geometry of the sample is small, there will be no displacement of the sample. If, however, the sample is placed in a nonhomogeneous field with a gradient $\partial H/\partial X$ in the direction of X, there will be a force exerted, given by:

$$F = \sigma_s M \frac{\partial H}{\partial X} .$$

The Faraday method for the measurement of the magnetic moment makes use of this principle. A sample of known mass is located in a nonhomogeneous field of known $\partial H/\partial X$ and the force exerted on the sample is measured. Knowing the force, mass, and field gradient, σ_s can be calculated.

The saturation magnetic moment was measured with the equipment shown in Fig. 23. This is generally known as a Faraday balance. The samples

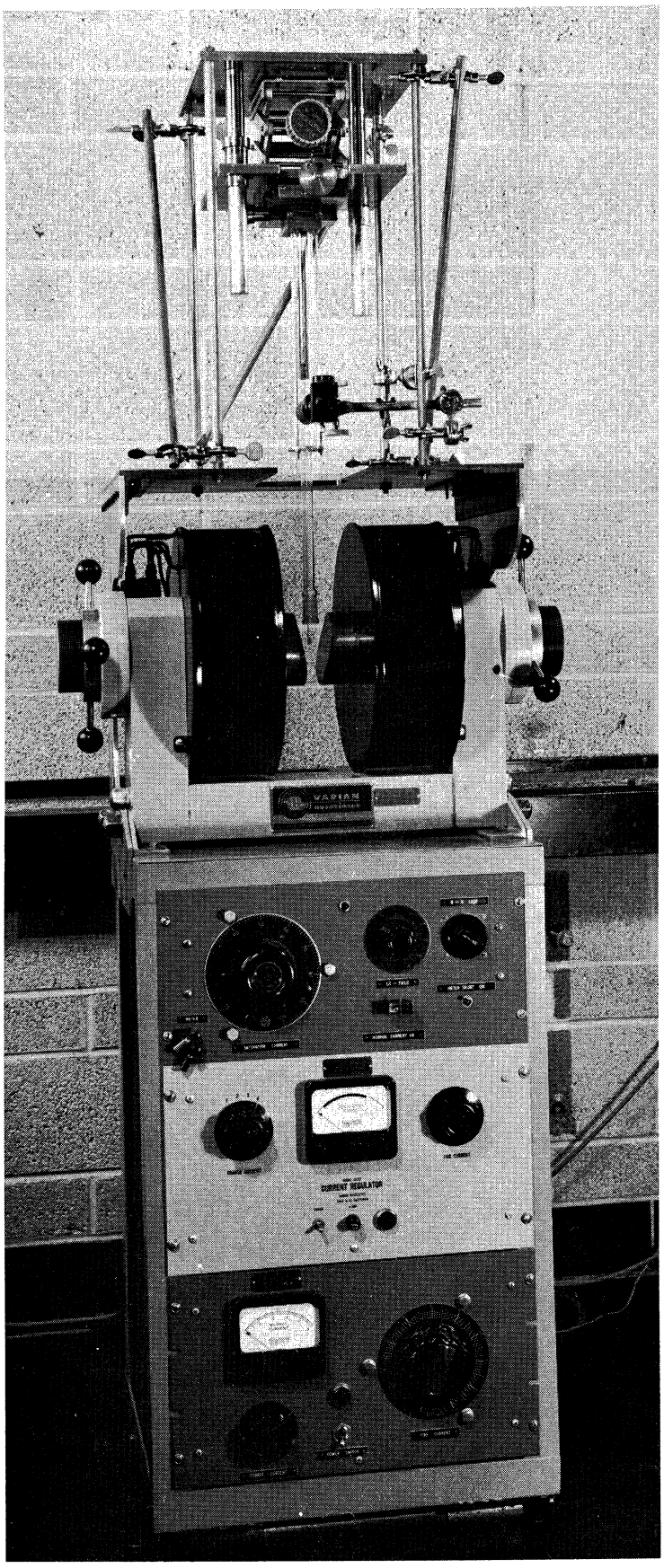

Fig. 23. The Faraday balance.

were weighed into 2-mm capsules which were sealed at one end. The glass rod suspended between the magnetic pole faces has a small receptacle at the end into which the samples were placed. The glass rod is suspended from a platform which can be adjusted in three directions for positioning the sample between the poles of the magnet. The poles are such that a position can be found which places the sample in a nonhomogeneous magnetic field. A telescope equipped with a filar eyepiece is focused on a graduated scale for accurately reading the displacement of the sample. Metallic nickel, which has a saturation moment of 54.39 emu, was used as the standard in determining the field gradient. The errors in the measurement were introduced in the weighing of the small sample (about .0100 gm) and the placement of the sample in a field of known $\partial H/\partial X$. The largest error was introduced in weighing the sample. The error in this measurement was about $\pm$ 1%.

The samples were prepared from C.P. NiO, Li_2CO_3, and Fe_2O_3. The components were mixed by ball-milling in acetone for 6 hours. The ball-milled oxides were pressed into compacts and heated for various lengths of time at the specified temperature in a tubular globar furnace. The samples were placed in a platinum boat which was attached to a ceramic rod for quick removal from the furnace. The platinum boat was placed in the cold zone of the furnace, and the furnace was flushed with the gas in which the reaction was to be run. The platinum boat was then inserted into the hot zone. The temperature was measured with a chromel-alumel thermocouple which was positioned next to the sample. About 3 minutes were required for the sample to reach furnace temperature. At the end of a specified time, the samples were removed from the furnace and quenched.

In the initial stages of the experiments, the samples were placed in the cold zone and the furnace evacuated to de-gas the sample. The furnace

was then filled with the desired gas. It was found, however, that more oxygen was introduced into the furnace through leaks in the system than was removed. Therefore, this procedure was abandoned, and the samples were flushed in the gas for an extended period of time.

The water vapor of the nitrogen and oxygen was removed by passing the gas through a U tube placed in dry ice and acetone. The temperature was controlled within ± 1° by placing a chromel-alumel thermocouple next to the sample. Prepurified N_2 and commercial grade O_2 were used.

As pointed out in Section 2, ferrous iron forms in the initial stage of the reaction. In air or oxygen atmosphere, this ferrous iron is oxidized as the reaction nears completion. In a nitrogen atmosphere there is no way in which the ferrous iron can be oxidized. Therefore, the ferrous iron formed in the initial stage of the reaction remains in the sample. The ferrous iron content for the reaction between NiO and Fe_2O_3 and between Li_2CO_3 and Fe_2O_3 in nitrogen is given in Tables XI and XII.

3.3.2 Results and Conclusions.—The data for the percent of reaction at the various temperatures are tabulated in Tables XIII and XIV for the reactions between NiO and Fe_2O_3 and between Li_2CO_3 and Fe_2O_3, respectively. The percent reacted vs. time for the reaction NiO + Fe_2O_3 in air and oxygen atmospheres is plotted in Fig. 24. The reactions in air and in oxygen are similar, except for the fact that the one in oxygen is somewhat retarded. The plot of $(1 - \sqrt[3]{1 - x/100})^2$ vs. time for the reaction in air is shown in Figs. 25 and 26. At the lower temperatures, and in the initial stages at the higher temperatures, this plot is linear, indicating that Jander's equation is valid. The same data plot for the reaction in oxygen is so similar that it is not included.

The percent of reaction vs. time for the same reaction in nitrogen is given in Fig. 27. At any given temperature the reaction proceeds faster

TABLE XI

THE FeO CONTENT OF NiO + Fe_2O_3 HEATED IN A NITROGEN ATMOSPHERE

Temp., °C	Time	Wt. % FeO
700	60	2.60
800	10	2.87
800	20	2.80
800	30	2.81
800	40	2.75
800	50	2.73
800	60	2.89
800	90	2.84
800	240	2.87
850	240	2.87
900	120	2.82

TABLE XII

THE FeO CONTENT OF Li_2CO_3 + $5Fe_2O_3$ HEATED IN A NITROGEN ATMOSPHERE

Temp., °C	Time	Wt. % FeO
600	10	2.78
600	20	2.84
600	30	2.63
600	40	2.87
600	50	2.95
600	60	2.92

TABLE XIII

THE PERCENT REACTION OF NiO + Fe_2O_3 AS A FUNCTION OF REACTION TIME AND TEMPERATURE

Percent Reaction-Oxygen Atmosphere

Time (min)	800°C	850°C	900°C	950°C
10	6.92	17.83	41.74	65.42
20	12.17	28.32	54.92	77.97
30	---	34.81	60.41	84.30
40	18.58	45.75	66.39	87.00
50	21.46	43.03	70.19	88.54
60	23.56	46.81	72.76	90.17
90	30.33	53.87	79.00	91.97
120	38.30	61.34	82.16	94.23
180	40.36	67.51	86.98	96.48
240	49.06	72.74	88.98	96.50

Percent Reaction-Nitrogen Atmosphere

Time (min)	700°C	750°C	800°C	850°C
10	21.10	29.61	45.87	62.00
20	24.46	38.40	54.92	74.03
30	27.32	42.48	62.24	80.12
40	28.90	45.62	67.23	84.63
50	30.00	47.52	69.65	90.34
60	---	50.02	71.78	89.80
90	33.43	56.18	79.92	94.42
120	36.90	60.03	82.87	98.1
180	42.72	67.00*	89.28	100.00
240	44.72	71.80	95.61	100.00

Percent Reaction-Air Atmosphere

Time (min)	750°C	800°C	850°C	900°C	950°C	1000°C
10	3.98	8.15	19.36	40.47	66.72	87.33
20	5.99	13.64	30.34	54.78	77.83	93.62
30	8.20	17.31	37.94	62.19	84.48	95.77
40	9.10	20.34	43.16	67.27	89.48	96.29
50	11.15	23.27	47.22	71.38	90.24	95.93
60	12.18	25.70	50.49	74.53	92.02	97.71
90	15.51	32.03	57.96	81.33	94.29	96.53
120	18.46	36.78	63.73	84.83	95.81	98.45
180	23.39	42.70	71.95	88.99	95.84	---
240	27.77	46.92	75.45	91.97	96.06	---

*Time 190 min.

TABLE XIV

THE PERCENT REACTION OF $Li_2CO_3 + 5Fe_2O_3$ AS A FUNCTION OF REACTION TIME AND TEMPERATURE

Percent Reaction-Oxygen Atmosphere

Time (min)	550°C	575°C	600°C	625°C
10	---	---	2.99	12.10
20	---	2.46	6.85	30.30
30	1.03	3.65	11.91	49.14
40	---	4.48	16.24	---
50	---	5.37	20.35	73.62
60	2.00	6.61	24.00	79.70
90	3.24	10.25	42.42	86.38
120	4.69	14.00	61.43	90.18
180	6.62	19.26	78.23	88.22
240	6.54	28.06	84.83	88.00

Percent Reaction-Air Atmosphere

Time (min)	550°C	575°C	600°C	625°C
10	---	---	3.96	---
20	---	2.33	9.49	40.55
30	---	3.98	16.64	61.0
40	1.41	4.78	21.41	75.35
50	---	6.28	30.81	82.35
60	2.50	7.70	34.50	84.74
90	3.60	13.09	54.81	88.70
120	5.48	17.21	70.11	88.80
180	7.66	29.48	85.81	88.20
240	10.91	41.37	87.60	88.10

Percent Reaction-Nitrogen Atmosphere

Time (min)	450°C	508°C	550°C	600°C
10	17.77	25.52	36.64	60.90
20	19.71	28.59	45.59	73.17
30	21.77	31.49	53.55	81.26
40	22.75	34.22	58.17	87.86
50	23.42	33.50	59.30	91.51
60	23.95	35.93	66.98	94.97
90	24.39	39.27	74.00	---
120	25.57	41.94	77.31	---
180	26.47	48.72	86.00	---
240	28.69	53.37	94.16	---

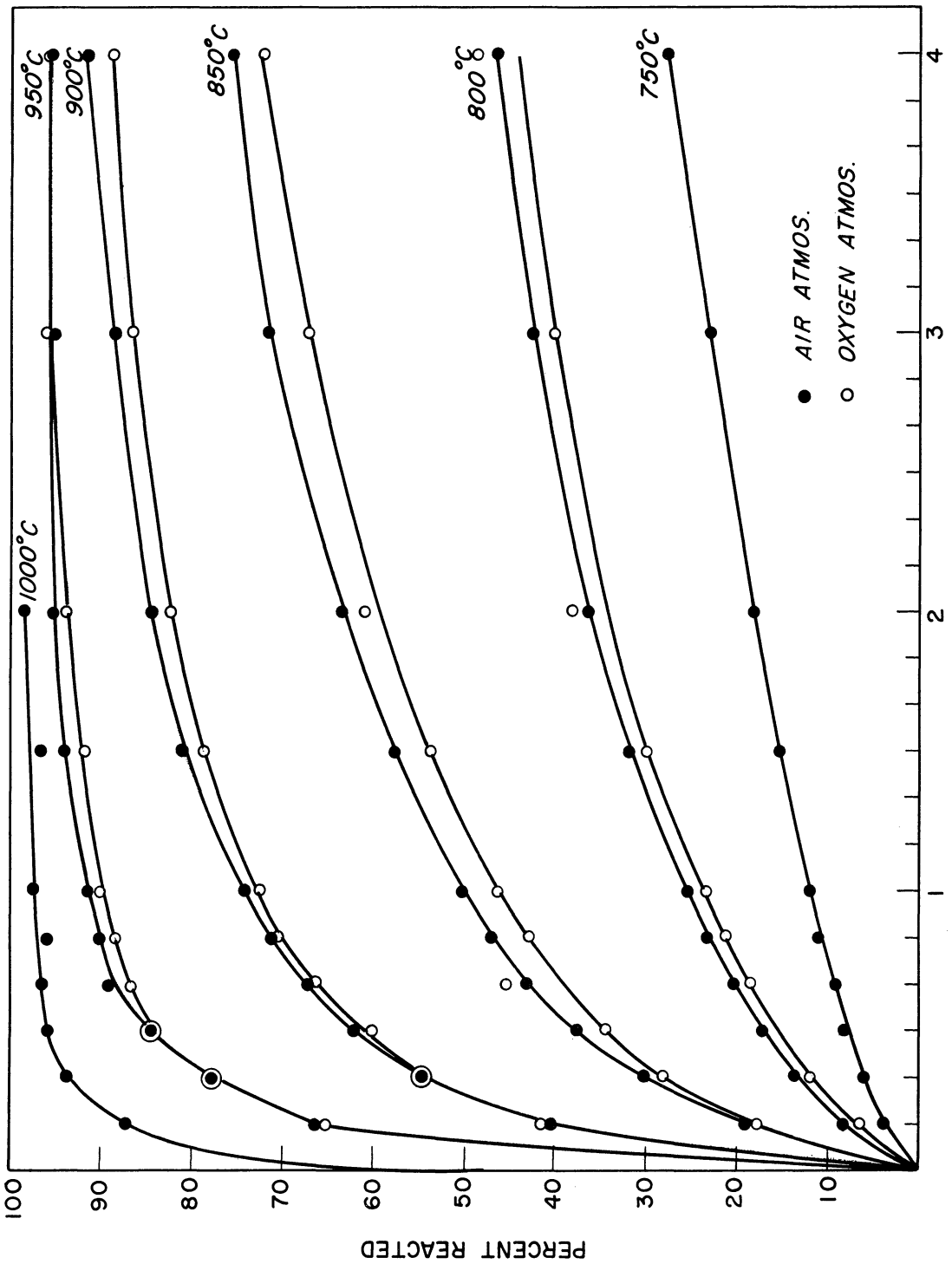

Fig. 24. Percent reacted vs. time for the reaction between NiO and Fe_2O_3 in air and oxygen.

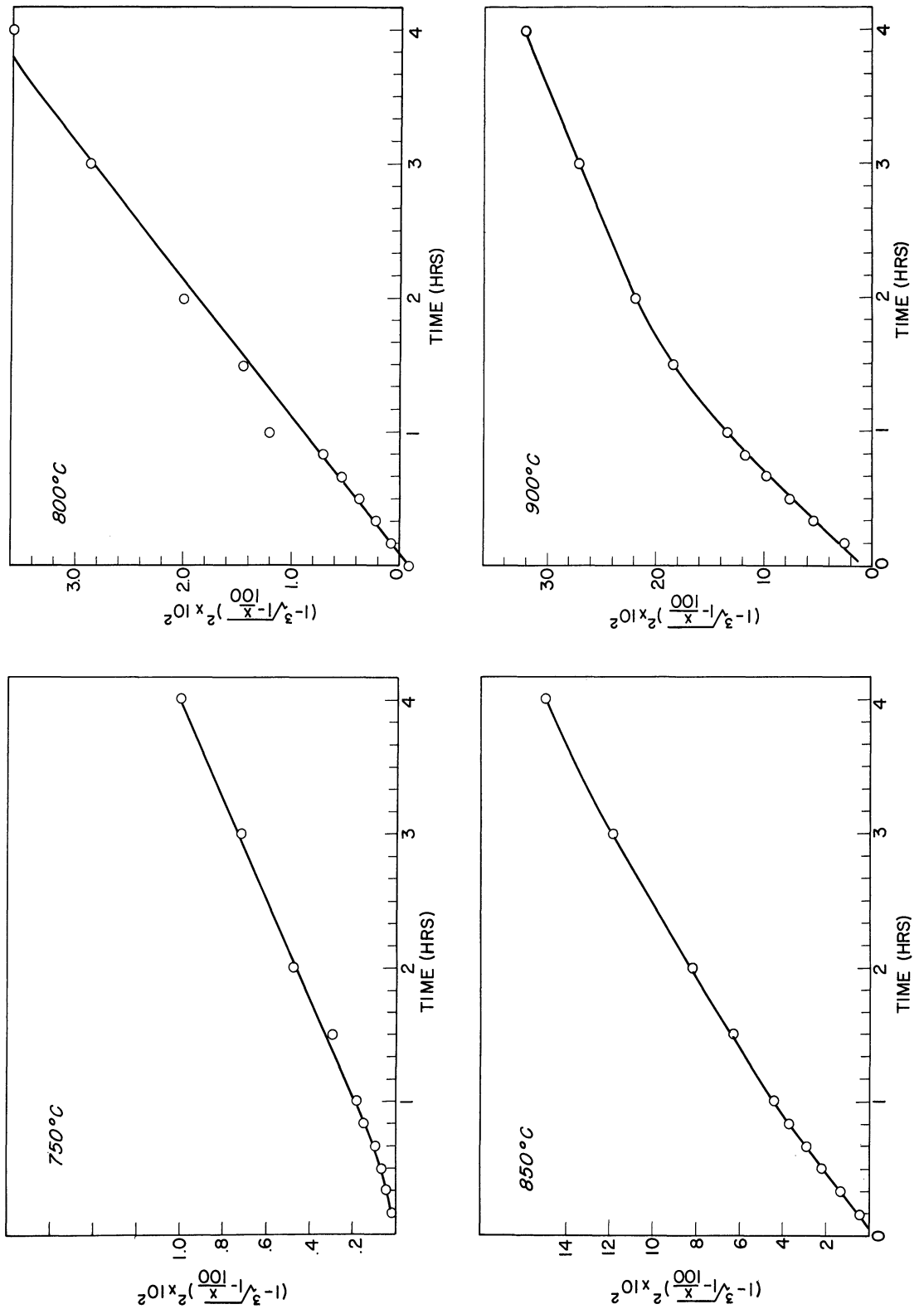

Fig. 25. $(1 - \sqrt[3]{1 - x/100})^2$ vs. time for the reaction between NiO and Fe_2O_3 in air.

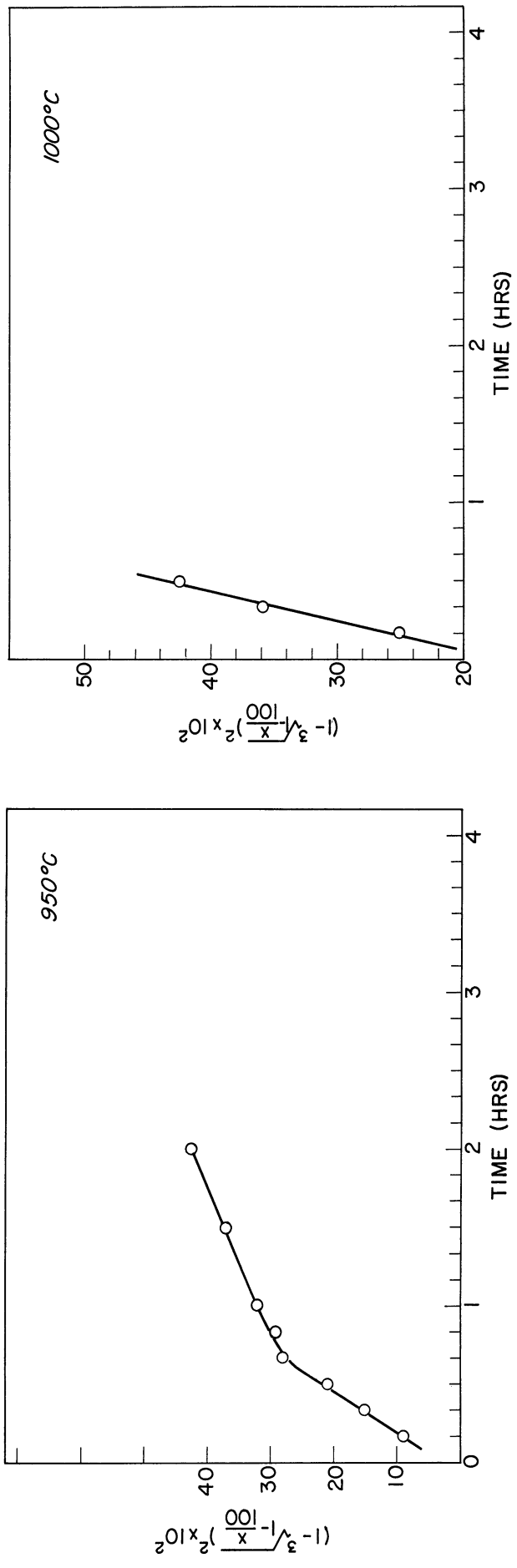

Fig. 26. $(1 - \sqrt[3]{1 - x/100})^2$ vs. time for the reaction between NiO and Fe_2O_3 in air.

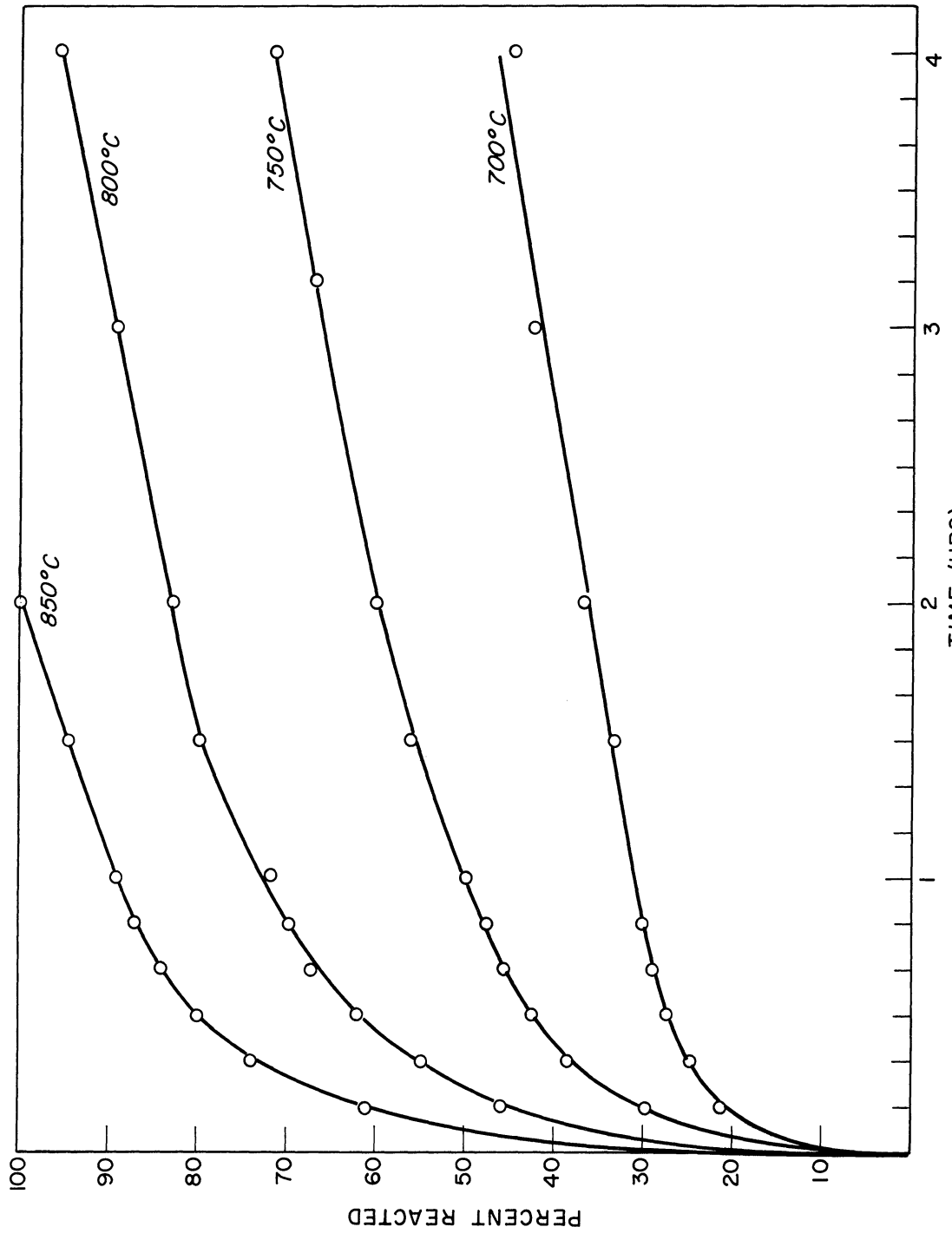

Fig. 27. Percent reacted vs. time for the reaction between NiO and Fe_2O_3 in nitrogen.

in nitrogen than in air or oxygen. The plot of $(1 - \sqrt[3]{1 - x/100})^2$ vs. time is given in Fig. 28. The data are linear over the entire temperature range. In general, the data for the reaction in nitrogen atmosphere fit Jander's equation over a greater portion of the reaction than do the data for the reaction in air atmosphere.

The reaction between Li_2CO_3 and Fe_2O_3 occurs at lower temperatures than does the reaction between NiO and Fe_2O_3. The reaction between NiO and Fe_2O_3 is slow at 700°C in air, while the reaction between Li_2CO_3 and Fe_2O_3 is completed in 5 minutes at this temperature. The reaction also occurs at a measurable rate over a smaller temperature interval. The percent reacted vs. time for the reactions in air and oxygen is given in Fig. 29 over the temperature interval 550° to 625°C. The reactions in air and oxygen again are very similar, with the exception that the reaction is somewhat retarded in oxygen. The data for this reaction do not fit Jander's equation. The plot of the percent reacted vs. time is linear in the initial stages of the reaction. This implies that the rate equation is of the type $dx/dt = k$.

The percent reacted vs. time for the reaction in nitrogen is plotted in Fig. 30. The reaction in nitrogen is considerably different from that in air or oxygen. The reaction occurs at a lower temperature, and in this case the data fit Jander's equation. The plot of $(1 - \sqrt[3]{1 - x/100})^2$ vs. time for this reaction is given in Fig. 31. At 450°C the fit is not good. At 508°C the curve is linear in the initial part of the reaction. At 550°C and 600°C the data fit the equation relatively well.

Several samples were heated in a CO_2 atmosphere to determine if the reaction was slowed down or stopped. The rate of reaction in CO_2 was found to be similar to that in nitrogen. This seems to rule out the decomposition of Li_2CO_3 as the rate-determining step in the reaction.

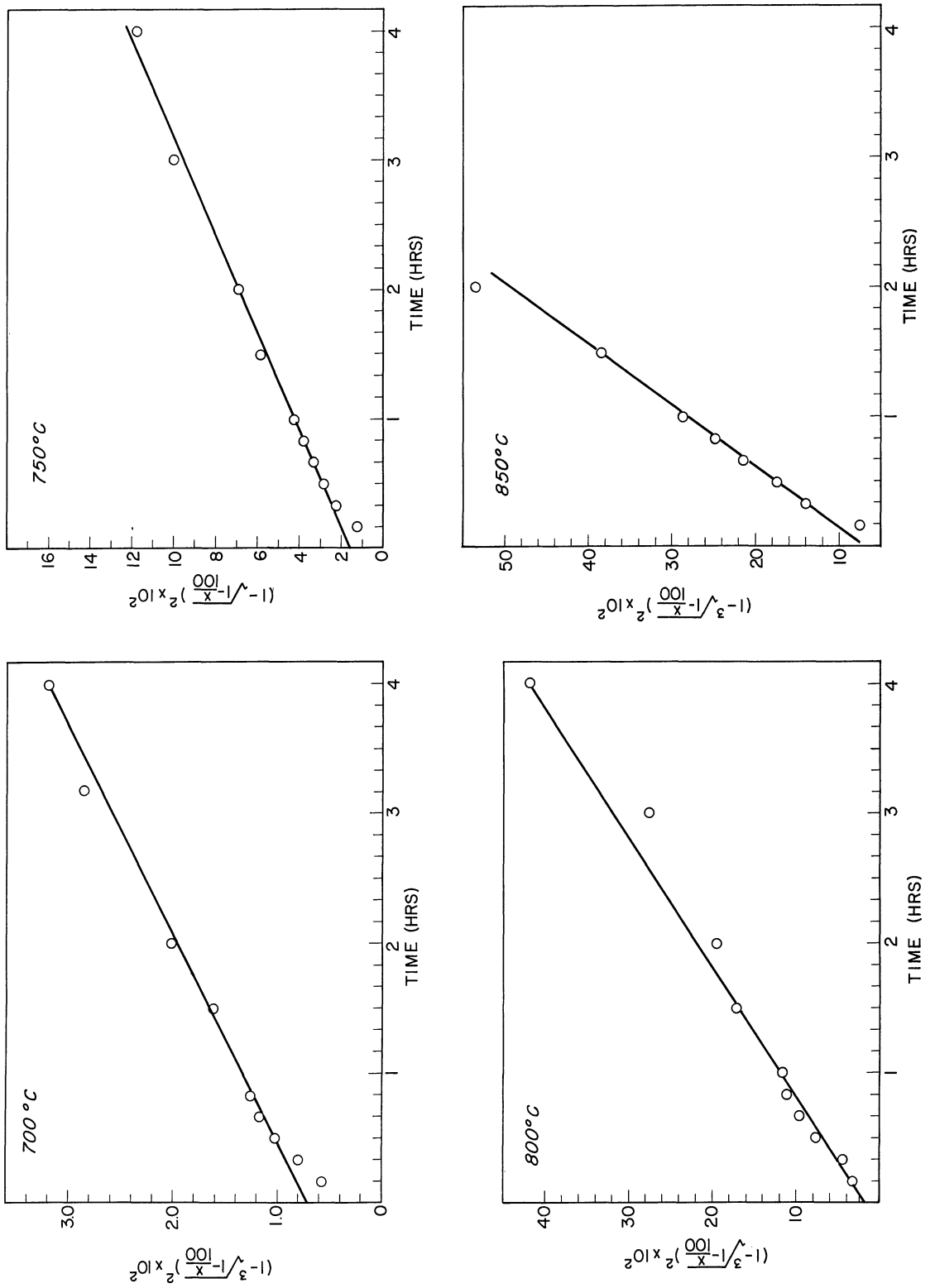

Fig. 28. $(1 - \sqrt[3]{1 - x/100})^2$ vs. time for the reaction between NiO and Fe_2O_3 in nitrogen.

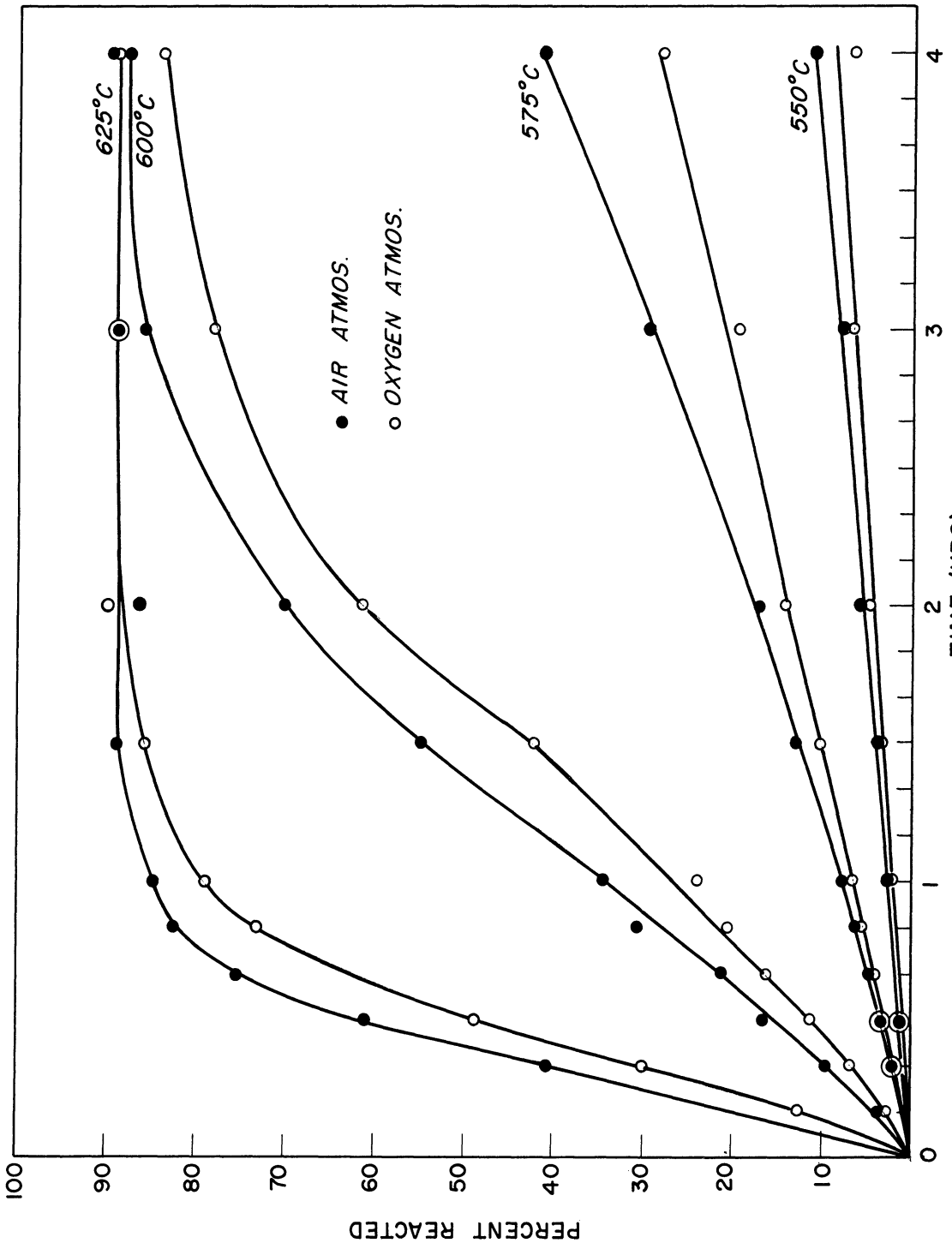

Fig. 29. Percent reaction vs. time for the reaction between Li_2CO_3 and $5Fe_2O_3$ in air and oxygen.

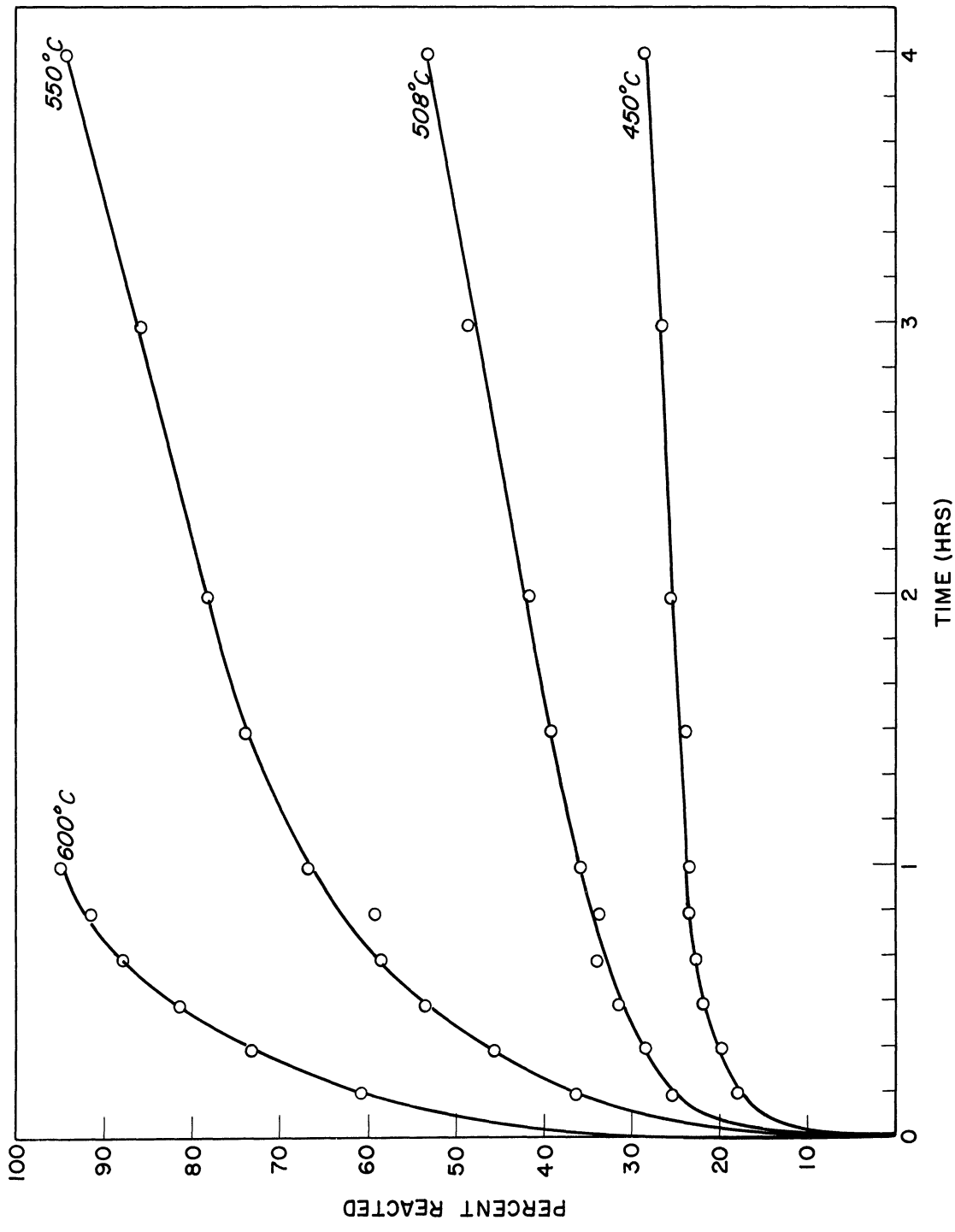

Fig. 30. Percent reacted vs. time for the reaction between Li_2CO_3 and $5Fe_2O_3$ in nitrogen.

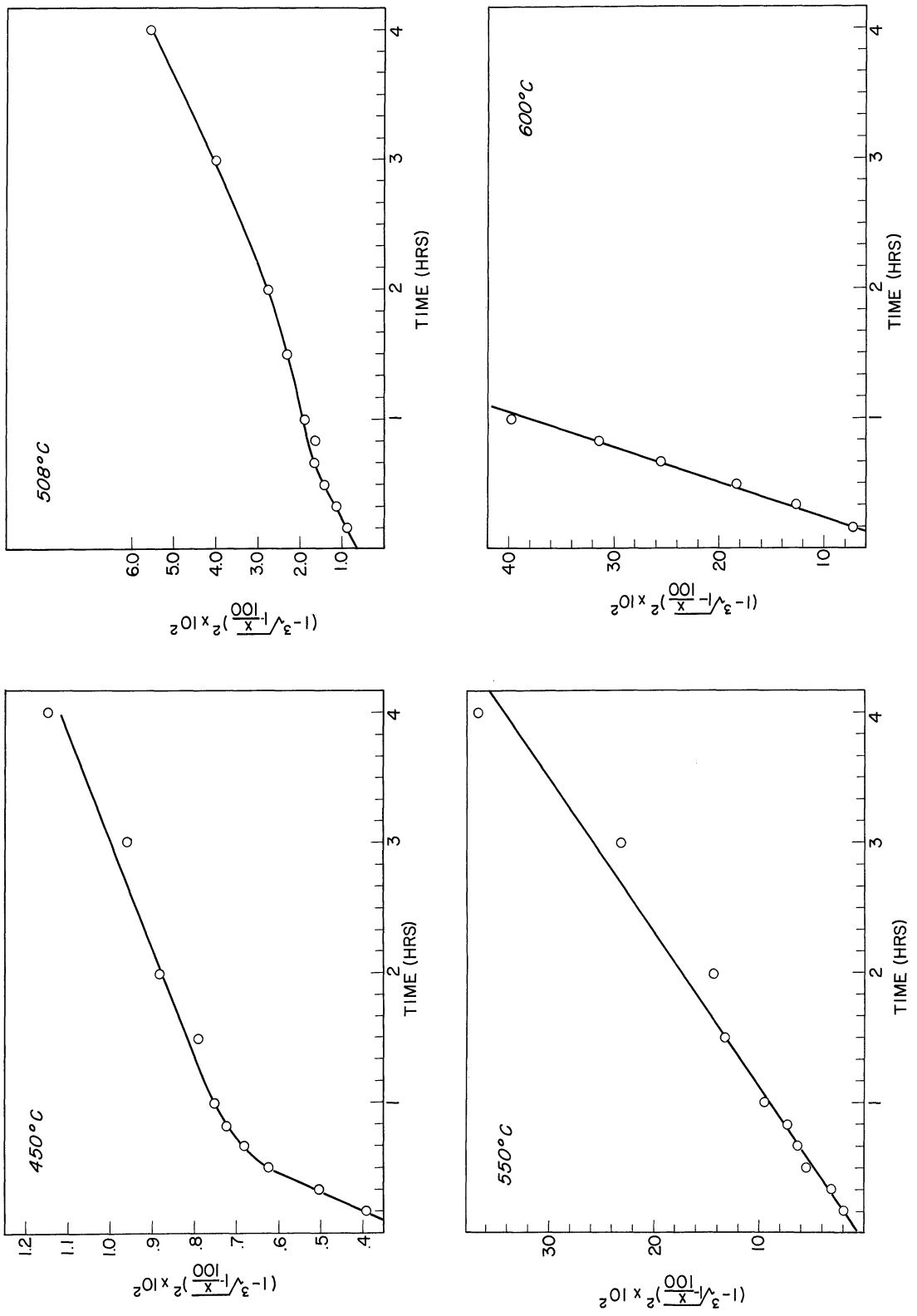

Fig. 31. $(1 - \sqrt[3]{1 - x/100})^2$ vs. time for the reaction between Li_2CO_3 and $5Fe_2O_3$ in nitrogen.

The activation energies for the reactions have been obtained from a plot of log k vs. 1/T. This plot is shown in Fig. 32. The data are tabulated in Table XV.

TABLE XV

THE ACTIVATION ENERGIES FOR THE FORMATION OF $NiFe_2O_4$ AND $LiFe_5O_8$ IN AIR AND NITROGEN ATMOSPHERES

Compound	Atmosphere	ΔH (Kcal/mole)
$NiFe_2O_4$	Air	55.6
$NiFe_2O_4$	Nitrogen	51.2
$LiFe_5O_8$	Air	74.4
$LiFe_5O_8$	Nitrogen	46.7

The facts can be summarized as follows. The rate of the solid-state reaction for both the formation of $NiFe_2O_4$ and $LiFe_5O_8$ increases as the oxygen pressure decreases. The difference between the rates of reaction in air and oxygen is small, while the difference between the rates in air and nitrogen is pronounced. The kinetics of the reaction between NiO and Fe_2O_3 in air fit Jander's equation over a part of the reaction, while the same reaction in nitrogen fits this equation over the entire course of the reaction. The kinetics of the reaction between Li_2CO_3 and Fe_2O_3 in air and in oxygen cannot be explained by the mechanism assumed in Jander's equation. The reaction is best expressed by the rate equation $dx/dt = k$. The data for the same reaction in nitrogen fit Jander's equation. The activation energy for both reactions is lower in nitrogen than in air.

Since Jander's equation assumes that the rate-determining step is the diffusion of the reacting components through the product layer formed at the interface, it must be concluded that this is more nearly the case in

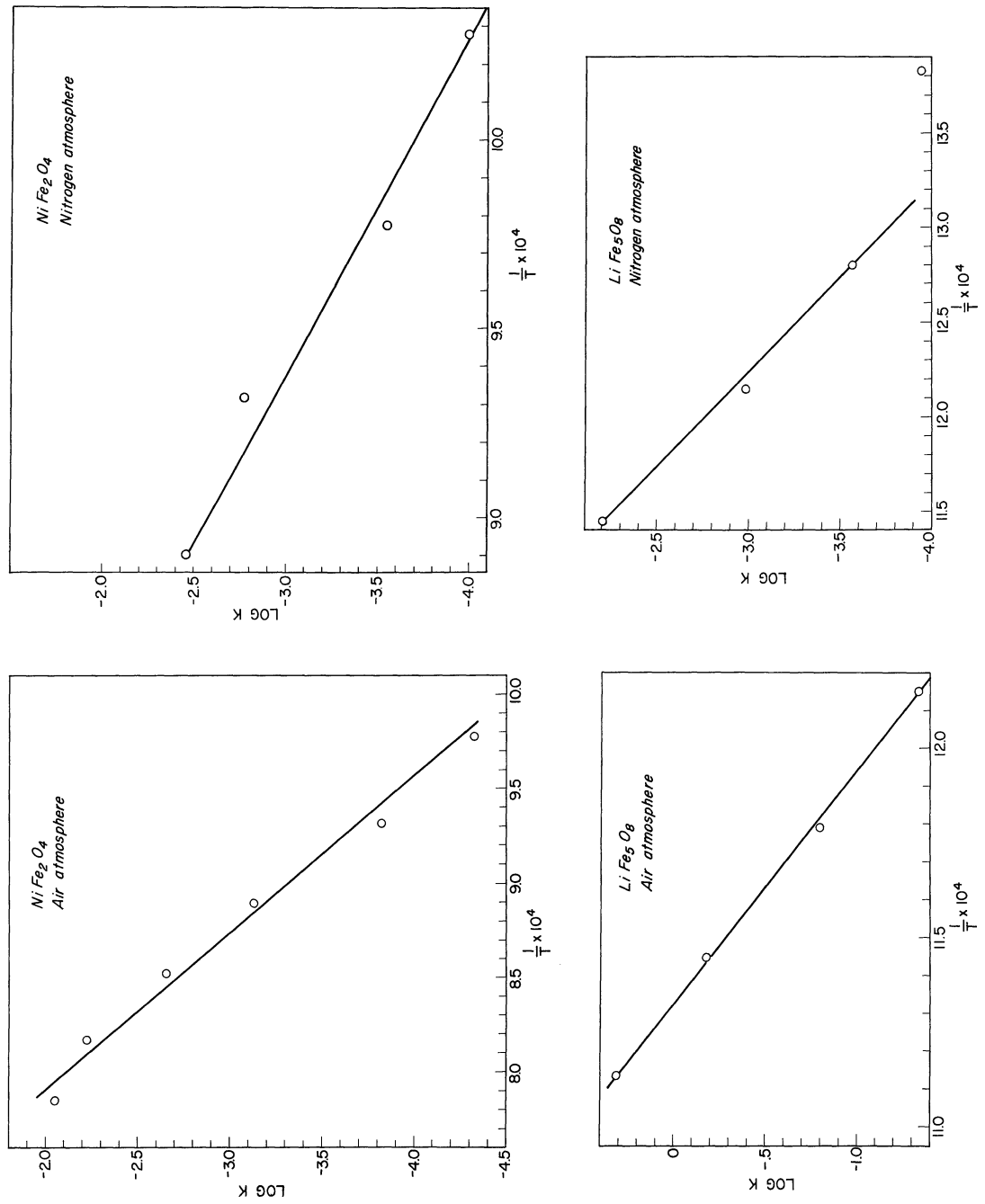

Fig. 32. Log k vs. 1/T.

nitrogen than it is in air or oxygen. It is suggested here that, when there is only a small amount of oxygen in the atmosphere, ferrous iron forms readily, and facilitates the spinel formation at the boundaries. In air and oxygen, only a very small amount of ferrous iron forms at these temperatures, and the boundary reactions play a larger role in determining the rate of reaction. At the low temperatures at which Li_2CO_3 reacts with Fe_2O_3 in air and oxygen, the boundary reactions appear to be the rate-determining step. The diffusion of the relatively small lithium ion (if this is the diffusing component) through the product layer plays no role in determining the rate of the reaction.

3.4 THE Ddensification PROCESS

The densification process considered here is not concerned with the X-ray density of the material but with the apparent density of the bulk material. The change in apparent density is simply a measure of the change of porosity of the material. In order for material to densify, it is necessary that some process or processes involving material transport occur. The driving force for this reaction is generally considered to arise from the reduction in surface energy resulting from the decreased total surface area of the denser material. Various mechanisms have been proposed for the necessary transport of material. Those most commonly considered are viscous flow, vaporization and subsequent condensation, diffusion through the lattice, and surface migration. The relative contributions of the different mechanisms have not been established, and evidently will vary greatly from system to system. Shaler[4] contends that metals must flow to densify, and that densification cannot progress by evaporation and condensation or by surface diffusion alone. In a review of the mechanism of sintering, Roberts[41] divides the process into two stages. The first stage is character-

ized by connected pores and the second stage by disconnected pores. Evaporation and condensation play a part in densification during the first stage, but contribute only to spheroidization of pores in the second stage. A flow mechanism is used to account for densification in the second stage.

The densification of $Ni_{.4}Zn_{.6}Fe_2O_4$ as a function of the firing temperature is shown in Fig. 33. The green density of this material is 2.60, so there is little densification at 1000°C and below. The densification progresses with increasing temperatures up to a density of approximately 5.2 gm/cc, which is about 97% of the theoretical density.

To study the effect of the initial density on the final density of ferrites, two investigations were conducted. In one case the reaction time was held constant at 4 hours, and cores with different green densities were caused to react at several different temperatures. In the other case, the effect of reaction time was investigated at constant temperature for two different green densities. It was found that the total force exerted on the die was not a good criterion of the degree of compacting of the material. Because of friction between the walls of the die, green compacts made with the same pressing pressure showed a considerable spread in density. Therefore, the green density of the unfired cores was used as a measure of compacting. This density was obtained by measuring the mass and volume of the core. The volume of the green cores was obtained by measuring the cores with a micrometer. A slight warp in the cores after heating made this same procedure unreliable, so the reacted cores were coated with a thin wax layer and the volumes were determined by weighing the cores in air and in water.

For sufficiently high reaction temperatures, it is expected that the final density will approach the X-ray density for any reasonable value of

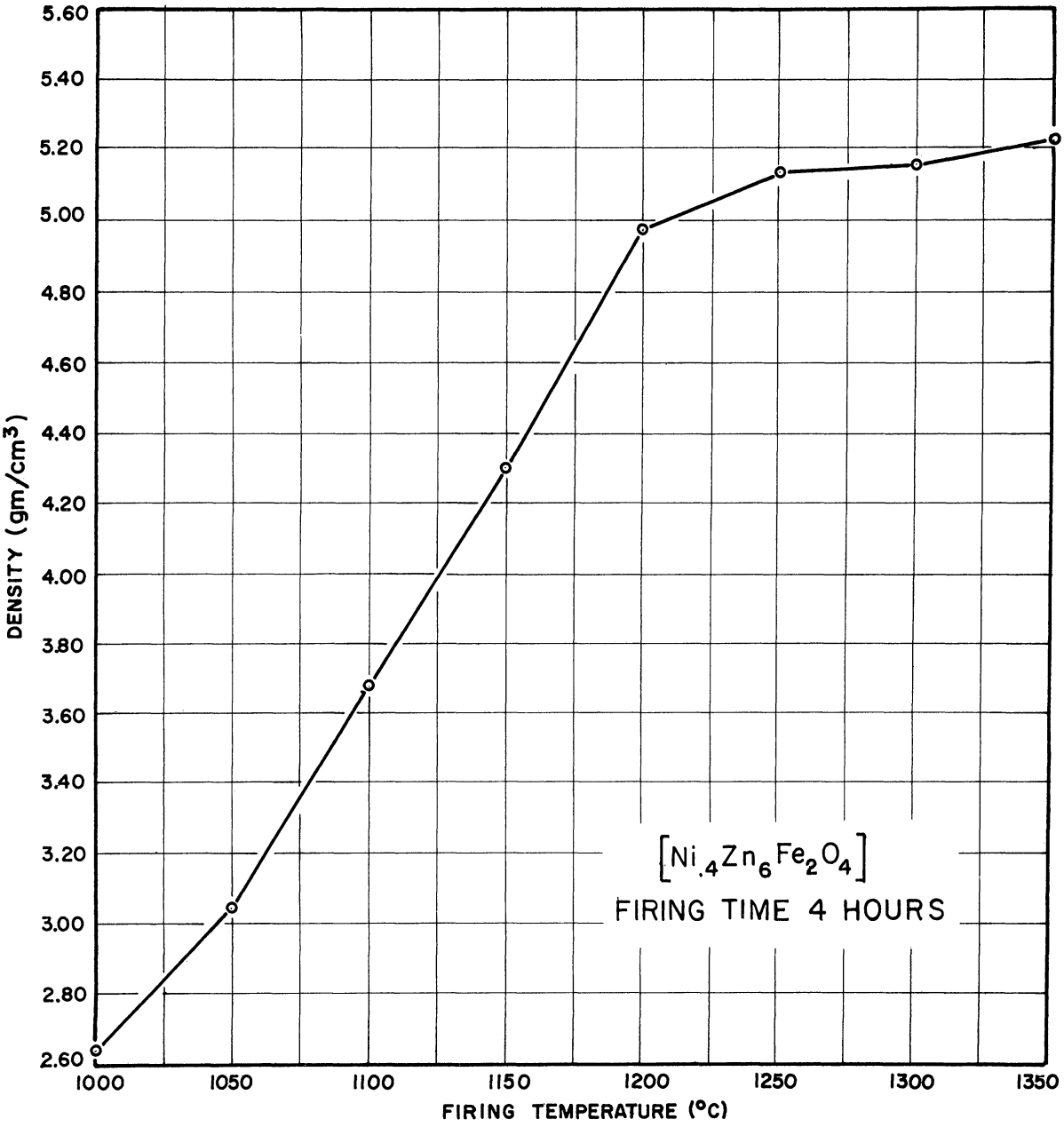

Fig. 33. Density vs. firing temperature.

green density. Similarly, at sufficiently low reaction temperatures there will be no reaction at all, and the final density will equal the green density. If the difference, ΔD, between the final and green densities is plotted against the green density, each normalized by division by the X-ray density, these two limits would be represented by the two solid lines in Fig. 34. The green density is represented by g.

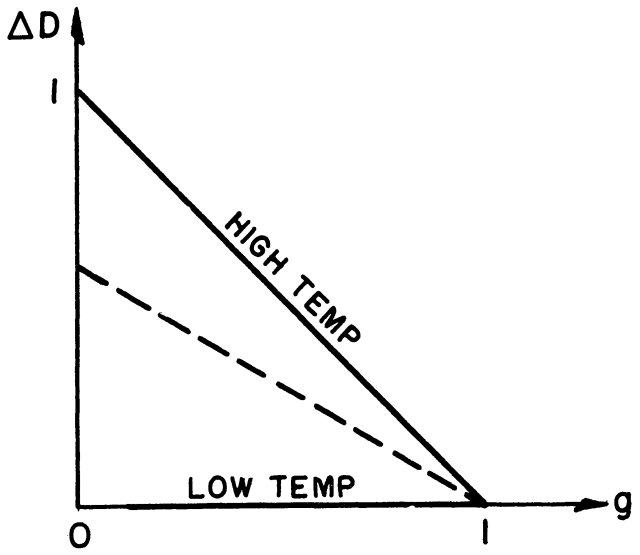

Fig. 34. Expected behavior of density change upon firing.

At an intermediate temperature, the relationship might still be linear as represented by the dashed line in Fig. 34. Such a line would be given by the equation

$$\Delta D = -f_1(T)g + f_2(T) \quad , \qquad (9)$$

where the slope $-f_1$ and the intercept f_2 are functions of the firing temperature T. It is required that $f_1 = f_2 = 0$ at low temperatures, and that $f_1 = f_2 = 1$ at high temperatures. If the lines actually do pass through the point (1,0) as in Fig. 34, this implies that $f_1(T) = f_2(T)$.

In Table XVI the experimental values of the green density, final density, and ΔD are given. In Fig. 35 the values of ΔD have been plotted as a function of the green density. There is considerable scatter in the

TABLE XVI

DATA ON THE DENSIFICATION OF $Ni_{.4}Zn_{.6}Fe_2O_4$; REACTION TIME 4 HOURS

1000°C			1050°C			1100°C		
Green Density	Final Density	ΔD	Green Density	Final Density	ΔD	Green Density	Final Density	ΔD
1.97	2.11	.14	1.99	2.70	.71	2.02	3.22	1.20
2.11	2.27	.16	2.13	2.72	.59	1.99	3.34	1.35
2.17	2.38	.21	1.94	2.57	.63	1.92	3.18	1.26
2.15	2.35	.20	2.06	2.70	.64	1.98	3.20	1.22
1.96	2.18	.22	2.15	2.87	.72	2.11	3.55	1.44
2.20	2.41	.21	2.11	2.83	.72	2.09	3.48	1.39
2.19	2.42	.23	2.28	2.74	.46	2.15	3.57	1.42
1.97	2.19	.22	2.43	2.94	.51	2.16	3.49	1.33
2.18	2.38	.20	2.51	3.05	.54	2.27	3.68	1.41
2.04	2.23	.19	2.54	3.15	.61	2.29	3.67	1.38
2.29	2.43	.14	2.59	3.25	.66	2.36	3.65	1.29
2.36	2.50	.14	2.60	3.22	.62	2.45	3.58	1.13
2.47	2.61	.14	2.05	2.73	.68	2.52	3.65	1.13
2.13	2.54	.31	2.01	2.67	.66	2.60	3.80	1.20
2.44	2.68	.24				2.60	3.89	1.29
2.50	2.75	.25						
2.48	2.70	.22				2.63	3.95	1.32
2.53	2.77	.24				2.66	3.85	1.19

1150°C			1200°C		
Green Density	Final Density	ΔD	Green Density	Final Density	ΔD
1.96	4.24	2.28	1.95	5.05	3.10
1.92	4.36	2.44	1.92	5.05	3.13
1.98	4.44	2.46	1.92	5.06	3.14
1.92	4.06	2.14	1.98	5.06	3.08
1.99	4.21	2.22	2.07	5.12	3.05
1.98	4.18	2.20	2.06	5.10	3.04
2.18	4.20	2.02	2.12	5.12	3.00
2.04	4.09	2.05	2.13	5.08	2.87
2.18	4.27	2.09	2.21	5.11	2.90
2.15	4.30	2.15	2.20	5.11	2.91
2.14	4.33	2.19	2.33	5.08	2.75
2.28	4.27	1.99	2.37	5.09	2.72
2.40	4.17	1.77	2.48	5.05	2.57
2.43	4.23	1.80	2.46	5.10	2.64
2.52	4.46	1.94	2.58	5.13	2.55
2.50	4.50	2.00	2.55	5.14	2.59
2.63	4.50	1.87	2.64	5.14	2.50
2.56	4.46	1.90	2.63	5.13	2.50

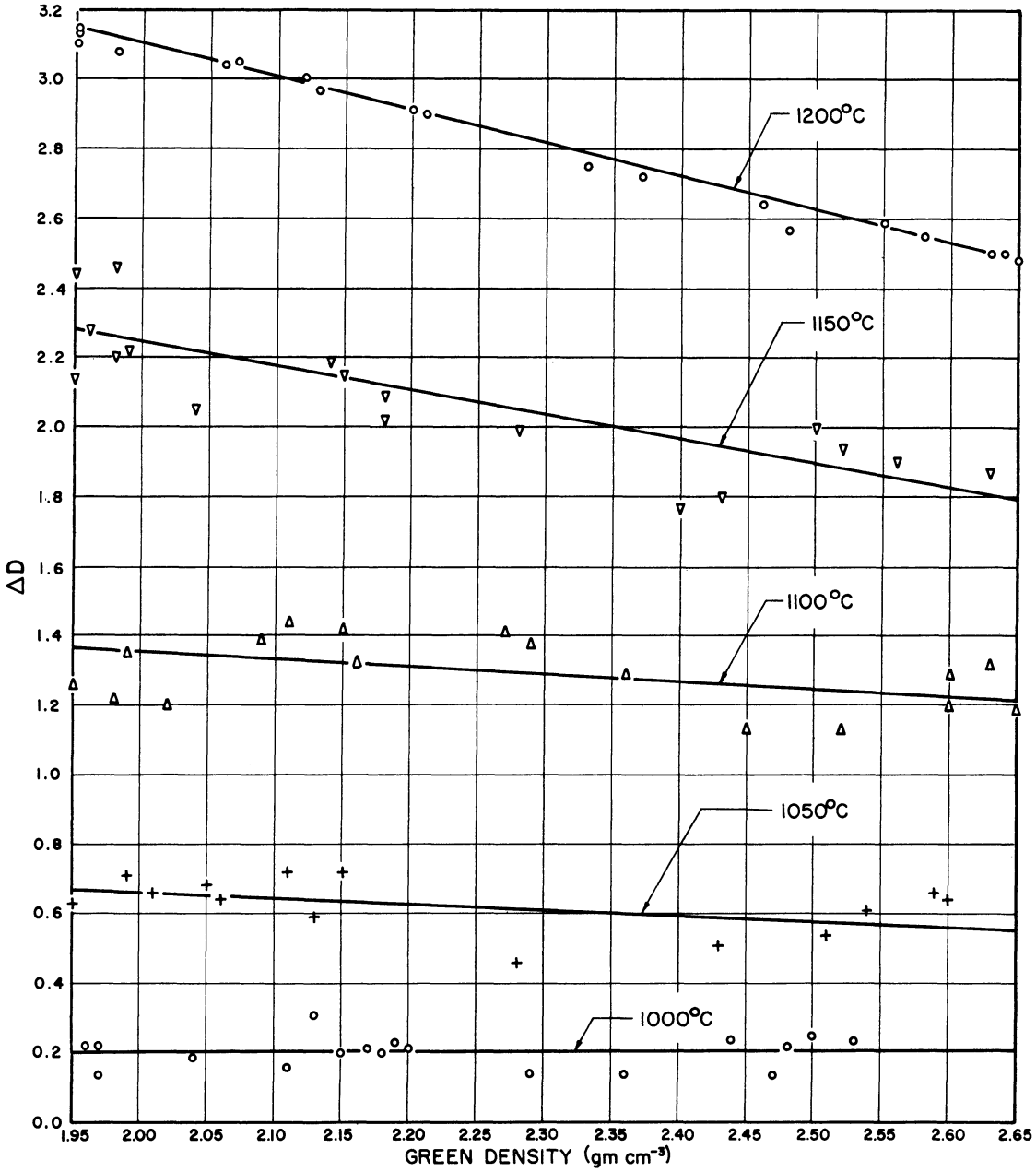

Fig. 35. Change in density vs. green density for several firing temperatures; firing time 4 hours.

data, particularly at the middle temperatures. At 1000°C the increase in density is almost constant. At 1200°C the increase in density plus the green density is almost constant. This is to be expected, since the final density of all the samples reacted at 1200°C is almost constant. (See Table XVI.)

The lines shown in Fig. 35 were fitted to the experimental data and used to compute values of f_1 and f_2 of Eq. (9). These values are plotted against the reaction temperatures in Fig. 36. Note that f_1 and f_2 are almost equal throughout the temperature range, indicating that all the lines of Fig. 35 would very nearly pass through a common point, the theoretical X-ray density, if extended.

The wide scatter of points obtained in the above data is the result of the thermal gradient in the furnace. To control the temperature more closely, the samples prepared by varying the reaction time at constant temperature were made by placing all samples in the same location in the furnace. The same procedure as given above was used to obtain the green and final densities.

The data are given in Table XVII. The percent densification was calculated as D/(5.35-green density). These data are plotted in Fig. 37 as a function of the reaction time. It can be seen that the rate of densification is highest for the samples with the higher green density. This is to be expected, since the rate of densification is closely related to the amount of contact area between the particles.

The permeability of the cores fired at 1150°C is plotted as a function of firing time in Fig. 38. It can be seen that the samples with the higher green density have the higher permeability. An interesting correlation between the permeability and percent densification is seen in Figs. 39 and 40. The permeability appears to be related to the percent of densification,

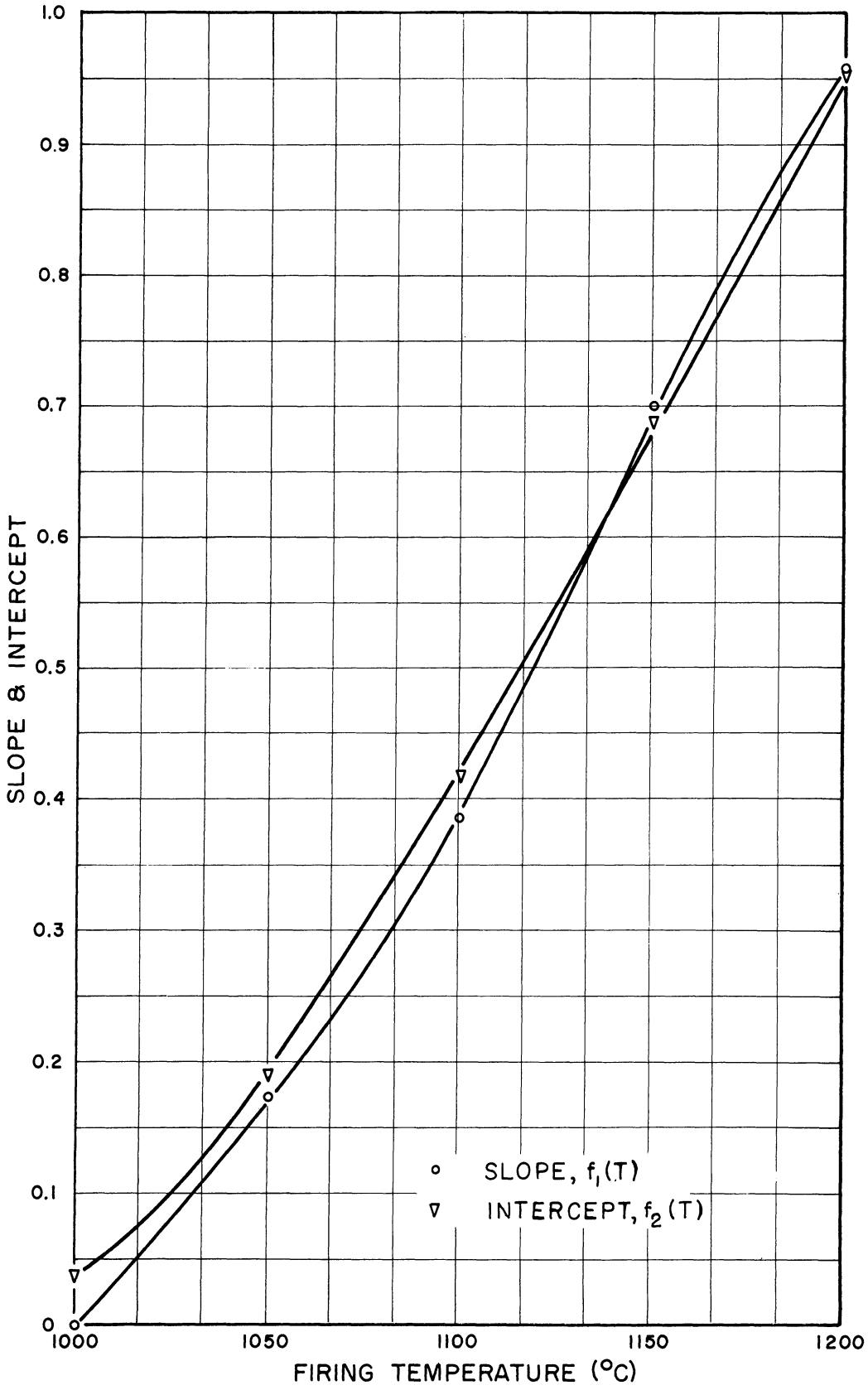

Fig. 36. $f_1(T)$ and $f_2(T)$ of Eq. (9) vs. temperature.

TABLE XVII

DATA ON THE DENSIFICATION OF FERRITES

Green Density	Final Density	Percent Densif.	μ_1	Time (min)	Green Density	Final Density	Percent Densif.	μ_1
			$Ni_{.4}Zn_{.6}Fe_2O_4$ Reacted at 1150°C					
2.07	3.22	34.3	27	3	2.65	3.88	45.5	48
2.10	3.55	44.6	47	5	2.64	4.14	55.6	76
2.03	3.60	48.6	54	7	2.63	4.23	59.2	90
2.05	3.79	52.8	69	10	2.64	4.36	63.8	110
2.06	3.97	58.2	86	15	2.64	4.47	67.8	129
2.11	4.42	71.4	158	40	2.65	4.72	76.8	195
	4.59		180	60	2.64	4.79	79.6	212
2.06	4.64	78.5	199	80	2.65	4.85	81.4	264
2.00	4.75	82.1	233	120	2.66	4.94	84.5	306
1.99	4.93	87.5	290	240	2.64	5.01	87.8	368
			$Ni_{.474}Zn_{.526}Fe_2O_4$ Reacted at 1210°C					
1.96	2.79	24.6	8.2	3	2.64	3.65	37.4	16.1
1.97	2.94	29.0	12.9	5	2.64	3.76	39.3	25.4
1.98	3.06	32.3	20.0	10	2.64	3.92	47.4	44
1.93	3.28	39.5	35.2	20	2.66	4.14	54.8	76
1.95	3.50	45.6	55	40	2.65	4.32	61.8	117
1.96	3.76	53.1	86	80	2.66	4.45	66.3	163
2.00	3.92	57.4	110	120	2.60	4.52	69.5	187
1.99	4.23	66.9	175	240	2.64	4.67	75.2	257
2.00	4.47	74.2	254	480	2.62	4.84	81.0	389
1.92	4.66	79.9	358	900	2.66	4.94	84.5	630

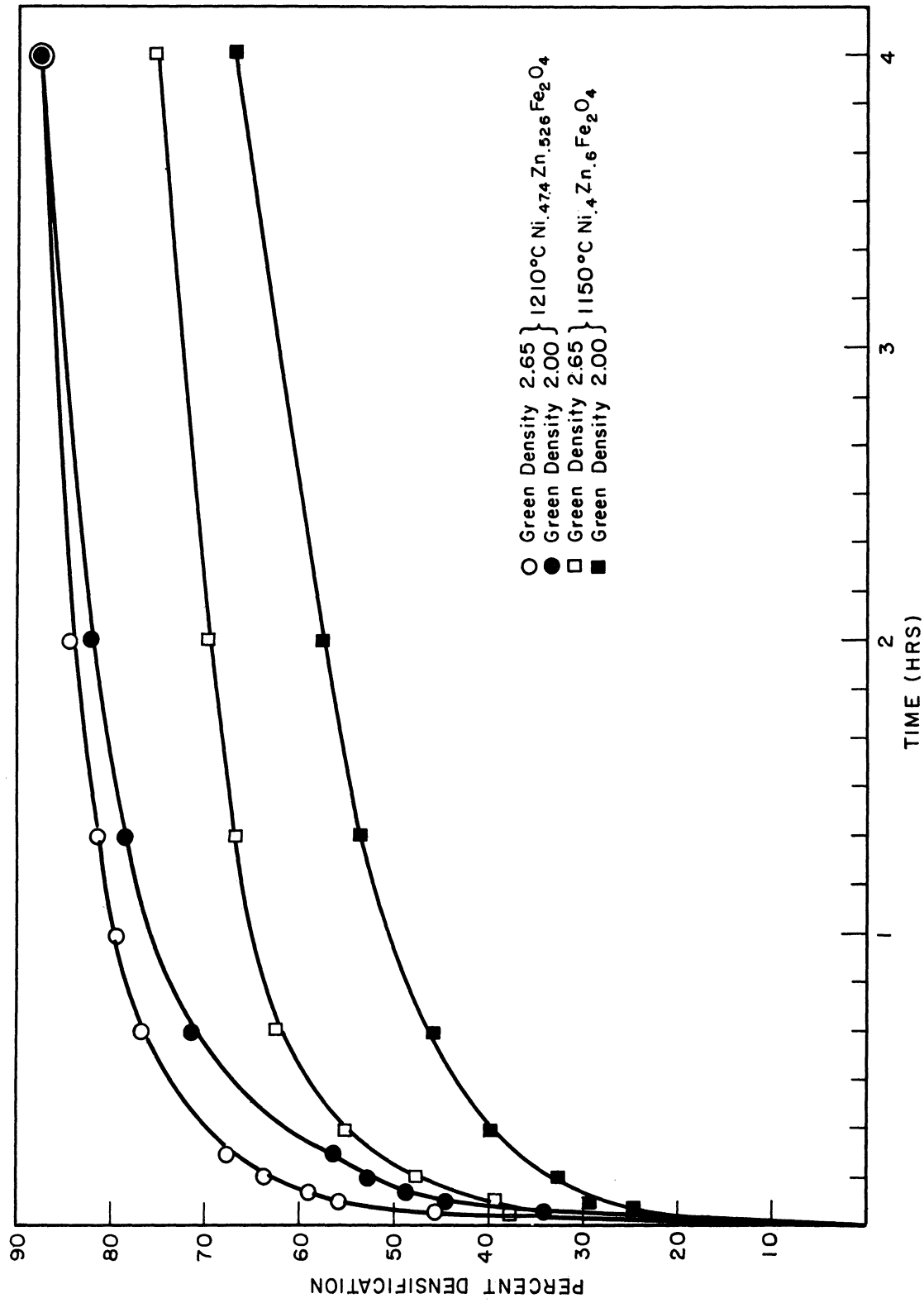

Fig. 37. Percent densification vs. reaction time.

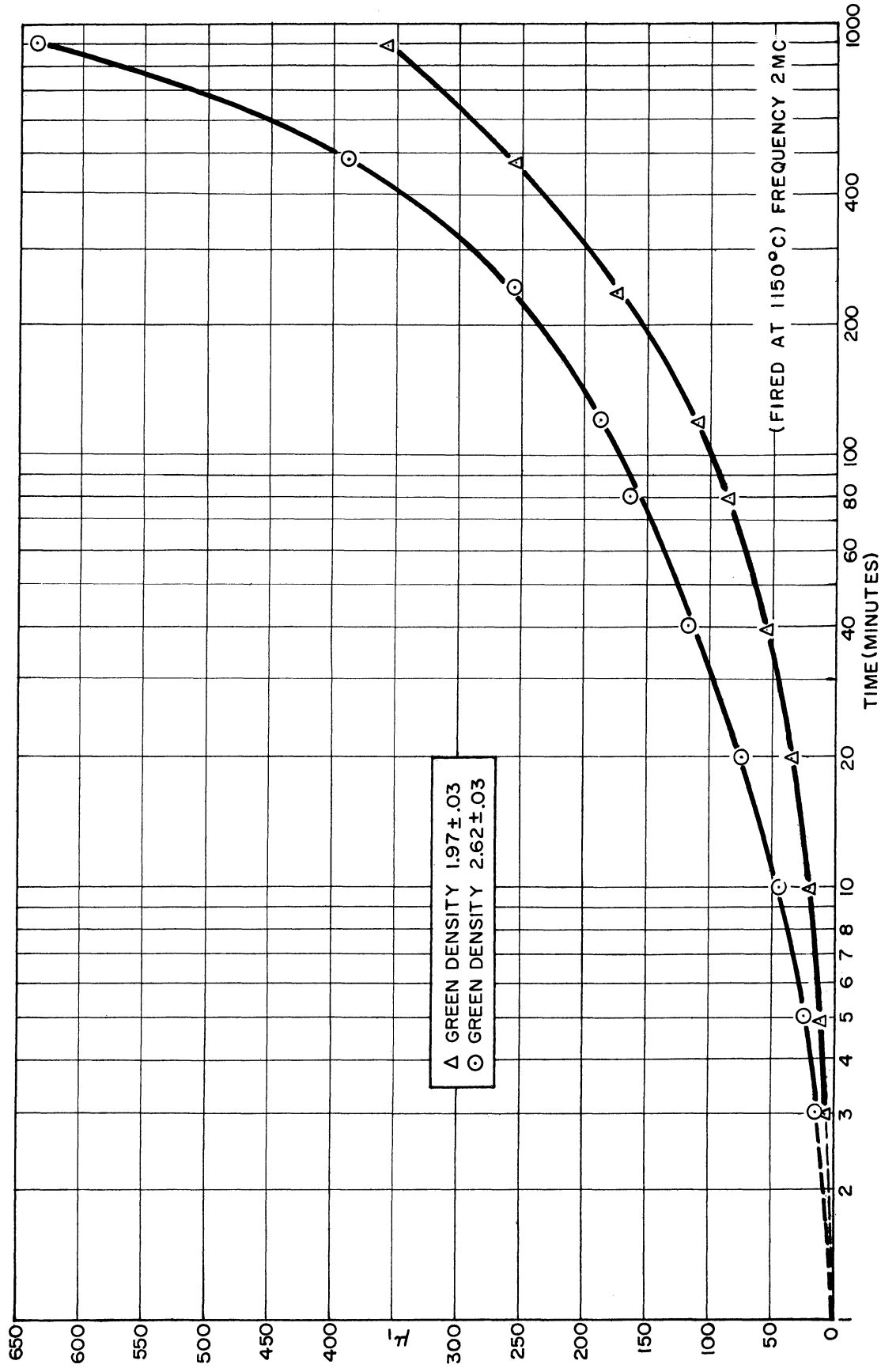

Fig. 38. Effect of green density on the change in μ_1 with firing time for $Ni_{.4}Zn_{.6}Fe_2O_4$.

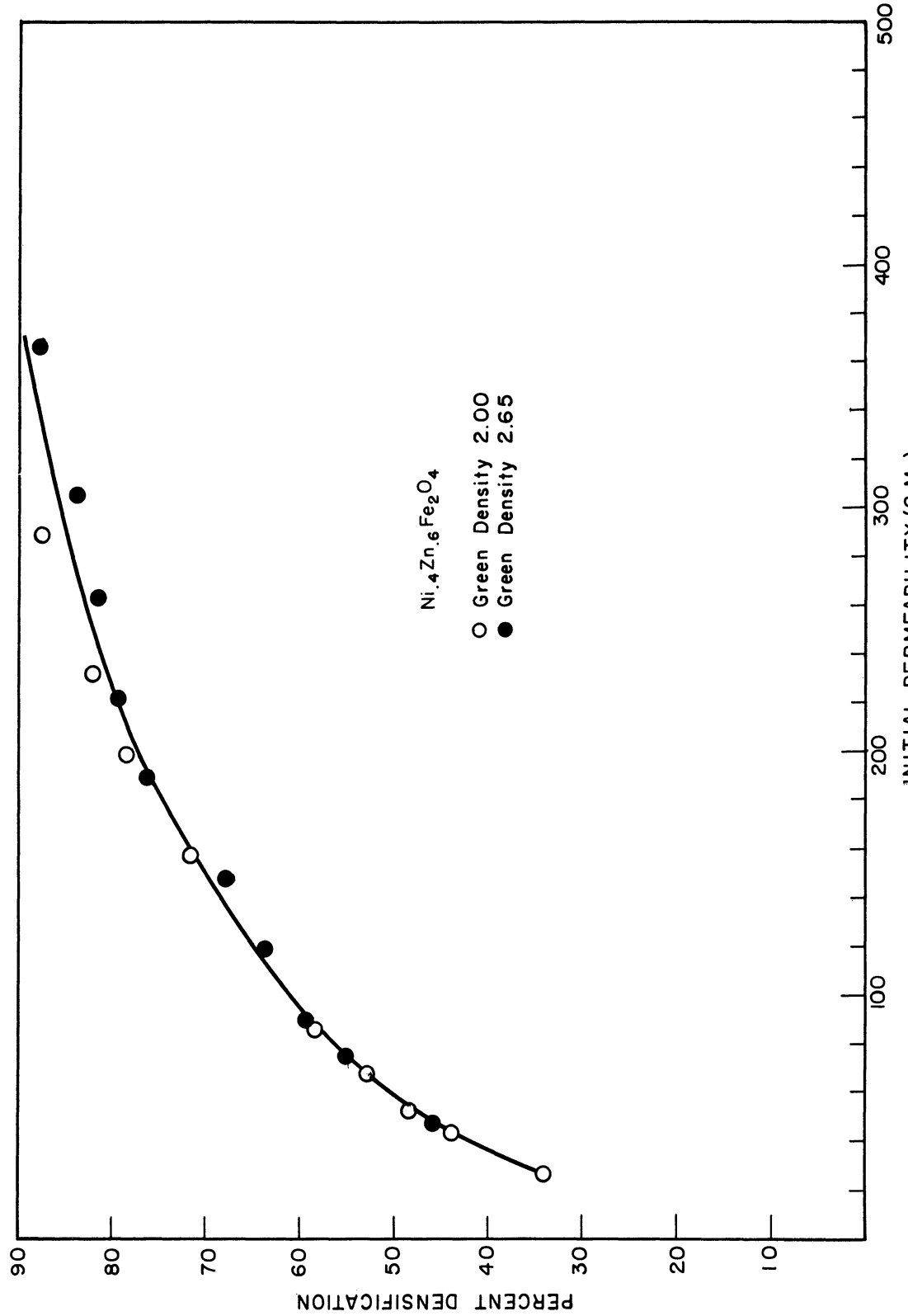

Fig. 39. Percent densification vs. initial permeability; reaction temperature 1150°C.

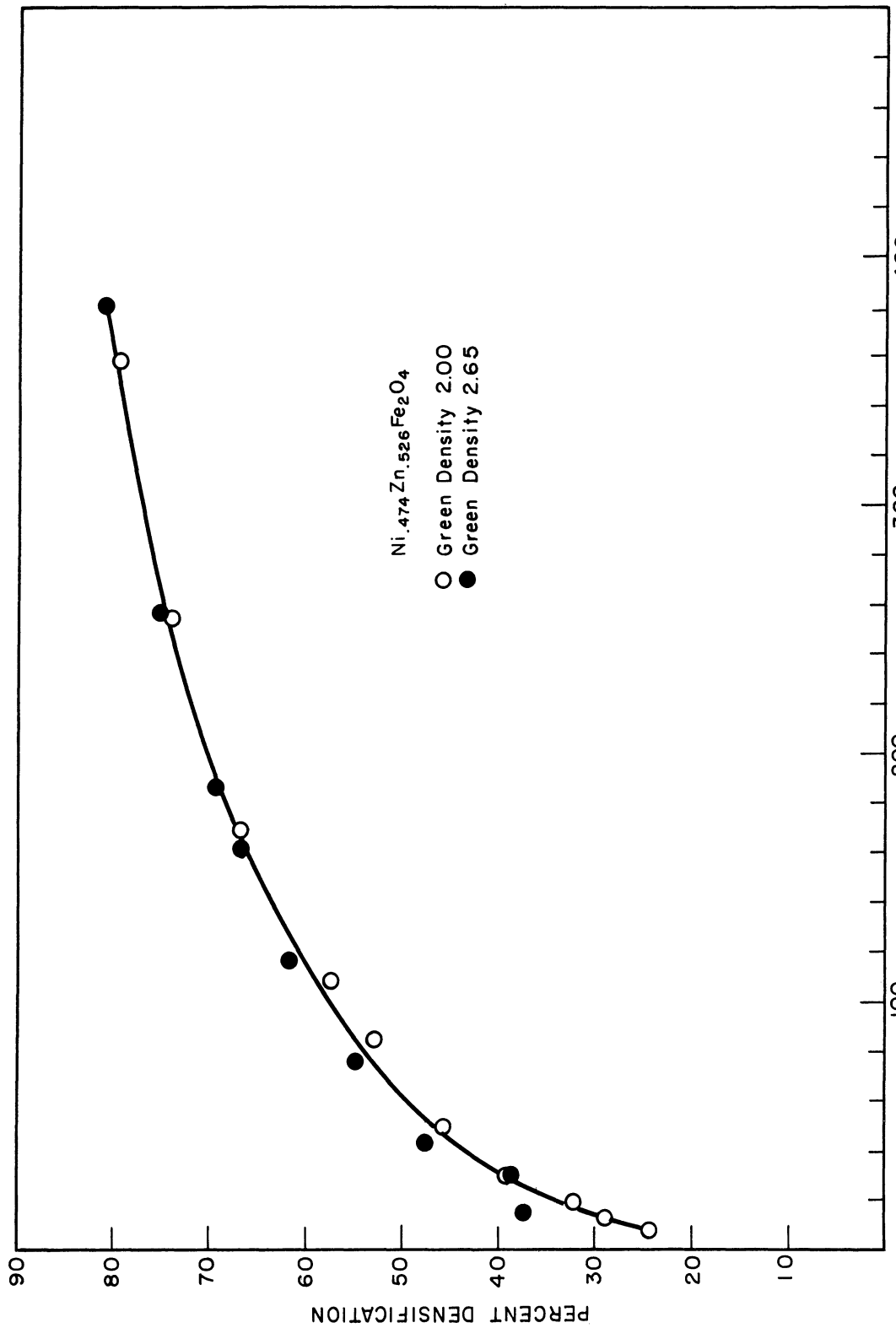

Fig. 40. Percent densification vs. initial permeability; reaction temperature 1210°C.

rather than to the final density of the samples. This indicates that only that increase in density obtained by sintering serves to increase the permeability.

3.5 THE OXIDATION OF THE SYSTEMS $Ni_{.474}Zn_{.526}Fe_2O_4$-$Fe_3O_4$ AND $LiFe_5O_8$-Fe_3O_4

3.5.1 Introductory Remarks.—It has been recognized for some time that two iron sesquioxides exist. Hematite or αFe_2O_3 is the hexagonal form of the oxide. Except for a small parasitic ferromagnetism, it is antiferromagnetic below 680°C, and above this temperature it is paramagnetic. Gamma ferric oxide, ferromagnetic ferric oxide or maghemite is the cubic form of the sesquioxide. It is ferromagnetic below its Curie temperature. The Curie temperature has never been determined with exactness because γFe_2O_3 transforms to αFe_2O_3 before its Curie temperature is reached.

Gamma ferric oxide has been known since 1859 when Robbins[42] first discovered it. The structure of gamma ferric oxide which is now generally accepted was proposed by Hagg[43] and by Verwey.[44] It is a defect structure which contains in its unit cell $Fe_8^{+3}[Fe_{13\frac{1}{3}}^{+3}\square_{2\frac{2}{3}}]O_{32}$. It is similar to magnetite, which has as its unit cell $Fe_8^{+3}[Fe_8^{+2}Fe_8^{+3}]O_{32}$, with the exception that the ferrous iron has been replaced with holes in the lattice and electroneutrality maintained by increasing the amount of trivalent iron. The defects or holes have been found to be ordered on the B sites.[45] This ordering gives rise to lines in the X-ray pattern that are absent in Fe_3O_4, but aside from this and a small change in the lattice constant, the X-ray patterns for γFe_2O_3 and magnetite are the same.

The usual method of preparing γFe_2O_3 is by the low-temperature oxidation of synthetic magnetite or by the dehydration of a gamma hydrate, $\gamma FeOOH$, known as lepidocrocite. A rather detailed account of methods of preparation is given by Wagenkneckt.[46] Sachse and Haase[47] found that the

gamma oxide was unstable at room temperature, transforming over a period of years to αFe_2O_3. It has been established that impurities such as Na, Al, and H_2O stabilize the γFe_2O_3 structure.[48] DeBoer and Selwood[49] investigated the kinetics of the transformation γFe_2O_3-αFe_2O_3 as a function of the stabilizing impurity.

Nicholls[50] and others have proposed that γFe_2O_3 is actually the high-temperature form of the oxide. Magnetite itself exists with a defect structure. Depending on the temperature and the oxygen pressure at which it is prepared, it can be considered to consist of $Fe_8^{+3}[Fe_8^{+2}Fe_8^{+3}]O_{32}$ at the one limit and $Fe_8^{+3}[Fe_{13}^{+3}\frac{1}{3}\ \square_2\frac{2}{3}]O_{32}$ at the other. In air at one-atmosphere pressure Darken and Gurry[18] found that the composition of magnetite is $7Fe_3O_4 \cdot 3Fe_2O_3$ at 1392°C. It appears that at very high oxygen pressures the composition would approach that of γFe_2O_3.

It is generally supposed that γFe_2O_3 is a monotropic phase. There are, however, references in the literature that indicate that the transformation γFe_2O_3 to αFe_2O_3 is reversible. Wagenkneckt[46] states that the reaction αFe_2O_3 + pressure → γFe_2O_3 occurs in nature. Kojima[51] studied the transformations in iron oxides by following the magnetic remanence and coercive force as functions of temperature in various atmospheres. He concluded that γFe_2O_3 was an intermediate product in both the oxidation of magnetite to αFe_2O_3 as well as in the reduction of αFe_2O_3 to magnetite. Finch and Sinha[29] also found that the transformation $\gamma Fe_2O_3 \rightarrow \alpha Fe_2O_3$ is reversible.

It is now a generally accepted fact that synthetic magnetite prepared from solution by the co-precipitation of ferrous and ferric hydroxides is transformed to αFe_2O_3 in two stages. Welo and Baudisch[52] found that the reaction $Fe_3O_4 + O_2 \xrightarrow{220°C} \gamma Fe_2O_3$ was the first stage in the oxidation of

synthetic magnetite. They found that the transformation $\gamma Fe_2O_3 \rightarrow \alpha Fe_2O_3$ occurs at higher temperatures. These findings have been confirmed by others. The question whether natural magnetite, which differs from the synthetic product in the amount of water it contains and the particle size, oxidizes directly to αFe_2O_3, or also goes through the γFe_2O_3 stage, has remained controversial.

David and Welch[21] investigated the oxidation of magnetite prepared by the reduction of αFe_2O_3 and by precipitation of ferrous and ferric hydroxide from basic solutions. Only the magnetite prepared by precipitation from solution showed the formation of γFe_2O_3 on oxidation. These authors conclude that γFe_2O_3 is stable only if water is present in the lattice. A similar conclusion was arrived at by deBoer and Houben[53] with regard to the stability of γAl_2O_3, a compound isomorphous with γFe_2O_3.

The oxidation of magnetite has been investigated by differential thermal analysis by several investigators. Magnetite shows two characteristic exothermic peaks in a differential thermal analysis curve. The first peak occurs at around 300°C, while the second broader peak occurs at around 900°C. Both the amplitude and the temperature at which these peaks occur are changed by the particle size of the magnetite. Kulp and Trite[54] concluded that synthetic magnetite, prepared by the reduction of αFe_2O_3 at low temperatures, was transformed to γFe_2O_3 on oxidation, and they attributed the first peak in the differential thermal analysis curve to this transformation. They attributed a somewhat similar peak in the differential thermal analysis curve of natural magnetite to recrystallization of the magnetite, with no formation of γFe_2O_3. This conclusion was based on the fact that the amplitude of the peak was proportional to the particle size of the magnetite, and on the fact that the material heated beyond the

temperature of the first peak contained a considerable amount of ferrous iron. Schmidt and Vermaas[55] concluded that the first peak in natural magnetite was due to surface oxidation, and that the second peak was due to the oxidation of the interior instigated by recrystallization of the protective surface layer of αFe_2O_3. They agreed with Kulp and Trite that no γFe_2O_3 was formed during the oxidation of natural magnetite. Lepp[56] concluded that natural magnetite was oxidized to γFe_2O_3 up to approximately 375°C, at which temperature the gamma oxide transformed to the alpha oxide. He also concluded that, at around 500°C, magnetite oxidized directly to αFe_2O_3.

This section of the discussion reports the results of studies on the oxidation of the solid solution series $Ni_{.474}Zn_{.526}Fe_2O_4$-$Fe_3O_4$ and $LiFe_5O_8$-Fe_3O_4. This study was made to determine the influence of $(Ni_{.474}Zn_{.526})O$ and Li_2O on the stabilization of γFe_2O_3 formed during the process of oxidation. $(Ni_{.474}Zn_{.526})O$ was selected because of the wide application of the ferrite, $Ni_{.474}Zn_{.526}Fe_2O_4$, in electronic devices. Lithium oxide was selected because of the close structural resemblance between $LiFe_5O_8$ and γFe_2O_3.

3.5.2 Preparation and Measurement of Samples.—The samples used in this study were the same as those prepared for the phase studies. The initial compositions are given in Tables I and VI for the $Ni_{.474}Zn_{.526}Fe_2O_4$-$Fe_3O_4$ and $LiFe_5O_8$-Fe_3O_4 series, respectively. Compositions 1 through 10 were used for the $Ni_{.474}Zn_{.526}Fe_2O_4$-$Fe_3O_4$ series, while Compositions 8 through 20 were used for the $LiFe_5O_8$-Fe_3O_4 series. The samples were prepared at a temperature which insured that homogeneous single phases of the solid solutions were obtained. All samples were quenched in water.

Differential thermal curves of all samples were obtained after crush-

ing the material in an agate mortar and sieving through a 325-mesh screen. Samples of Compositions 18 and 20 were prepared with a smaller particle size by ball-milling the samples in acetone. The particle size of these samples was estimated, by microscopic examination, to be approximately 1 micron. These samples are designated throughout the discussion as Compositions 18' and 20' to distinguish them from samples with larger particles of the same composition. Differential thermal analysis curves were obtained with a unit built according to the Department of Agriculture design. A platinum vs. platinum - 10% rhodium thermocouple was used for the differential thermocouple, while a chromel-alumel thermocouple was used to determine the temperature of the nickel block. The latter thermocouple was calibrated against the inversion temperature of quartz, using the procedure given by Faust.[57] The heating rate was 12°/min.

Measurements of the saturation moment and the percent of oxidation were made on Compositions 18' and 20'. The measurements were made after heating the samples for 15 minutes at temperature intervals of 25°C. The percent oxidation of Composition 20, which had been sieved through a 325-mesh sieve, was determined after heating for 15 minutes at temperature intervals of 50°C.

The saturation-moment measurements were made with the equipment shown in Fig. 23. The percent oxidation was determined by following the change in weight and by ferrous iron analysis. To eliminate the error in the saturation-moment measurement introduced in weighing the sample, the tube containing the sample for the measurement was heated with a second sample in a porcelain crucible. From the latter sample, the weight change was determined and ferrous iron determinations were made. This made it possible to make all magnetic moment measurements on the same sample. Moment

measurements of the sample in the crucible, at various intervals during the course of oxidation, showed that the extent of oxidation of this sample was identical with that of the sample in the tube.

3.5.3 Results.—The differential thermal curves are shown in Fig. 41 and Figs. 42 and 43 for the $Ni_{.474}Zn_{.526}Fe_2O_4$-$Fe_3O_4$ and $LiFe_5O_8$-Fe_3O_4 series, respectively. The numbers on the curves correspond to the numbers assigned to the initial compositions given in Tables I and VI, with the exception of Curve 21 of Fig. 43, which is the differential thermal analysis curve obtained from a sample of natural magnetite ore. This material will be referred to as natural magnetite, while the material prepared by heating Fe_2O_3 above 1390°C in air and quenching to room temperature will be referred to as synthetic magnetite. This synthetic magnetite should not be confused with the synthetic magnetite referred to in the literature, which is prepared by co-precipitation of ferrous and ferric hydroxides from solution. The sensitivity of the differential thermocouple for curves in Fig. 41 is 2.89 μv/cm, while that for Figs. 42 and 43 is 9.96 μv/cm. There is a slight exothermic peak at 360°C in both curves which marks the Curie temperature of the nickel block that held the sample.

Curve 1 of Fig. 41 has a broad exothermic peak. This is due to the oxidation of some ferrous iron formed in the stoichiometric ferrite. As the magnetite content is increased in Curves 2 to 10, this peak becomes less broad and moves down in temperature and coincides with the low-temperature peak in Curve 10, which is the curve for synthetic magnetite. In Curve 4, a second exothermic peak makes its appearance at about 725°C. This peak moves down in temperature with increasing magnetite content and decreases in amplitude until it has disappeared in Curve 10. A third exothermic peak makes its appearance in Curve 6 at about 775°C. (The second

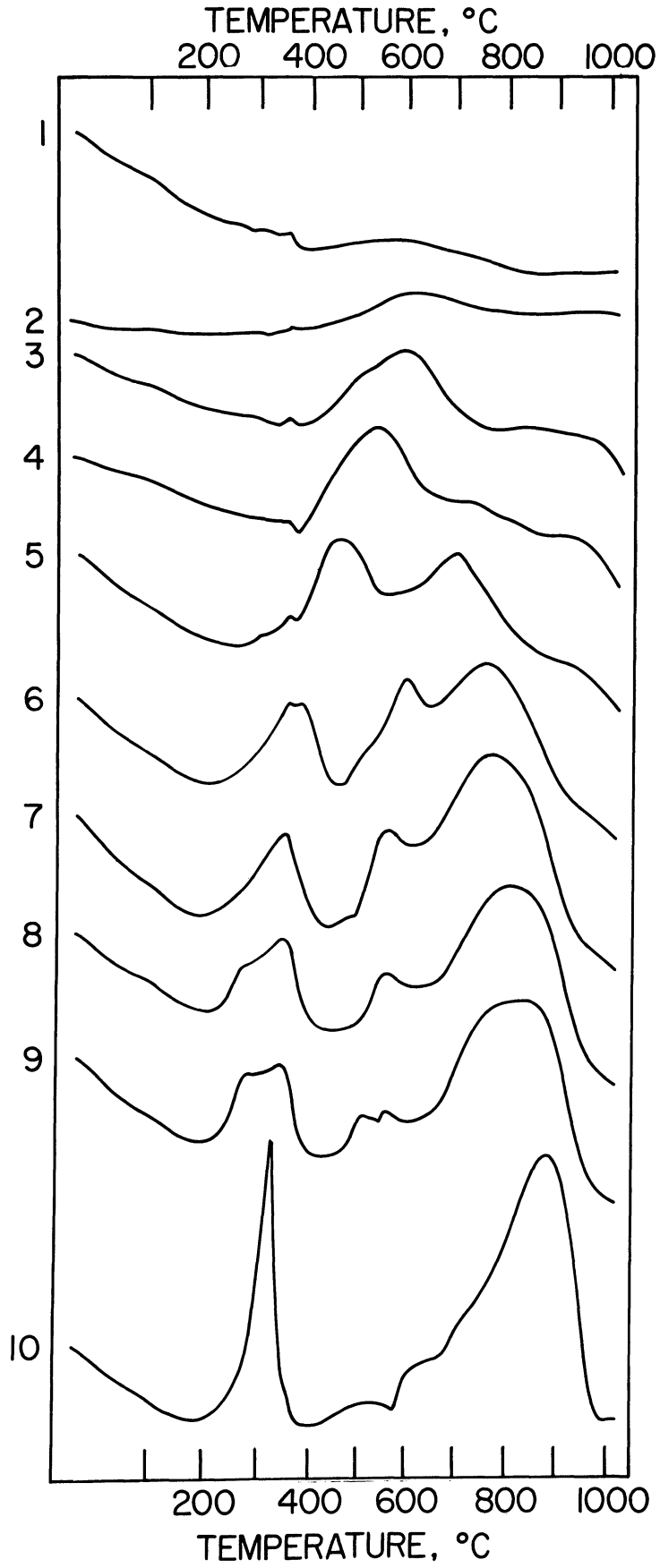

Fig. 41. Differential thermal analysis curves for the solid solution series $Ni_{.474}Zn_{.526}Fe_2O_4$-$Fe_3O_4$.

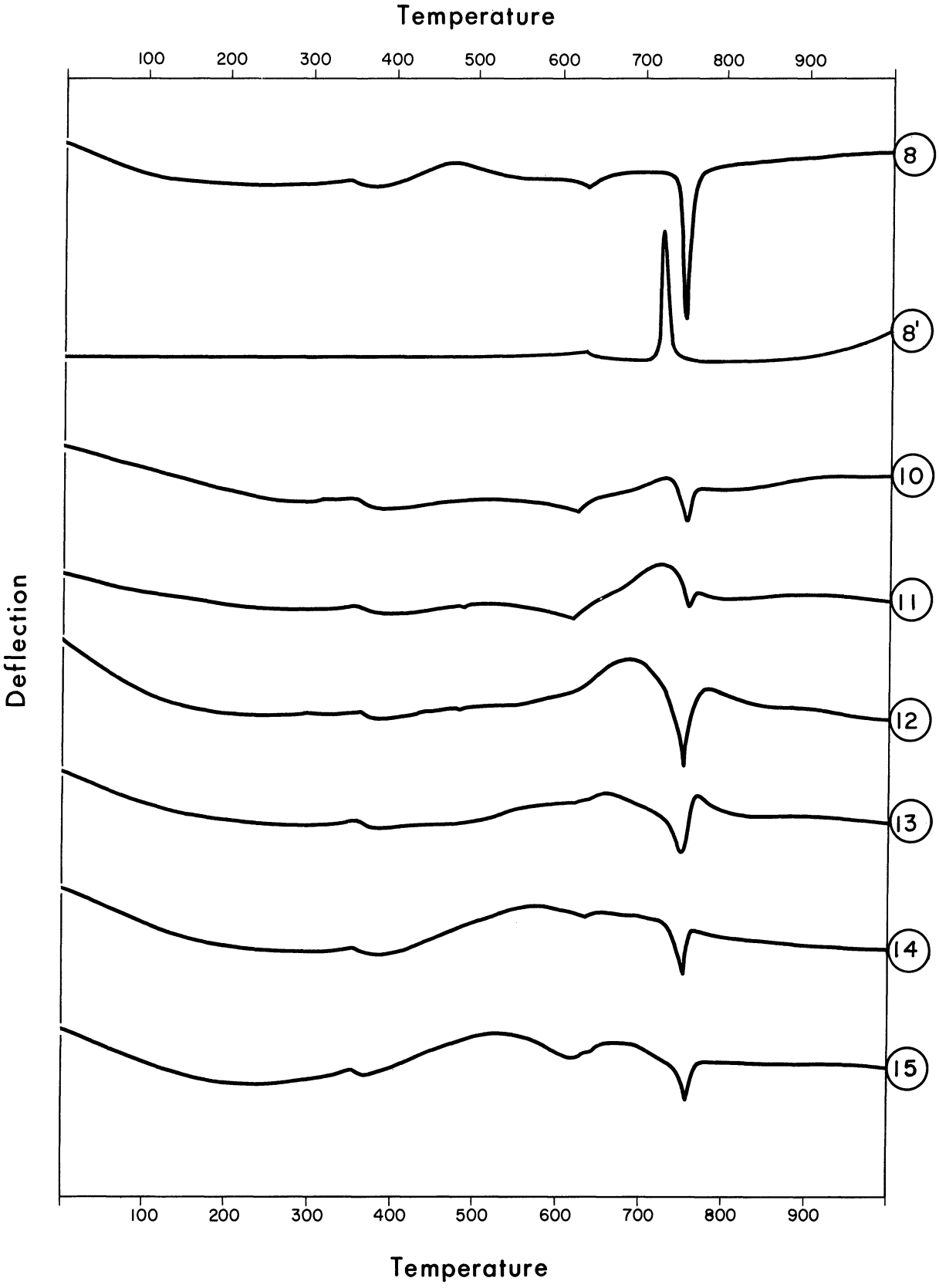

Fig. 42. Differential thermal analysis curves for the solid solution series $LiFe_5O_8$-Fe_3O_4.

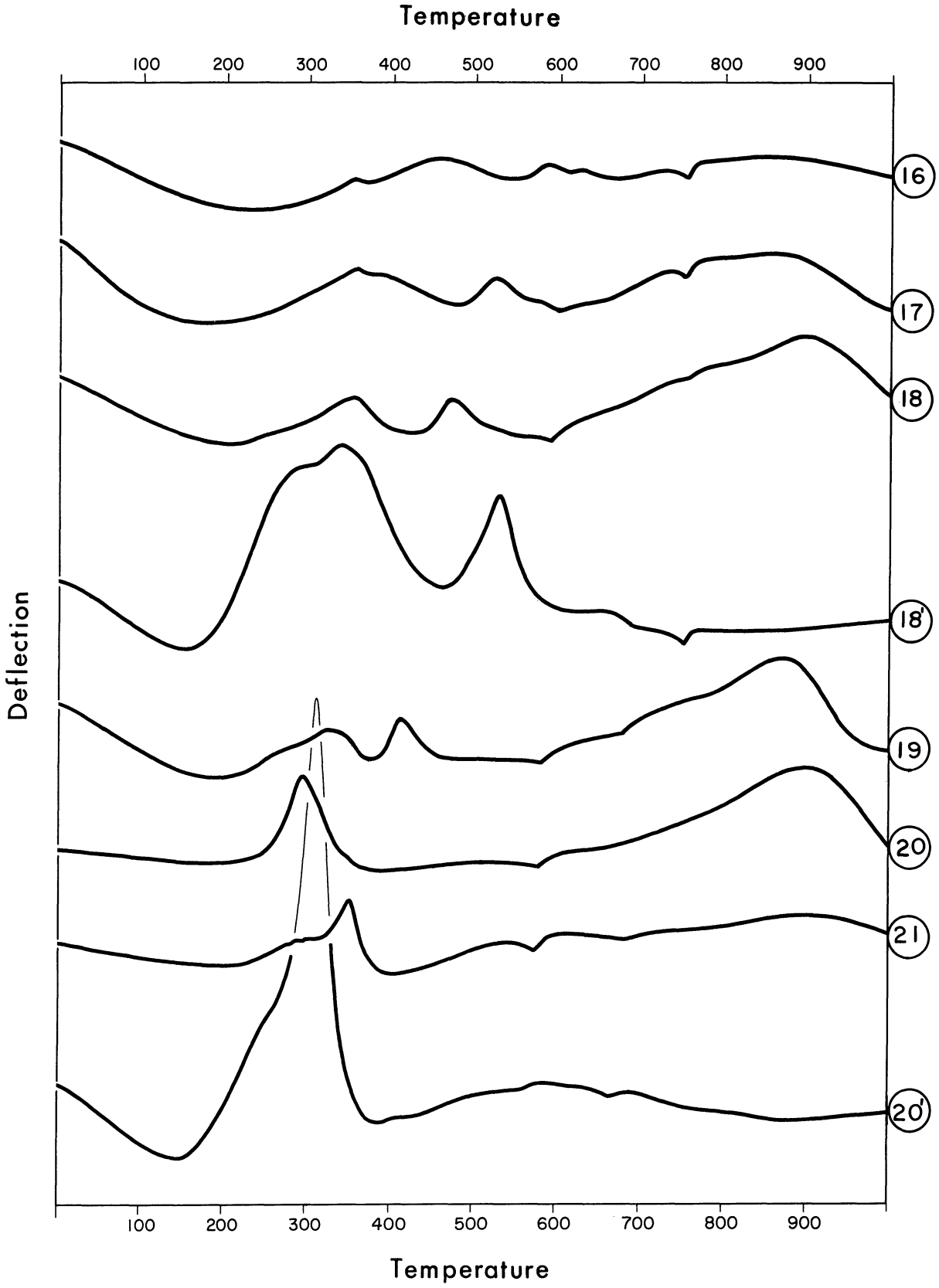

Fig. 43. Differential thermal analysis curves for the solid solution series $LiFe_5O_8$-Fe_3O_4.

peak in Curve 5 might well be a summation of two superimposed peaks.) This third peak moves up in temperature with increasing magnetite content and corresponds with the high-temperature peak in the curve for magnetite.

In Fig. 42, Curve 8 is the heating curve for $LiFe_5O_8$. Curve 8' is the cooling curve for the same sample. The dip at 634°C corresponds to the Curie temperature of $LiFe_5O_8$. $LiFe_5O_8$ undergoes a disorder transformation at 755°C and this gives rise to the endothermic transition at this temperature. This transition was first observed by Braun[20] and has been attributed to an ordering of the lithium ions on the A and B sites. The cooling curve shows that the transition is reversible. This is in agreement with Braun, who gives a temperature of 755°C for the disordering process on heating and a temperature of 735°C for the ordering process on cooling. As in the Ni-Zn ferrite series, an exothermic peak appears as the magnetite content is increased. This peak moves down in temperature as the composition approaches that of magnetite. This peak appears in Curve 10 of Fig. 42 just before the disorder transformation occurs. Up to and including Curve 15, the oxidation appears to be complete below the temperature of the disorder transformation. In Curve 16 there is evidence of oxidation taking place above this temperature. A third peak also makes its appearance at this composition. As the magnetite content is increased further, the position of this intermediate peak moves down in temperature, while the high-temperature peak moves to correspond with the high-temperature peak of pure Fe_3O_4.

To identify the origin of the exothermic peaks in magnetite, the oxidation of magnetite was followed by determining the change in weight and the change in ferrous iron content by chemical analysis of a sample heated in air for 15 minutes at 50°C intervals. Figure 44 shows the results of

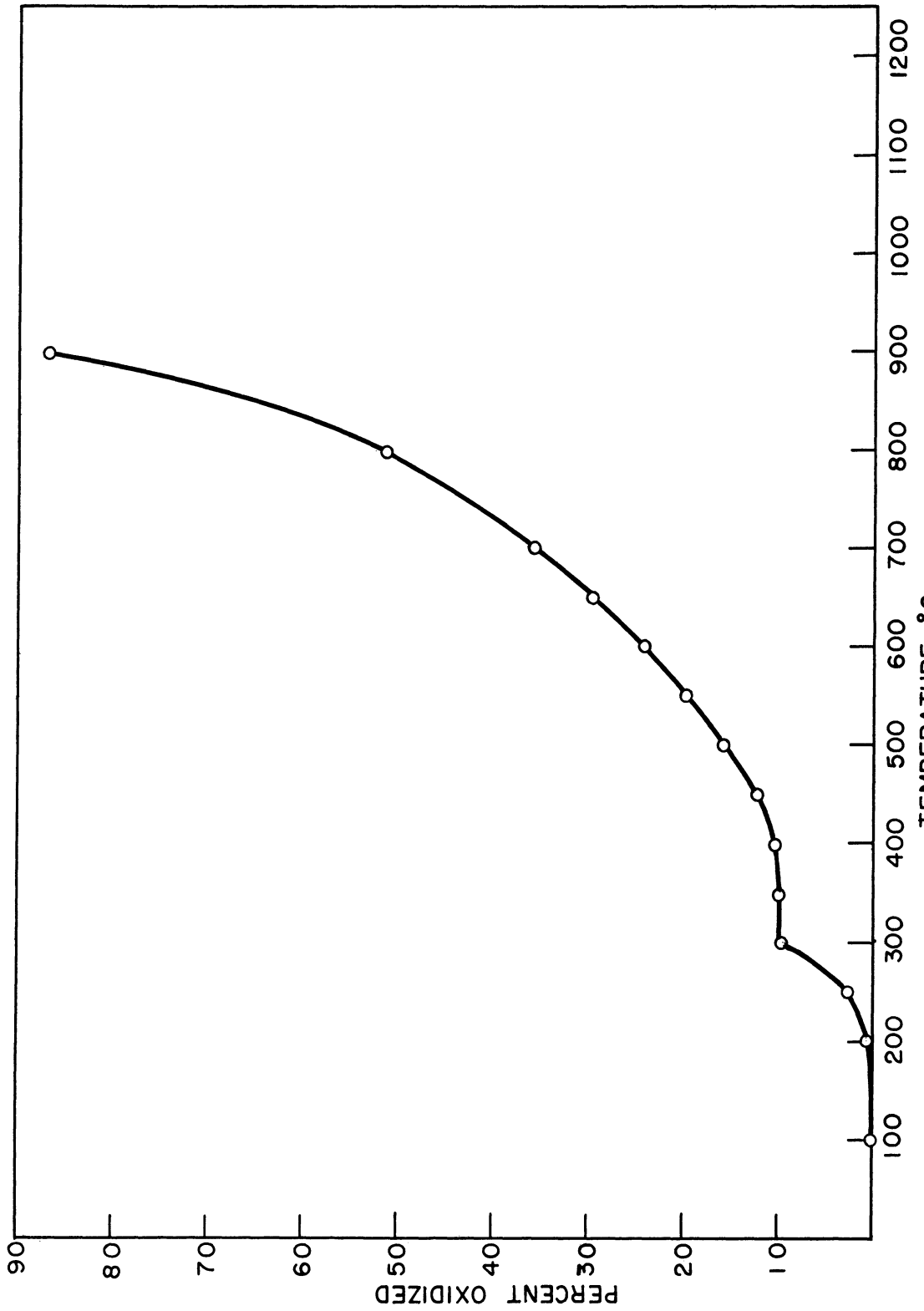

Fig. 44. Percent oxidation vs. heating temperature for magnetite; heating time 15 minutes.

this investigation. There is a break in the oxidation curve at 300°C. The change in the rate of oxidation at this temperature explains the low-temperature exothermic peak in the differential thermal curve of magnetite. It is concluded that this peak is caused at least in part by the surface oxidation of Fe_2O_3 as proposed by Schmidt and Vermaas. These authors, however, found that the oxidation was accelerated at 580°C, the Curie temperature of Fe_3O_4. Figure 44 shows no indication that this is the case. It appears that the second peak is not due to any sudden initiation of oxidation, but rather makes its appearance when the continuously increasing rate of oxidation becomes sufficiently rapid.

The saturation moment and the percent of oxidation of Compositions 18' and 20' are plotted as a function of the heating temperature in Fig. 45. The oxidation curve of Composition 20' has the same break at 300°C as does the oxidation curve of Composition 20 (Fig. 44). The oxidation curve of Composition 18', however, does not have this break. The oxidation of Composition 18' is complete at 700°C, while the oxidation of Composition 20' is complete at 750°C. (Since the data were plotted only to 700°C, this is not shown in Fig. 45.) This contrasts with the oxidation of Composition 20 which is not complete even at 900°. This higher temperature required to oxidize completely the sample with the larger particle size is to be expected.

The saturation moment of Composition 18' decreases slowly to 400°C. At this temperature there is a drop in the moment which levels off at around 500°C. As the heating temperature is raised, the moment continues to decrease slowly until the moment of the completely oxidized sample is reached. (The composition of the oxidized sample is $8.34LiFe_5O_8 + 750Fe_2O_3$.) The saturation moment of Composition 20' decreases slowly until the temper-

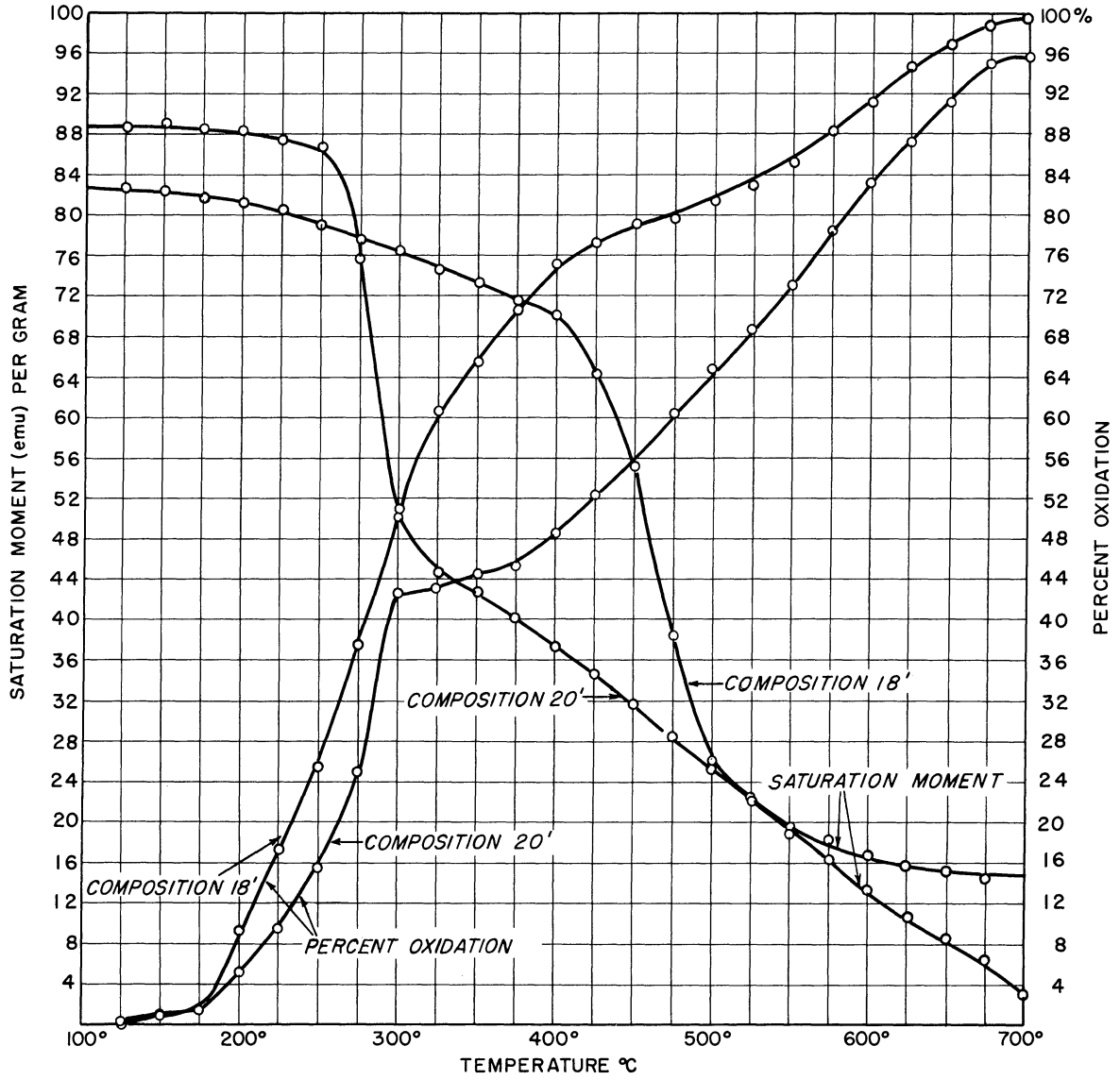

Fig. 45. Saturation moment per gram and percent oxidation vs. heating temperature; heating time 15 minutes.

ature of 250°C is reached. At this temperature there is a sharp drop, after which the moment decreases more slowly.

In Fig. 46 the saturation moment of both compositions is plotted as a function of the percent of oxidation. The interesting feature of this curve is that in the initial stages of oxidation, the curves for both compositions are similar. This indicates that γFe_2O_3 is formed in the early stages of the oxidation of magnetite. Extrapolation of the data in this region to 100% oxidation indicates that the saturation moment of γFe_2O_3 at room temperature is about 70 emu.

When 50% of Composition 20' has been oxidized, the moment is not 50% of the initial value, but somewhat below this. This would not be the case if only the oxidation of the sample were contributing to the decrease in the moment. The composition of the sample was found by chemical analysis to be $.825Fe_3O_4 \cdot .175Fe_2O_3$. Thus some Fe_2O_3 was in solid solution as γFe_2O_3 in the sample. This appears to have been converted to αFe_2O_3 between 300° and 375°C when 42 to 45% of the oxidation was complete. This caused the moment to drop without oxidation taking place.

The saturation moment of Composition 20' in Fig. 46 appears to be approaching a value of about 4 emu until the oxidation is about 95% complete, at which time it drops to zero at 100% oxidation. (There is actually a small moment at 100% oxidation, due to the parasitic ferromagnetism of αFe_2O_3.) It is interesting to observe that this drop occurs between 675° and 700°C, and that the Curie temperature of αFe_2O_3 is 680°C. The cause of this behavior is not known.

It is interesting to compare the temperature of the transformation $\gamma Fe_2O_3 \rightarrow \alpha Fe_2O_3$ obtained by differential thermal analysis with that obtained by heating the sample at 25°C intervals for 15 minutes. In the

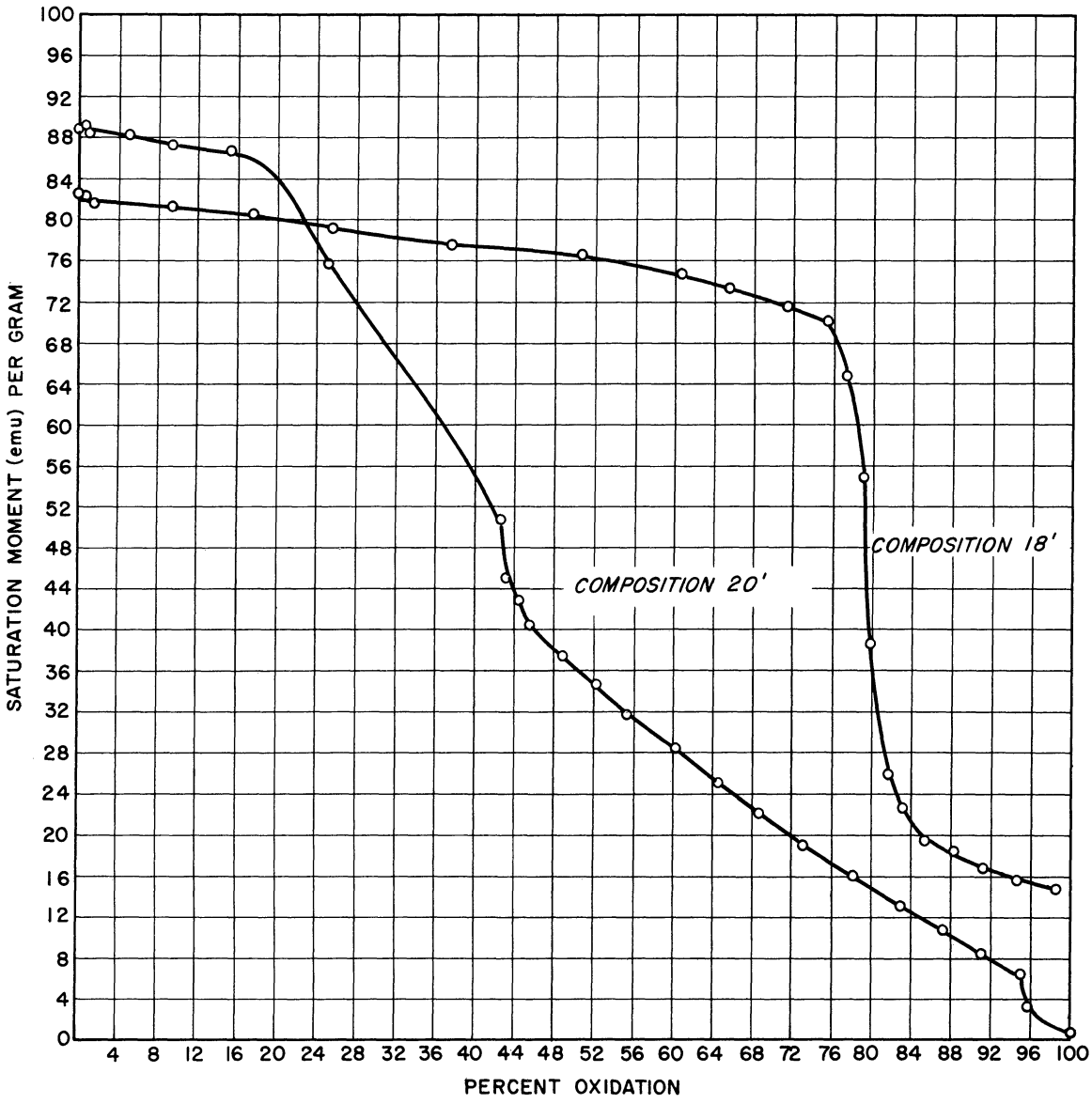

Fig. 46. Saturation moment per gram vs. percent oxidation.

first case, the transformation is indicated by an exothermic peak; in the second case, the transformation is indicated by a sharp drop in the saturation moment. It is to be expected that a transformation which occurs over a temperature interval will not occur at the same temperature in both cases, since a different time factor is involved.

Curve 18' of Fig. 43 indicates that the transformation $\gamma Fe_2O_3 \rightarrow \alpha Fe_2O_3$ begins at around 470°C and terminates at around 560°C with the peak maximum at around 530°C. The saturation moment measurements of the same sample indicate that the transformation starts at around 400°C and terminates at around 500°C. It is difficult to determine the temperature at which the transformation $\gamma Fe_2O_3 \rightarrow \alpha Fe_2O_3$ occurs in Composition 20' from the differential thermal analysis curve (Curve 20', Fig. 43). The exothermic peak which occurs at around 300°C is the composite of two peaks superimposed on each other. One peak is caused by surface oxidation, while the other is caused by the transformation $\gamma Fe_2O_3 \rightarrow \alpha Fe_2O_3$. The saturation-moment measurements of Composition 20', Fig. 45, indicate that the transformation starts at around 250°C and terminates at 300°C.

In Fig. 47 the temperature at which the peak in the differential thermal analysis curve, arising from the $\gamma Fe_2O_3 \rightarrow \alpha Fe_2O_3$ transformation, is at a maximum has been plotted against the composition of the material. It can be seen that $Ni_{.474}Zn_{.526}Fe_2O_4$ and $LiFe_5O_8$ are about equal in their ability to stabilize γFe_2O_3. It appears that it is the concentration of the impurity, i.e., lithium and nickel + zinc, that determines the extent of stabilization of γFe_2O_3. If it were the ferrite concentration, the comparison would be between the mole percent $Ni_{.474}Zn_{.526}Fe_2O_4$ and $(LiFe)_{1/2}Fe_2O_4$. That is, $Ni_{.474}Zn_{.526}Fe_2O_4$, which has one gram atomic weight of (Ni + Zn) per mole of ferrite, is twice as effective as the corresponding lithium

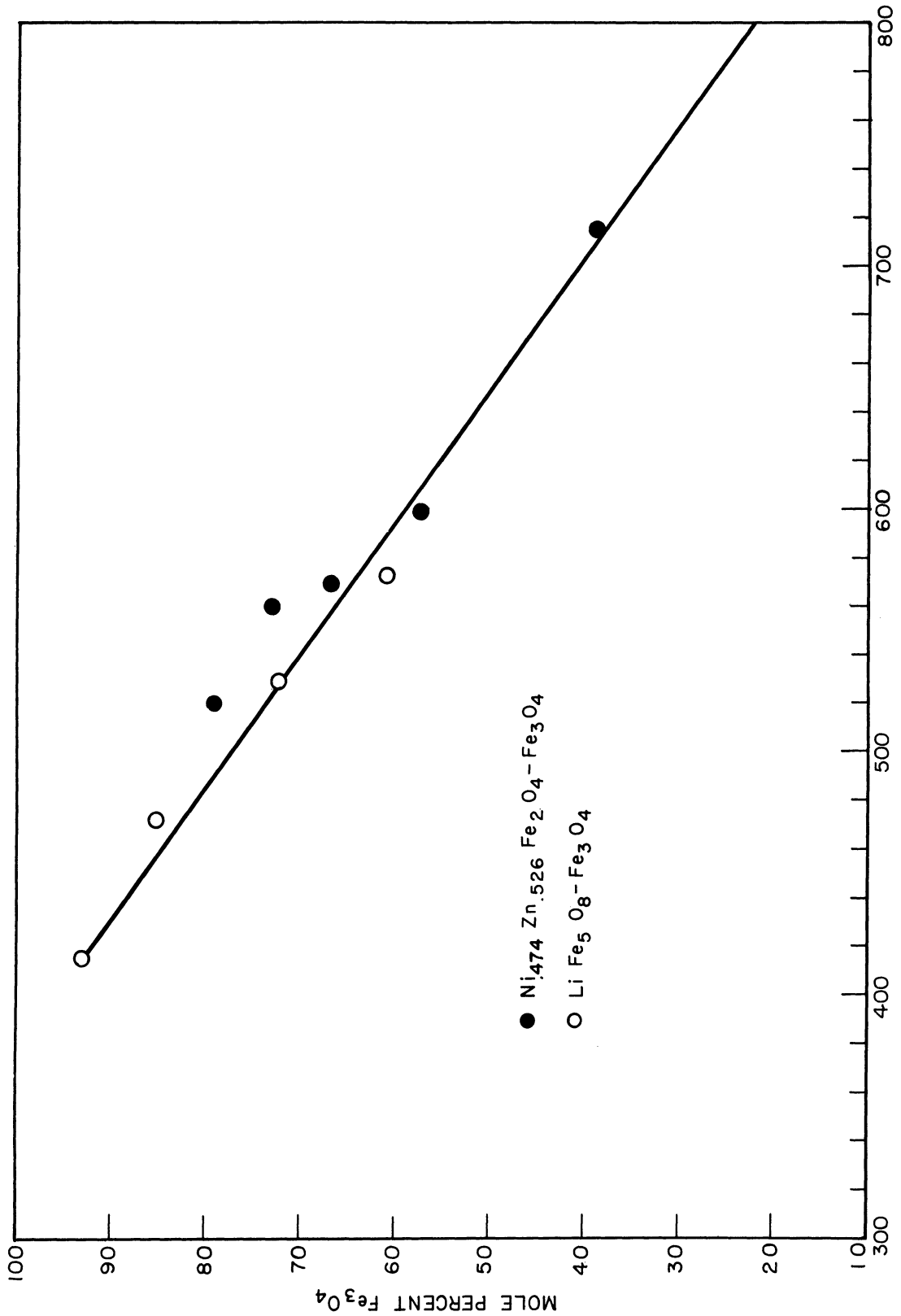

Fig. 47. Temperature of the γFe_2O_3-αFe_2O_3 transformation as a function of composition.

ferrite, $(LiFe)_{1/2}Fe_2O_4$, which has only 1/2 gram atomic weight of Li per mole of ferrite. Extrapolation shows that the $\gamma Fe_2O_3 \rightarrow \alpha Fe_2O_3$ transformation should occur at around 375°C with Fe_3O_4. This is at least 75°C higher than the temperature actually found. A comparison of the Curves 18 and 18' in Fig. 43 shows that the $\gamma Fe_2O_3 \rightarrow \alpha Fe_2O_3$ transformation is about 70°C higher in Curve 18'. This indicates that particle size as well as composition plays a role in determining the temperature to which γFe_2O_3 is stabilized.

The low-temperature peaks of both series at the Fe_3O_4-rich end of the series show a double peak. The exact cause of this has not been extablished. It can be observed that in natural magnetite (Fig. 43, Curve 21) a similar situation occurs, while in synthetic magnetite (Fig. 43, Curve 20) it does not. The difference in the purity of the samples might account for the difference in the differential thermal analysis curves of natural and synthetic magnetite.

3.5.4 Conclusions.—The investigation of the oxidation of the solid solution series $Ni_{.474}Zn_{.526}Fe_2O_4$-$Fe_3O_4$ and $LiFe_5O_8$-Fe_3O_4 has shown that the presence of $Ni_{.474}Zn_{.526}Fe_2O_4$ or $LiFe_5O_8$ in solid solution with magnetite stabilizes γFe_2O_3 formed during the oxidation process. The temperature to which γFe_2O_3 is stabilized depends upon the concentration of the stabilizing component. The two ferrites are equal in their ability to stabilize γFe_2O_3. This means that it is the number of stabilizing atoms, rather than the charge of the atoms, that is significant in promoting stabilization. The temperature to which γFe_2O_3 is stable also depends upon the particle size of the sample.

Magnetite oxidizes in two stages. The extent of oxidation occurring during the first stage, which begins at around 150°C and terminates at

around 300°C depends on the particle size. During the initial period of this stage, magnetite oxidizes to γFe_2O_3. The second stage of the oxidation, which starts where the first terminates, proceeds to completion at a temperature that again depends on the particle size. The defect structure of magnetite prepared in air at 1400°C, resulting from the solubility of γFe_2O_3 in magnetite, disappears on heating between 300 and 350°C.

The above conclusions made concerning the oxidation of magnetite are in close agreement with those of Lepp.[56] It is understandable why the controversy concerning formation of γFe_2O_3 during the oxidation of magnetite has occurred. The dependence of the stability of γFe_2O_3 formed during oxidation on the particle size, the impurities, and the heating procedure make the results greatly dependent on the method of investigation.

4. SUMMARY

The phase diagrams for the systems $Ni_{.474}Zn_{.526}Fe_2O_4$-FeO-$Fe_2O_3$ and $LiFeO_2$-FeO-Fe_2O_3 in air at one atmosphere are given. The composition of magnetite in solid solution with $Ni_{.474}Zn_{.526}Fe_2O_4$ and with $LiFe_5O_8$ in the ferrite-hematite field is $7Fe_3O_4 \cdot 3Fe_2O_3$. The stoichiometric lithium ferrite, $LiFe_5O_8$, decomposes at around 1000°C with the formation of $LiFeO_2 \cdot xFeO$ and $LiFe_5O_8 \cdot xFe_3O_4$.

A microscopic study of the reaction between NiO and Fe_2O_3 shows that both oxides take part in the diffusion process. The diffusion of NiO into Fe_2O_3 results in the formation of a ferrite phase at the surface of the Fe_2O_3 particles. At the same time, Fe_2O_3 diffuses into NiO and forms a NiO-Fe_2O_3 solid solution. As the concentration of Fe_2O_3 increases, a ferrite phase precipitates out. A study of the reaction between ZnO and Fe_2O_3 shows that the ferrite reaction takes place on the Fe_2O_3 particles. No evidence of diffusion of Fe_2O_3 into ZnO or of ferrite formation on the ZnO surface was observed.

The kinetics of the reaction between NiO and Fe_2O_3 and between Li_2CO_3 and Fe_2O_3 were investigated in air, oxygen, and nitrogen atmospheres. The data for the reaction between NiO and Fe_2O_3 in a nitrogen atmosphere fit Jander's equation better than the data for the same reaction in air and oxygen atmospheres. The rate of reaction in a nitrogen atmosphere is greater than it is in air or oxygen atmospheres. The rate of reaction in an air atmosphere is slightly greater than it is in an oxygen atmosphere. The data for the reaction between Li_2CO_3 and Fe_2O_3 in air and oxygen atmospheres do not fit Jander's equation. The data for the same reaction

in a nitrogen atmosphere, however, do fit Jander's equation. The rate of reaction in a nitrogen atmosphere is again considerably greater than it is in an air or oxygen atmosphere, and the rate of reaction in an air atmosphere is slightly greater than in an oxygen atmosphere. Since Jander's equation assumes that the rate-determining step is the diffusion of the reacting components through the product layer, it is concluded that this is more nearly the case in a nitrogen atmosphere than it is in an air or oxygen atmosphere. In an air or oxygen atmosphere the reaction at the boundary plays a role in determining the rate of reaction.

The extent of densification of ferrites during sintering at a constant temperature is related to the green density, g, of the compact by the equation $\Delta D = -f_1(T)g + f_2(T)$, where ΔD is the change in density and f_1 and f_2 are functions of the reaction temperature. The permeability is found to be closely correlated with the percent of densification.

The presence of $Ni_{.474}Zn_{.526}Fe_2O_4$ and $LiFe_5O_8$ in solid solution with magnetite stabilizes γFe_2O_3 formed during the oxidation process. The temperature to which γFe_2O_3 is stabilized depends on the concentration of the stabilizing ferrite and the particle size of the sample. $Ni_{.474}Zn_{.526}Fe_2O_4$ and $LiFe_5O_8$ are equal in their stabilizing effect. From measurements of the saturation moment as a function of the percent of oxidation, it is concluded that, in the initial stages of the oxidation of magnetite, γFe_2O_3 is formed.

APPENDIX I

THE PROCEDURE FOR FERROUS IRON ANALYSIS

The procedure used in the analysis of ferrous iron is given here because it is a modification of a procedure found in the literature. The modification was made because of the difficulty encountered in dissolving Ni-Zn ferrites. These ferrites dissolve very slowly in concentrated hydrochloric acid, but when $SnCl_2$ is added, they dissolve rapidly.

The samples are ground in an agate mortar to a fine powder, and about .5 gm of the sample is weighed into a 300-ml Erlenmeyer flask. The flask is fitted with a stopper containing an inlet for the CO_2, and another inlet through which a buret tip can be inserted. The system is flushed with CO_2 which has been bubbled through a chromous chloride solution to remove any oxygen, following a procedure given by Kolthoff and Lingane.[58] With the CO_2 still flowing, exactly 20 ml of a standardized solution of .1 N $SnCl_2$ in concentrated HCl is added from a buret. The opening for the buret is then attached to a line containing a gas trap to insure a one-way flow of gas, and the CO_2 flow rate is reduced. The flask is heated in a water bath until the ferrite is dissolved. This usually requires about 15 to 20 minutes. The flask is then cooled, the flow of CO_2 being adjusted so that no water from the trap is taken into the flask. The ferrous iron is then titrated against a standard solution of $K_2Cr_2O_7$, using diphenylamine sulfonic acid as an indicator according to the procedure given by Willard and Furman.[59] The $SnCl_2$-HCl solution is standardized following the same procedure, but using 20 ml of 1 N $FeCl_3$ as a sample. The amount of $K_2Cr_2O_7$ required to titrate the ferrite sample can be corrected by sub-

tracting the amount required to titrate the ferrous iron formed by the 20 ml of $SnCl_2$-HCl solution. The percent by weight of ferrous iron is then

$$\%Fe^{+2} = \frac{[\text{ml } K_2Cr_2O_7(\text{sample}) - \text{ml } K_2Cr_2O_7(FeCl_3 \text{ soln})] \times .05585 \times N_{K_2Cr_2O_7} \times 100}{\text{weight of sample}}$$

The method used for storing the HCl-$SnCl_2$ solution is given by Scott.[60]

APPENDIX II

CALCULATIONS OF THE FINAL COMPOSITIONS FROM THE INITIAL COMPOSITIONS

CALCULATION OF THE RATIO $MeFe_2O_4$:Fe_3O_4

The equation for magnetite formation in a mixture of MeO and Fe_2O_3 is

$$aMeO + (a+e)Fe_2O_3 \rightarrow aMeFe_2O_4 + (e - 3/2\ b)Fe_2O_3 + bFe_3O_4 + \frac{b}{4} O_2 . \quad (A\text{-}1)$$

The mole ratio b/a, given in Table IV, can be calculated from the weight percent of ferrous iron,

$$\%Fe^{+2} = \frac{b[Fe] \times 100}{a[MeFe_2O_4] + (e - 3/2\ b)\ [Fe_2O_3] + b[Fe_3O_4]} , \quad (A\text{-}2)$$

where [ ] represent the molecular weight. Then:

$$\frac{b}{a} = \frac{\left([MeFe_2O_4] + e/a[Fe_2O_3]\right)\ \%Fe^{+2}}{100[Fe] + \left(3/2\ [Fe_2O_3] - [Fe_3O_4]\right)\%Fe^{+2}} . \quad (A\text{-}3)$$

CALCULATION OF THE RATIO b/(b+c+d)

The final composition can be expressed as follows:

$$aNi_{.474}Zn_{.526}Fe_2O_4 \cdot bFe_3O_4 \cdot cFe_2O_3 + dFe_2O_3 . \quad (A\text{-}4)$$

Using the value of b/a calculated above, and the fact that c+d = e - 3/2 b, we can write:

$$\frac{b}{b+c+d} = \frac{b}{e - 1/2\ b} . \quad (A\text{-}5)$$

CALCULATION OF THE MOLES OF $LiFeO_2$, FeO, AND Fe_2O_3

The compositions for the phase diagram given in Fig. 7 were calculated from the initial compositions and the weight percent FeO as follows. The equation for the reaction in terms of the above components is

$$xLi_2O + yFe_2O_3 \rightarrow 2xLiFeO_2 + aFeO + bFe_2O_3 + \frac{a}{4} O_2 \quad . \qquad \text{(A-6)}$$

The weight percent FeO is then

$$\%FeO = \frac{a[FeO] \times 100}{2x\ [LiFeO_2] + a[FeO] + b[Fe_2O_3]} \quad . \qquad \text{(A-7)}$$

Since $2y = 2x + a + 2b$, we have

$$b = y - x - \frac{a}{2} \quad . \qquad \text{(A-8)}$$

Substituting this value of b into Eq. (A-7) and solving for a, we obtain

$$a = \frac{\%FeO \left(2x\ [LiFeO_2] + (y-x)\ [Fe_2O_3]\right)}{100[FeO] + \left(1/2[Fe_2O_3] - [FeO]\right) \%FeO} \quad . \qquad \text{(A-9)}$$

REFERENCES

1. Barth, F. W., and Posnjak, E., "Spinel Structures With and Without Variate Atom Equipoints," Z. Krist., 82, 324-341 (1932).

2. Verwey, E.J.W., and Heilmann, E. L., "Cation Arrangement in Spinels," J. Chem. Phys., 15, 174-180 (1947).

3. Rammelsberg, C., "Über den sogenannten octaëdrischen Eisenglanz vom Vesuv, und über die Bildung von Magneteisen durch Sublimation," Ann. Physik, 107, 451-454 (1859).

4. Sauveur, A., The Metallography of Iron and Steel, II-4, 1st ed., University Press, Cambridge, U.S.A. (1912).

5. Sneed, M. C., and Maynard, J. L., General Inorganic Chemistry (D. Van Nostrand Co., Inc., New York, 1942), p. 1080.

6. Palache, C., Berman, H., and Frondel, C., Dana's System of Mineralogy I, 7th ed. (J. Wiley and Sons, New York, 1944), p. 696.

7. Néel, L., "Proprietes Magnétiques des Ferrites; Ferrimagnétisme et Antiferromagnétisme," Ann. Phys., 3, 137-198 (1948).

8. Snoek, J. L., New Developments in Ferromagnetic Materials, Elsevier Publishing Co., Inc., New York, 1949.

9. Galt, J. K., "Losses in Ferrites: Single Crystal Studies," Proc. I.E.E., 104B, 189-197 (1957).

10. Van Uitert, L. G., "dc Resistivity in the Nickel and Nickel-Zinc Ferrite System," J. Chem. Phys., 23, 1883-1887 (1955).

11. Brownlow, J. M., "Preferential Volatilization of Cation from Ferrites During Sintering," J. App. Phys., 29, 373-375 (1958).

12. Kato, Y., and Takei, T., "Studies on Zinc Ferrite: Its Formation, Composition and Chemical and Magnetic Properties," Trans. Am. Electrochem. Soc., 57, 297-312 (1930).

13. Kushima, I., and Amanuma, T., "On the Constitution of Zinc Ferrite," Mem. Fac. Eng., Kyoto Univ., 16, 191-203 (1954).

14. Roberts, H. S., and Merwin, H. E., "The System MgO-FeO-Fe_2O_3 in Air at One Atmosphere," Am. J. Sci., 21, 145-157 (1931).

15. Berger, S. V., "Röntgenunderökningar Av Spinellfasen I Systemet ZnO-Fe_2O_3," Festskr. Tillagnad J. Arvid Hedvall, 31-42 (1948).

16. Smolenski, A., "Non-Metallic Ferromagnetics-Ferrites," Izvest. Akad. Nauk S.S.S.R. Ser. Fiz., 16, 728-738 (1952).

17. Toropov, N. A., Rabkin, L. I., Freigenfeld, E. Zh., and Epstein, B. Sh., "The Influence of Several Technological Factors on Phase Composition and Magnetic Properties of Nickel-Zinc Ferrites," Zhur. Tekh. Fiz., 23, Issue 9 (1941).

18. Darken, L. S., and Gurry, R. W., "The System Iron-Oxygen II. Equilibrium and Thermodynamics of Liquid Oxide and Other Phases," J. Amer. Chem. Soc., 68, 798-816 (1946).

19. Hoffman, A., "Crystal Chemistry of Lithium Ferrites," Naturwiss., 26, 431 (1938).

20. Braun, P. B., "A Superstructure in Spinels," Nature, 170, 11-23 (1952).

21. David, I., and Welch, A.J.E., "The Oxidation of Magnetite and Related Spinels," Trans. Faraday Soc., 52, 1642-1650 (1956).

22. Collongues, R., and Chaudron, G., "Sur la preparation des Ferrites de Lithium," Compt. Rend., 231, 143-145 (1950).

23. Tammann, G., "Über die Bildungsgeschwindigkeit einiger Nitride," Z. Anorg. Chem., 124, 25-35 (1922).

24. Cohn, G., "Reactions in the Solid State," Chem. Rev., 42, 527-579 (1948).

25. Jander, W., "Reaktionen im festen Zustande bei höheren Temperaturen," Z. Anorg. Chem., 166, 31 (1927).

26. Wagner, C., "Über den Mechanismus der Bildung von Ionenverbindungen höherer Ordnung (Doppelsalze, Spinelle, Silikate)," Z. Physik. Chem., B 34, 309 (1936).

27. Huttig, G. F., Handbuch der Katalyse, ed. by G. M. Schwab, VI, 438-445, Wien (1943).

28. Finch, G. I., and Sinha, K. P., "On Reaction in the Solid State," Proc. Royal Soc. (London), 239A, 145-153 (1957).

29. Finch, G. I., and Sinha, K. P., "An Electron-Diffraction Study of the Transformation γFe_2O_3 to αFe_2O_3," Proc. Royal Soc. (London), 241A, 1-8 (1957).

30. Kedesdy, H., and Katz, G., "X-ray Diffraction Study of the Formation of Some Ni-Zn Ferrites," Ceram. Age, 62, 29-34 (1953).

31. Guillissen, J., and Van Rysselberghe, P. J., "Studies on Zinc and Barium Ferrites," Trans. Electrochem. Soc., 59, 95-106 (1931).

32. Hopkins, D. W., "The Reaction Between Solids; The Formation of Zinc Ferrite from Zinc Oxide and Ferric Oxide," Trans. Electrochem. Soc., 96, 195-202 (1949).

33. Okamura, T., and Simoizaka, J., "The Reaction Kinetics of Spinel-Type Ferrite I Nickel Ferrite," Science Repts., Research Insts., Tohoku Univ., Ser. A., 2, 675-689 (1950).

34. Yost, W., Diffusion, Academic Press, Inc., New York, 1952.

35. Linder, R., "Studies on Solid State Reactions with Radio Tracers," J. Chem. Phys., 23, 411 (1955).

36. Nagaura, S., Kato, E., and Niboshi, Y., "Solid Reaction of Zinc Chromium Spinel," J. Chem. Soc. Japan, 77, 1492-1496 (1956).

37. Kushima, I., and Amanuma, T., "Studies on the Ferrites," J. Mining Inst. Japan, 68, 267-271 (1952).

38. Hedvall, J. A., "Sintering and Reactivity in Solids," Ceram. Age, 65, 13-17 (1955).

39. Forestier, H., "Influence des Gas adsorbes sur la reactivity des surfaces solides," Proc. of the Inter. Symposium on the Reactivity of Solids, Gothenburg, 1952, Part I, 41-61, Goteborg (1954).

40. Postelthwaite, A. W., and Shaler, A. J., "Shrinkage of Synthetic Pores in Copper," The Physics of Powder Metallurgy, (McGraw-Hill Book Co., Inc., New York, 1951), pp. 189-201.

41. Roberts, J. P., "The Mechanism of Sintering," Metallurgia, 42, 123-130 (1950).

42. Robbins, J., "Magnetic Peroxide of Iron," Chem. News, 1, 11 (1859).

43. Hagg, G., "Die Kristallstruktur des magnetischen Ferrioxyds γFe_2O_3," Z. Physik. Chem., B 29, 95-103 (1935).

44. Verwey, E.J.W., "The Crystal Structure of γFe_2O_3 and γAl_2O_3," Z. Krist., 91, 65 (1935).

45. Henry, W. E., and Boehm, M. J., "Intradomain Magnetic Saturation and Magnetic Structure of γFe_2O_3," Phys. Rev., 101, 1253-1254 (1956).

46. Wagenkneckt, V. F., "Über die elektrischen und magnetischen Eigenschaften von ferromagnetischem γ Eisen-(III)-oxyd im hochfrequenten Wechselfeld," Kolloid, 112, 35-60 (1949).

47. Sachse, H., and Haase, R., "Die magnetischen Umwandlungen des regularen Ferrioxyds," Z. Physik. Chem., 148, 401-412 (1930).

48. Michel, A., and Lensen, M. "Sur la stabilisation du sesquioxyde de fer cubique," Compt. Rend., 243, 1422-1423 (1956).

49. De Boer, F. E., and Selwood, P. W., "The Activation Energy for the Solid State Reaction $\gamma Fe_2O_3 \rightarrow \alpha Fe_2O_3$," J. Am. Chem. Soc., 76, 3365-3367 (1954).

50. Nicholls, G. D., "The Mineralogy of Rock Magnetism," Advances Phys., 4, 113-190 (1955).

51. Kojima, H., "On the Magnetic Properties of Iron Oxides," Science Repts., Research Insts., Tohoku Univ., Ser. A, 6, 178-183 (1954).

52. Welo, L. A., and Baudisch, O., "The Two Stage Transformation of Magnetite," Phil. Mag., 50, 399 (1925).

53. de Boer, J. H., and Houben, G.M.M., "The Binding of Water in and on Aluminum Oxide," Proc. of the Inter. Symposium on the Reactivity of Solids, Gothenburg, 1952, Part I, 237-244, Goteborg (1954).

54. Kulp, S. L., and Trite, A. F., "Differential Thermal Analysis of Natural Ferric Oxide," Am. Mineralogist, 36, 23-44 (1951).

55. Schmidt, E. R., and Vermaas, F.H.S., "Differential Thermal Analysis and Cell Dimensions of Some Natural Magnetites," Am. Mineralogist, 40, 422-431 (1955).

56. Lepp, H., "Stages in the Oxidation of Magnetite," Am. Mineralogist, 42, 679-681 (1957).

57. Faust, G. T., "Thermal Analysis of Quartz and Its Use in Calibration of Thermal Studies," Am. Mineralogist, 33, 337-345 (1948).

58. Kolthoff, I. M., and Lingane, J. J., Polarography, Vol. I (Interscience Publishing, Inc., New York, 1952), p. 396.

59. Willard, H. H., and Furman, N. H., Elementary Quantitative Analysis, 3rd ed., D. Van Nostrand Co., Inc., New York, 1940.

60. Scott, W. W., Standard Methods of Chemical Analysis, 3rd ed., Vol. I (D. Van Nostrand Co., Inc., New York, 1922), p. 256a.

DISTRIBUTION LIST
Contract No. AF 18(603)-8

Agency	No. of Copies
Commander Air Force Office of Scientific Research Air Research and Development Command Washington 25, D. C. Attn: SRQB	5
Commander Wright Air Development Center Wright-Patterson Air Force Base, Ohio Attn: WCRRH Attn: WCRRL Attn: WCRTL Attn: WCRTM-1	4
Commander Air Force Cambridge Research Center L. G. Hanscom Field Bedford, Massachusetts Attn: Technical Library Attn: CRRF	2
Commander Rome Air Development Center Griffiss Air Force Base Rome, New York Attn: Technical Library	1
Director Office for Advanced Studies, AFOSR P. O. Box 2035 Pasadena 2, California	1
Superintendent Diplomatic Pouch Rooms Department of State Washington 25, D. C. For transmittal to: Commander European Office, ARDC c/o American Embassy Brussels, Belgium	1
Armed Services Technical Information Agency Arlington Hall Station Arlington 12, Virginia	10
Director of Research and Development Headquarters, USAF Washington 25, D. C. Attn: AFDRD-RE-3	1
Department of the Navy Office of Naval Research Washington 25, D. C. Attn: Code 423 Attn: Code 421	2
Officer in Charge Office of Naval Research Navy No. 100 Fleet Post Office New York, New York	1
Commanding Officer Naval Radiological Defense Lab. San Francisco Naval Shipyard San Francisco 24, California	1
Director Research and Development Division General Staff Department of the Army Washington 25, D. C.	1
Division of Research U. S. Atomic Energy Commission Division Office Washington 25, D. C.	1
U. S. Atomic Energy Commission Library Branch Technical Information Div., ORE P. O. Box No. E Oak Ridge, Tennessee	1

DISTRIBUTION LIST (Continued)

Agency	No. of Copies
Oak Ridge National Laboratory P. O. Box P Oak Ridge, Tennessee Attn: Central Files	1
Brookhaven National Laboratory Upton, Long Island, New York Attn: Research Library	1
Argonne National Laboratory P. O. Box 299 Lemont, Illinois Attn: Librarian	1
Ames Laboratory Iowa State College P. O. Box 14A, Station A Ames, Iowa	1
Knolls Atomic Power Laboratory P. O. Box 1072 Schenectady, New York Attn: Document Librarian	1
National Bureau of Standards Library Room 203, Northwest Building Washington 25, D. C.	1
Director, Office of Ordnance Research Box CM, Duke Station Durham, North Carolina	1
Office of Technical Services Department of Commerce Washington 25, D. C.	1
Commander Western Development Div. (ARDC) P. O. Box 262 Inglewood, California Attn: WDSIT	1
Document Custodian Los Alamos Scientific Lab. P. O. Box 1663 Los Alamos, New Mexico	1
Arnold Engineering Development Center P. O. Box 162 Tullahoma, Tennessee Attn: Technical Library	1
Commanding Officer Ordnance Materials Research Office Watertown Arsenal Watertown 72, Massachusetts	1
Commanding Officer Watertown Arsenal Watertown 72, Massachusetts Attn: Watertown Arsenal Labs Technical Reports Section	1
National Advisory Committee for Aeronautics 1512 H Street, N. W. Washington 25, D. C.	1
Commander Air Technical Intelligence Center Wright-Patterson Air Force Base, Ohio Attn: Deputy for Documentation	1
Commander Hq, AF Office of Scientific Research Washington 25, D. C. Attn: SREC, Technical Library	2

DISTRIBUTION LIST (Concluded)

Agency	No. of Copies
Commandant AF Institute of Technology Wright-Patterson Air Force Base, Ohio Attn: Technical Library, MCLI	1
Commander Wright Air Development Center Wright-Patterson Air Force Base, Ohio Attn: WCLTY-3 Mr. Robert Besamson	1
Prof. A. H. Morrish Dept. of Electrical Engineering University of Minnesota Minneapolis, Minnesota	1
Dr. W. F. Brown, Jr. Central Research Department Minnesota Mining and Mfg. Co. 2301 Hudson Road St. Paul 6, Minnesota	1
Dr. R. J. Prosen Honeywell Research Center Hopkins, Minnesota	1
L. E. Blazier, Research Library A C Spark Plug Division, GMC Flint 2, Michigan	2
Dr. L. Reiffel, Manager Physics Research Armour Research Foundation 3440 South State Street Chicago 16, Illinois	1
Dr. Nat Schwartz, Bldg. 3 Electronics Park General Electric Company Syracuse, New York	1
Dr. G. T. Rado Naval Research Laboratory Washington 25, D. C.	1
Mr. John L. Dalke, Div. 84.30 National Bureau of Standards Boulder, Colorado	1
Dr. D. M. Grimes Dept. of Electrical Engineering The University of Michigan Ann Arbor, Michigan	8
Dr. H. Katz, Bldg. 3 Electronics Park General Electric Company Syracuse, New York	1
The University of Michigan Research Institute Project File The University of Michigan Ann Arbor, Michigan	1
Mr. Peter H. Haas Mine Fuze Division Diamond Ordnance Fuze Labs Washington 25, D. C.	1
Dr. R. M. Bozorth Bell Telephone Laboratories Murray Hill, New Jersey	1
Mr. John A. Osborn, Manager Magnetic Materials Development Section Westinghouse Electric Corp. 501 Highland Avenue East Pittsburgh, Pennsylvania	1
Mr. Robert Harrington, Div. 84.30 National Bureau of Standards Boulder, Colorado	1
Dr. John B. Goodenough Lincoln Laboratory, MIT Cambridge, Massachusetts	1
Mr. Frank R. Arams Airborne Instruments Laboratory Mineola, Long Island, New York	1